Equalization and Blind Signal Combining Algorithms for Mobile Television Broadcast Reception

Von der Fakultät Informatik, Elektrotechnik und
Informationstechnik der Universität Stuttgart zur
Erlangung der Würde eines Doktor-Ingenieurs (Dr.-Ing.)
genehmigte Abhandlung

Vorgelegt von

Rana Hesham Abdelmonem Ahmed

aus Kairo

Hauptberichter:	Prof. Dr.-Ing. J. Speidel
Mitberichter:	Prof. Dr.-Ing. B. Yang
Tag der mündlichen Prüfung:	19. Januar 2016

Institut für Nachrichtenübertragung der Universität Stuttgart

2016

Acknowledgements

This dissertation is the outcome of my activities as a research assistant at the Institute of Telecommunications, University of Stuttgart, Germany. I would like to express my sincere gratitude to my adviser Professor Joachim Speidel for giving me the opportunity to work under his supervision. It has been a great pleasure for me to work with him. His encouragement and confidence in me helped me greatly throughout my work. His valuable advice and feedback have helped me refine my way of thinking towards a clear and scientific perspective and have enabled the publication of my research results.

I would also like to thank Professor Bin Yang for taking over the assessment of this thesis. His valuable comments helped me a lot refining this dissertation. Warm thanks to all of my colleagues at the INUE for creating a very positive and nice working environment at the institute. Very special thanks to all of my former students who supported this work through their master theses work and whom I learned a lot from. Working with all of you was indeed my pleasure.

Furthermore, I would like to express my gratitude to my colleagues from Sony Stuttgart, where I spent most of my PhD. I would like to especially thank Ben Eitel for his tremendous support during this work. His guidance and experience were extremely valuable to my work. In addition, I also would like to sincerely thank him for reading this thesis and giving me very useful feedback. Special thanks to Nabil Loghin and Daniel Schneider, I truly enjoyed working with you two, you always gave me your fullest support and still allowed me to contribute with my own ideas. I also enjoyed all the technical discussions with all of my colleagues at Sony in a positive and productive environment. I would like to thank Stefan Uhlich, Thomas Handte, Martin Fritz and David Roerich for reading parts of this thesis and giving me invaluable comments.

To my friends in Germany, especially Rana, Iman, Norhan, Nadiah and Noran thanks for being you. I saved the final and most special thanks to my family, my parents: Asmaa and Hesham, siblings: Reem and Khaled, my grandparents: Ragab and Kawthar and to my lovely fiancé Mohamed for their unconditonal support. I dedicate this thesis to my loving family for believing in me even when I did not.

"The man of knowledge is the one who recognizes that what is known is very little compared to what is not known". Ali ibn Abi Talib.

Contents

Acronyms

ADSL	asymmetric digital subscriber line
ASW	adaptive sliding window
ATSC	Advanced Television Systems Committee
ATSC 2.0	Advanced Television Systems Committee 2.0
ATSC 3.0	Advanced Television Systems Committee 3.0
AWGN	additive white Gaussian noise
aZF	approximated zero forcing
BER	bit error ratio
BCI	blind channel identification
BCH	Bose, Chaudhuri, and Hocquenghem
BMRC	blind maximum ratio combining
CFR	channel frequency response
CIR	channel impulse response
CLT	central limit theorem
CMA	constant modulus algorithm
CMMB	Chinese Mobile Multi-Media Broadcast System
CoP	continual pilot
CP	cyclic prefix
CR	cross relations
CSI	channel state information
DOA	direction of arrival
DTMB	Digital Terrestrial Multimedia Broadcast
T-DMB	Terrestrial Digital Media Broadcasting
DVB	Digital Video Broadcast
DVB-C	Digital Video Broadcast-Cable Standard
DVB-C2	Second Generation Digital Video Broadcast-Cable Standard
DVB-NGH	Digital Video Broadcast Next Generation Handheld
DVB-H	Digital Video Broadcast Handheld Standard
DVB-T	Digital Video Broadcast-Terrestrial Standard
DVB-T2	Second Generation Digital Video Broadcast-Terrestrial Standard
DVB-S	Digital Video Broadcast-Satellite Standard
DVB-S2	Second Generation Digital Video Broadcast-Satellite Standard
DVB-S2X	Extended Second Generation Digital Video Broadcast-Satellite
EGC	equal gain combining
eMBMS	Enhanced Multimedia Broadcast Multicast Service
EVD	eigenvalue decomposition
FEC	forward error correction

FEF	future extension frame
FFT	fast Fourier transform
FIR	finite impulse response
FWS	fixed window size
GACN	genie-aided channel knowledge
GI	guard interval
HOS	higher order statistics
IBI	inter-block interference
ICI	inter-carrier interference
ICIC	inter-carrier interference canceler
IFFT	inverse fast Fourier transform
ISDB-T	Integrated Services Digital Broadcasting-Terrestrial
ISI	intersymbol interference
LDPC	low density parity check
LOS	line of sight
LLR	log-likelihood ratio
LMS	least mean square
LOS	line of sight
LS	least squares
LTE	long term evolution
MBMS	multimedia broadcast multicast service
MCFLMS	multi-channel frequency least mean squares
MCLMS	multi-channel least mean squares
MIL	matrix inversion lemma
MIMO	multiple input multiple output
MISO	multiple input single output
ML	maximum likelihood
MMSE	minimum mean squared error
MSE	mean squared error
MRC	maximum ratio combining
MSE	mean squared error
MUSIC	multiple signal classification
NLOS	non line of sight
NRPMSE	normalized root projection mean squared error
OC	optimum combining
OFDM	orthogonal frequency division multiplexing
PACE	pilot assisted channel estimate
PANE	pilot assisted noise estimate
PDF	probability density function
PIC	parallel interference canceler
PN	pseudo-noise
PRBS	pseudo-random binary sequence
p-t-m	point to multi-point
QAM	quadrature amplitude modulation

RF	radio frequency
SD	selection diversity
SDCC	simplified Doppler compensation combining
SFN	single frequency network
SFN-TU6	single frequency network typical urban 6 tap channel
SIC	successive interference cancellation
SIMO	single input multiple output
SINR	signal to interference plus noise ratio
SIR	signal to interference ratio
SISO	single input single output
SNR	signal-to-noise ratio
SOS	second order statistics
SP	scattered pilot
SSC	switch and stay combining
SVD	singular value decomposition
TFS	time frequency slicing
TPS	transmitter parameter signalling
TU6	typical urban 6-tap channel
VSB	vestigial sideband
ZF	zero-forcing
2D	two dimensional
2TU6	double typical urban 6 tap channel
3TU6	triple typical urban 6 tap channel
3GPP	third generation partnership project
5G	5th generation mobile network

Notation and Used Symbols

Notation

x	Scalar variable
$\mathbf{x}$	Vector or matrix in time domain
$\mathbf{X}$	Vector or matrix in frequency domain
$\mathbf{x}_{(A\times B)}$	Vector or matrix $\mathbf{x}$ of size A rows and B columns
$\hat{x}$	Estimate of scalar variable x
$\hat{\mathbf{x}}$	Estimate of vector or matrix $\mathbf{x}$
$\check{\mathbf{x}}$	Vertically concatenated vectors or matrices $\mathbf{x}$ from multiple antennas
$\tilde{x}$	Unnormalized estimate of scalar variable x
$\tilde{\mathbf{x}}$	Unnormalized estimate of vector or matrix $\mathbf{x}$
x_m	Scalar variable x corresponding to receive antenna m
$\mathbf{x}_m$	Vector or matrix $\mathbf{x}$ corresponding to receive antenna m
$\bar{\mathbf{X}}(k)$	Subset of vector or matrix $\mathbf{X}$ centered at subcarrier position k
$x(i,l)$	Scalar variable x related to i^{th} scatterer and l^{th}channel tap index
$\|\mathbf{x}\|_p$	l_p-norm of vector or matrix $\mathbf{x}$
$\|x\|$	Absolute value of x
x^*	Complex conjugate of scalar x
$\dot{x}(t)$	First derivative of function $x(t)$
$\ddot{x}(t)$	Second derivative of function $x(t)$
$E\{.\}$	Expectation operator
$\min_x f(x)$	Minimum of $f(x)$ with respect to x
$\mathbf{x}^T$	Transpose of vector or matrix $\mathbf{x}$

$\mathbf{x}^H$	Hermitian of vector or matrix $\mathbf{x}$
$\mathbf{x}^{-1}$	Inverse of matrix $\mathbf{x}$
$\mathbf{x}^\dagger$	Pseudo inverse of vector or matrix $\mathbf{x}$
$\nabla\mathbf{x}$	Gradient operator applied on vector or matrix $\mathbf{x}$

Used Symbols

a	Channel coefficient
a_{drop}	Maximum amplitude QAM symbol threshold used in PIC to detect unreliable QAM symbols
a_{sat}	Saturation amplitude QAM symbol threshold used in PIC for noise reduction on initial QAM symbol estimates
a_{max}	Maximum value of real or imaginary components of modulated symbols
A_R	Peak amplitude of the dominant LOS tap in a Rice channel
$A\left(k,k^{'}\right)$	Weighting given to noise contribution from carrier (pilot) located at subcarrier index $k^{'}$, for computing the noise information at carrier k
$\mathbf{A}$	Noise coloring weighting vector
B	Observation window containing samples of received signal from one antenna
B_c	Coherence bandwidth
B_s	Signal bandwidth
B_{sc}	Subcarrier bandwidth
c	Speed of light
c_{SDCC}	Constant factor used in SDCC
$\mathbf{C}_{\text{Noise}}$	AWGN autocovariance matrix across frequency
$\check{\mathbf{C}}_{\text{Noise}}$	AWGN autocovariance matrix across antennas
$\check{\mathbf{C}}_{\text{ICI}}$	ICI vector autocovariance matrix across antennas
$\check{\mathbf{C}}$	Noise +ICI autocovariance matrix across antennas
$\mathbf{C}_{r_m}$	Circulant matrix of sequence $\mathbf{r}_m$

d	Off-diagonal distance
d_{ant}	Distance between two antennas
D	Number of off-diagonal coefficients
D_I	Interleaving depth
D_x	Pilot spacing in frequency direction
D_y	Pilot spacing in time direction
D_t	Resultant Pilot spacing in time direction
D_f	Resultant Pilot spacing in frequency direction
D_{max}	Maximum number of considered off-diagonal coefficients
D_{simo}	Number of off-diagonal coefficients in a SIMO combiner
$\mathbf{D}_m^u$	Diagonal matrix containing frequency domain received signal on antenna m for the u^{th} block
e	Error signal used in MCLMS
$\mathbf{e}$	Error vector
$\mathbf{E}$	Frequency domain error vector
f_c	Carrier frequency
$f_{D,max}$	Maximum Doppler shift
f_{D_i}	Doppler shift from i^{th} scatterer
$f_{D,norm}$	Normalized Doppler shift
$\mathbf{F}_B$	Normalized DFT matrix of size $B \times B$
$F\,(r,\, c)$	Element at r^{th} row and c^{th} column in normalized DFT matrix $\mathbf{F}$
$\mathbf{g}_m$	Toeplitz channel matrix representing multi-path time domain channel of antenna m
$h\,(n,\, l)$	Time varying channel transfer function at time index n and tap index l
$h_m(n,\, l)$	Time varying channel transfer function at time index n, tap index l and receive antenna m
$h\,(l)$	Channel transfer function at tap index l

$h^{avg}(l)$	Average channel transfer function at tap index l
$H_m(k,\, k)$	Main diagonal coefficient of channel frequency matrix at subcarrier index k from antenna m
$H_m(k,\, k^{'})$	Off-diagonal interference coefficient of subcarrier index $k^{'}$ on subcarrier index k from antenna m
$\hat{H}_p$	Pilot assisted channel estimate
$H_k(n)$	Channel frequency response of subcarrier k at time index n.
$\mathbf{H}_{f,m}(k)$	Channel interference vector at subcarrier index k from antenna m
$\mathbf{h}_m$	Channel vector of antenna m
$\mathbf{H}^F$	2D FFT channel matrix
i	Scatterer index notation
i_o	Polynomial order used in channel interpolation
I	Interference signal
$I_D(k)$	Interference function at subcarrier position k from interferers that are D subcarriers apart
$\mathbf{I}_B$	Identity matrix of size $B \times B$
j	Imaginary unit
j_{CR}	Cost function of cross relations error in time domain
J_{CR}	Cost function of cross relations error in frequency domain
j_{SCR}	Cost function of sparse cross relations error in time domain
J_μ	Cost function of variable step size
$J_0(x)$	Bessel function
k	Subcarrier index
k_p	Pilot subcarrier index
k_ϕ	Phase threshold used in tap coefficient masking
k_{onr}	Out-of-band energy clipping threshold
k_2	Gain of the second TU6 channel
l	Channel tap index

L	Channel length
m	Receive antenna index
M	Number of receive antennas
n	Discrete time index
n_{LDPC}	LDPC codeword length
N	FFT size
N_{pilots}	Number of pilot subcarriers in an OFDM symbol
N_{GI}	Number of subcarriers in a guard interval
N_a	Number of active subcarriers in an OFDM symbol
N_{data}	Number of data subcarriers in an OFDM symbol
N_s	Number of scatterers
N_{SP}	Number of scattered pilot subcarriers
N_{CoP}	Number of continual pilot subcarriers
p	Pilot index in frequency domain
P	Channel cross-correlation matrix entry, used in Wiener interpolation
$\mathbf{P}$	Channel cross-correlation matrix used in Wiener interpolation
q	Number of continual pilots in a noise window
r	Received OFDM symbol in time domain
R	Received OFDM symbol in frequency domain
$R_{\hat{H}_p}$	Channel frequency response auto-correlation matrix entry, used in Wiener interpolation
$\mathbf{R}_{\hat{H}_p}$	Channel frequency response auto-correlation matrix, used in Wiener interpolation
$\mathbf{R}_{ss}$	Auto-correlation matrix of the sent signal
s	Transmitted OFDM symbol in time domain
S	Transmitted OFDM symbol in frequency domain
t	Continuous time index
T	Elementary period in an OFDM system (sampling time)

T_s	Useful time of an OFDM symbol
T_c	Channel coherence time
u	Block index
$\mathbf{U}$	Wiener filter coefficients
v	Temporal difference in channel frequency response coefficients' between two successive OFDM symbols
x	AWGN noise
X_t	Total noise+ICI in the frequency domain
W	Weight coefficient
$\tilde{\mathbf{W}}_{aZF}$	Approximated ZF weighting vector
$\tilde{\mathbf{W}}_{mrc}$	MRC weighting vector
$\tilde{\mathbf{W}}_{OC}$	OC weighting vector
$\tilde{\mathbf{W}}_{SDCC}$	SDCC weighting vector
$\mathbf{w}_{PRBS}$	PRBS used in pilot generation
y	OFDM symbol index
z	Discrete frequency index of Z transform
$\mathbf{Z}$	Noise+ICI correlation matrix used in OC
α	Ambiguity factor of blind channel estimate
γ	Inter-channel noise+ICI ratio
$\delta(x)$	Dirac delta function
Γ	Signal to noise ratio
Γ_t	Total signal to noise ratio
ϵ	Normalization factor after diversity combining
ζ	Sparseness measure
θ	Scattered angle
ι	Index of CoP
κ	Constant used in SDCC approximation

λ	Forgetting factor parameter
λ_{mask}	Forgetting factor parameter used in masking operation
λ_s	Sparseness weighting factor
μ	Step size
Ξ	ICI leakage coefficient
σ^2	Noise variance
σ_t^2	Total noise variance
σ_{ICI}^2	ICI noise variance
$\sigma_{resICI}^2(2D)$	Residual ICI noise variance outside a considered number of $2D$ sub- and super-diagonals
E_R	Received symbol power
E_S	Transmitted symbol power
τ	Channel time delay
τ_2	Time delay of the second channel in a 2TU6 channel
τ_{max}	Maximum channel time delay
ϕ	Tap phase information
$\bar{\phi}$	Average difference in phase information
χ	Noise de-normalization factor
$\Upsilon_D(k)$	Signal power to D^{th} interferer power at subcarrier position k
Ω_{SP}	Set of scattered pilots
Ω_{CoP}	Set of continual pilots

Abstract

Mobile TV reception through orthogonal frequency division multiplexing (OFDM) based terrestrial networks such as digital video broadcast-terrestrial standard (DVB-T) and its second generation DVB-T2 imposes many challenges on the receiver equalizer block. In this thesis, we deal with the problem of inter-carrier interference (ICI) in an OFDM receiver, due to a time-varying multi-path channel. We show that taking the ICI frequency selectivity into account, a better trade-off between performance and complexity can be reached in single input single output (SISO) and single input multiple output (SIMO) receivers. In addition, our simulation results suggest that exploiting spatial diversity, especially using ICI-aware antenna receiver diversity combining techniques, is a very effective technique to mitigate ICI. We also study several concatenations of receiver diversity combining and SISO ICI cancelers. Simulation results suggest that the best Doppler resistance can be achieved using an ICI-aware receiver diversity combining technique followed by an ICI canceler.

In the second part of this thesis, we investigate a special architecture of receiver diversity combining, which works independently of the underlying broadcasting standard. Blind identification using multi-channel frequency least mean squares (MCFLMS) is carried out to estimate the channel without using pilots. We also introduce several enhancements on MCFLMS to allow better tracking of fast time-varying multi-path communication channels. Our simulation results show that modified blind maximum ratio combining (MRC), even with no synchronization information, can reach a very close performance level to that of the classical MRC with genie-aided channel knowledge (GACN).

Kurzfassung

Digitale Fernsehübertragungssysteme wie DVB-T und DVB-T2 arbeiten mit orthogonaler Mehrträgermodulation OFDM. Dieses Modulationsverfahren stellt sehr hohe Anforderungen an den mobilen Empfänger. Die vorliegende Arbeit beschäftigt sich mit dem Einfluss und der Verringerung von Interkanalinterferenz-Störungen (ICI), welche durch die zeitvariante Mehrwegeausbreitung bei Mobilempfang verursacht wird. Es wird gezeigt, dass eine Berücksichtigung der Frequenzselektivität des Spektrums der ICI zu einem besseren Kompromiss zwischen Leistungsfähigkeit und Komplexität bei Empfängern mit einer Antenne (SISO) und bei Empfängern mit mehreren Antennen (SIMO) führt. Darüber hinaus zeigen die vorgestellten Ergebnisse, dass ICI sehr effektiv durch Ausnutzung der räumlichen Diversität durch Empfänger unterdrückt werden kann, welche die verschiedenen Empfangssignale geeignet verknüpfen (Diversity Combining). Auch die Kettenschaltung aus Diversity Combining und ICI-Entzerrung wird für verschiedene Varianten vorgestellt. Simulationen zeigen, dass die größte Robustheit gegenüber dem Doppler-Effekt durch eine Anordnung aus Diversity Combining unter Berücksichtigung von ICI gefolgt von ICI-Entzerrung erzielt werden kann.

Im zweiten Teil der Arbeit wird eine spezielle Empfänger struktur mit Diversity Com-

bining untersucht, welche unabhängig vom verwendeten Rundfunkstandard ist, was einen großen technischen Vorteil darstellt. Unter Verwendung eines Verfahrens zur blinden Systemidentifikation (Multi-Channel Frequency Least Mean Squares, MCFLMS) wird der Kanal ohne Verwendung von Pilotträgern blind geschätzt. Es werden außerdem mehrere Erweiterungen des MCFLMS-Verfahrens vorgestellt, die eine verbesserte Nachführung der Kanalschätzung von sich schnell ändernden Mehrwegekanälen ermöglichen. Simulationen zeigen, dass ein vorgeschlagenes, modifiziertes blindes Maximum-Ratio-Combining (MRC)-Verfahren ohne jegliche Synchronisation sehr nahe an die Leistungsfähigkeit von klassischen MRC-Verfahren mit perfekter Kanalkenntnis herankommt.

1. Introduction

1.1. Motivation

The mobile wireless industry has undergone a great progress in device capability over the recent years; in response to the ever growing requirements and expectations of users and mobile operators. Such a progress has enabled new exciting services to emerge such as mobile TV. Consumers now have appropriate sized screens, through their tablets and smart phones, to receive mobile TV broadcasting. Commercial trials have revealed strong consumer interest according to [Mas06]. Nowadays, users can easily buy mobile TV tuners to work in vehicles or on their hand-held devices; to follow live events like football matches, the Oscars, etc. However, most of the widespread digital terrestrial broadcasting standards, such as the Digital Video Broadcast-Terrestrial Standard (DVB-T), were not initially designed to serve mobile reception with high terminal speed. Therefore, many challenges are encountered with the mobile environment. In fact, many voices have called for providing mobile TV services through the cellular systems, which are especially designed to deal with the mobile environment.

Cellular systems have been initially designed for unicast services. On the one hand, an advantage of providing broadcast services through the cellular network is that users can access content on-demand, rather than following a fixed schedule. Another advantage is the ability to adapt the transmission parameters depending on the user settings instead of designing the system based on the worst case user. On the other hand, a major disadvantage is the poor scalability as the number of users increase in the network [GB13]. To deal with these limitations, third generation partnership project (3GPP) has defined a broadcast extension, called multimedia broadcast multicast service (MBMS) for existing and upcoming 3GPP networks. MBMS introduces new point to multipoint (p-t-m) radio channels and multi-cast support in the core network. In [HHH$^+$07], the limitations of using unicast technology to provide mobile TV reception is studied and a hybrid unicast-broadcast delivery scheme is proposed. Although it gained a lot of attention, MBMS has not been practically deployed so far. Its long term evolution (LTE) version Enhanced Multimedia Broadcast Multicast Service (eMBMS), on the other hand, seems more promising where several broadcasters such as Verizon [Flo14] have announced they are trialling or deploying eMBMS.

This thesis discusses the challenges faced at the equalization stage in mobile TV orthogonal frequency division multiplexing (OFDM) based broadcast reception with a special focus on the problem of inter-carrier interference (ICI). ICI is a special kind of interference which occurs due to the time varying channel in a mobile OFDM receiver. ICI is a major challenge especially in mobile broadcasting, with the relatively small carrier spacings. For example, on an 8 MHz channel, the carrier spacing in DVB-T can be

either 1.116 kHz in the 8k mode or 4.47 kHz in the 2k mode, i.e, at least 3 times smaller than that of LTE which is 15 kHz. Because of this very small carrier spacing, DVB-T and Second Generation Digital Video Broadcast-Terrestrial Standard (DVB-T2) systems are very sensitive to temporal channel variations.

As we shall see, one elegant solution to such a problem and a general technique to boost a wireless system performance is to employ multiple antennas at the receiver side, i.e., antenna receiver diversity. In such case, the information message is sent via a single antenna at the transmitter side and later captured via multiple appropriately spaced[1] antennas at the receiver side, i.e., a single input multiple output (SIMO) system. In this context, we shall observe that ICI-aware diversity combining, which seek maximizing the signal to interference plus noise ratio (SINR) can deliver a significant improvement in Doppler resistance. We show that even, with no special ICI consideration, a significant improvement in the Doppler resistance is observed when using 2 antennas instead of one.

Sending the same copy of information over M independent different channels, and with no special ICI consideration, the received signals can be combined using four principal types of algorithms, which differ in the amount of channel state information (CSI) required, used complexity and performance [SA05]:

1. maximum ratio combining (MRC): which assigns different weights to the received signals coming from the different antennas, depending on the channel strength experienced over each antenna.

2. equal gain combining (EGC): which assigns the same weights to all the received signals coming from the different antennas.

3. selection diversity (SD): only processes the received signal obtained from the strongest channel.

4. switch and stay combining (SSC): a variant of SD, which selects the strongest branch at a certain point of time and does not scan further for the strongest branch until the received power drops below a certain threshold.

The most promising performance of which is that of MRC. For equally likely transmitted symbols and in the absence of correlation among the antennas, MRC produces a total signal-to-noise ratio (SNR) per symbol, Γ_t, at the output of MRC given by [Stu96] $\Gamma_t = \sum_{m=1}^{M} \Gamma_m$, where Γ_m denotes the SNR of the diversity branch on the m^{th}antenna and M is the number of receive antennas. However, in order to achieve this gain, MRC requires full knowledge of the channel coefficients' amplitude and phase information. Other algorithms require less information, such as information about the strongest branch, phase angle of the channel coefficients, etc., but at the expense of an inferior performance. To acquire this information, standard dependent blocks have to be placed before the

[1]The spacing is to guarantee the received signals have gone through independent fading channels. Typically, a spacing distance $d_{ant} > \frac{\lambda_w}{2}$ is required, where λ_w is the wavelength used for transmission [PNG08].

combining stage which performs this task. This means that, for example, a receiver with a single antenna can't be easily modified to a SIMO receiver. In such case the whole architecture has to be rebuilt.

In the second part of this thesis, we discuss a standard independent receiver diversity combining scheme proposed in [AES13, EAS13]. The proposed architecture acts as a universal combining stage that can be placed between the receiver front end and the demodulator block. Our goal is to decouple the combining stage from the system based demodulator. The proposed architecture is very advantageous for system on chip design, for example in receivers which are designed to receive transmit signals from different standards. Moreover, an existing single input single output (SISO) receiver can be easily extended to a SIMO receiver, by adding the standard independent combining unit between the multiple antennas and the SISO demodulator. With these advantages, extra processing power and time delay latency are expected. Broadcasting systems, however, are known for having less restrictions on latency compared to cellular communication systems and thus we are left with the processing power as our concern. The combining stage should combine the received distorted signals using MRC, producing a signal with a higher SNR. The standard based demodulator removes the distortion from the combined signal.

1.2. Organization of the Thesis

This thesis is organized as follows. In Chapter 2, we start by presenting the mathematical model of the time-varying channel model considered in this work. We then introduce the motivation and introduction to the class of multi-carrier signals, which serves as a basis for discussion in later Chapters. We then give a brief overview of the most common digital broadcasting systems around the world, to focus finally on the Digital Video Broadcast (DVB) family of standards. We give a brief overview of this standard and describe how channel and noise estimation are conducted in our system implementation.

In Chapter 3, the problem of ICI due to mobile reception of an OFDM signal is investigated in detail. We lay down a mathematical model which describes how ICI can be modeled and computed in practice. We also focus on the problem of ICI in a time-varying frequency selective channel, i.e., a double selective channel. From the observations obtained in this section, we are able to introduce two receiver enhancements in [ALS14, AES15]. We then move to introduce two well known classes of SISO ICI cancelers, namely minimum mean squared error (MMSE) ICI canceler and parallel interference canceler (PIC). Within this context, we present a proposed enhancement to an MMSE- inter-carrier interference canceler (ICIC) namely MMSE-adaptive sliding window (ASW) ICIC.

Chapter 4 deals with the problem of ICI mitigation in a multi-antenna receiver. We present several algorithms proposed in the literature for multi-antenna receiver signal combining including the classical MRC scheme which does not consider ICI in its operation. Other discussed approaches consider ICI in the combining stage, leading to a better ICI mitigation performance, compared to MRC, at the expense of higher complexity and

memory requirements. Within this context, we present a modified approach for MRC, where ICI is not directly considered but which assumes ICI to be a source of colored noise. We then investigate the possible gains from concatenating several combining algorithms with ICI cancelers. We compare between two possible architectures, depending on the order of SIMO combining and ICI cancellation, namely SIMO combining first or ICI cancellation first. In our comparisons, we rely on coded bit error ratio (BER) results obtained from testing the abovementioned algorithms on a DVB-T system.

In Chapter 5, we discuss a proposed blind maximum ratio combining (BMRC) architecture. The proposed unit uses blind channel identification (BCI), in particular multi-channel frequency least mean squares (MCFLMS), to compute the channel coefficients used for building the weighting vectors for MRC. We describe in detail the challenges obtained when applying the proposed algorithm on practical communication systems and the solutions proposed. At the end, we present coded BER results for the proposed architecture with the proposed enhancements tested on a DVB-T2 system.

We end this thesis, by the conclusions in Chapter 6 with a summary of our main results. We draw from these results the possible directions we believe could be investigated in future work.

2. Overview of Transmitter and Wireless Channel Model

In this Chapter, we give an overview of the transmitter and channel model used in this work. We deal with the equivalent baseband channel after radio frequency (RF) demodulation. We start by laying the mathematical model of the multi-path time-varying channel impulse response. From this point, we derive a motivation for the well known class of multi-carrier signals. Finally, we present a brief overview of the main digital terrestrial/hand-held broadcasting systems around the world, with special focus on the DVB-T and DVB-T2 systems deployed widely in Europe, Australia, most of Asia and Africa[Rei05].

2.1. Fundamentals

2.1.1. Multi-Path Time Varying Channel Model

The channel fading can be described by two different spatial scales [Rap96, Skl]:

1. large Scale Fading: due to motion over large areas. Large scale models describe the path loss due to the distance between the transmitter and the receiver and the surrounding environment hills, buildings, etc.

2. small Scale Fading: due to motion over a limited scale of few wavelengths. The received signal is typically the sum of many reflections coming from different directions. The phases are random and therefore the components change significantly even with a small motion over a fraction of a wavelength.

In this work, we describe the fading of a channel, assuming that the receiver antenna remains within a limited trajectory, i.e., large scale fading can be assumed as a constant [Skl]. In general, two main phenomena govern the statistics of small scale fading :

1. time delay spreading of the received signal (“ echoes”) caused by multi-path propagation delays.

2. time varying behavior of the channel impulse response, due to relative motion of transmitter, receiver and/or surrounding scatterers. For the rest of this work, we assume only the receiver antenna is in motion.

In an environment with no direct line of sight (LOS) between the transmitter and the receiver, i.e., a non line of sight (NLOS) environment, the envelope of the received signal can be described by a Rayleigh probability density function (PDF)

$$p_r(r) = \frac{r}{E_R} \exp\left(\frac{-r^2}{2E_R}\right); r \geq 0, \tag{2.1}$$

where E_R is the average received signal power. Such a channel is called Rayleigh fading channel. With direct LOS between the transmitter and the receiver, the envelope of the received signal is described by the Rician PDF

$$p_r(r) = \frac{x}{E_R} \exp\left(\frac{-\left(r^2 + A_R^2\right)}{2E_R}\right) J_0\left(\frac{A_R r}{E_R}\right); r \geq 0 \quad \& \quad A_R \geq 0, \tag{2.2}$$

where A_R is the peak amplitude of the dominant LOS signal and $J_0(x)$ is the Bessel function. It is worth noting that a Rayleigh distribution is just a special case of the Rician distribution with $A_R = 0$. The time-varying Rayleigh channel model can be computed as

$$\tilde{h}(t, \tau) = \sum_{l=0}^{L-1} \tilde{\alpha}(t, l)\, \delta(\tau - lT), \tag{2.3}$$

where

$$\tilde{\alpha}(t, l) = \sum_{i=1}^{N_s} a(i, l) \exp(\mathrm{j}2\pi f_{D_i} t), \tag{2.4}$$

where L is the total number of channel taps, $a(i, l)$ is the complex valued channel weight due to i^{th} scatterer at the delay lT and N_s is the total number of scatterers. $a(i, l) \geq 0 \quad \forall l = 0, ...L-1$ and $a(i, l) = 0 \quad \forall l < 0$ and $l \geq L$. Therefore, the channel impulse response is that of a finite impulse response (FIR) filter. Each scatterer i contributes to the summation with a ray incident from an angle θ_i and therefore different Doppler frequency shift (due to the motion) $f_{D_i} = f_{D,max} \cos\theta_i$. The maximum Doppler frequency $f_{D,max}$ is given by

$$f_{D,max} = \frac{f_c v}{c}, \tag{2.5}$$

where f_c is the carrier frequency, v is the velocity of the user and c is the speed of light. For more information about the time-varying multi-path channel model in (2.3), we refer to [Jak74]. $\tilde{h}(t, \tau)$ can be considered as a function ideally sampled in τ direction providing the samples $\tilde{\alpha}(t, l); l = 0, 1, ...L-1$. Sampling of $\tilde{h}(t, \tau)$ with T spaced Dirac impulses in t direction yields

$$\begin{aligned} \tilde{h}_s(t, \tau) &= \sum_{l=0}^{L-1} \tilde{\alpha}(t, l)\, \delta(\tau - lT) \sum_{n=-\infty}^{\infty} \delta(t - nT) \\ &= \sum_{n=-\infty}^{\infty} \sum_{l=0}^{L-1} \tilde{\alpha}(nT, l)\, \delta(\tau - lT)\, \delta(t - nT), \end{aligned} \tag{2.6}$$

with the corresponding two-dimensional discrete impulse response

$$h\left(n,\, l\right) = \tilde{\alpha}\left(nT,\, l\right). \tag{2.7}$$

With $\tilde{\alpha}\left(nT,\, l\right)$ from (2.3) we finally get

$$h\left(n,\, l\right) = \sum_{i=1}^{N_s} a\left(i,\, l\right) \exp\left(\mathrm{j}2\pi f_{D_i} nT\right) \quad n \in \mathbb{Z}, l = 0, 1, ..., L-1 \tag{2.8}$$

Taking the two dimensional (2D) N-point based fast Fourier transform (FFT) on $h\left(n,\, l\right)$ on the two dimensions n and l, and restricting n to the interval $[0, N-1]$, results in [STJ08]

$$\begin{aligned} H^F\left(d,\, k\right) &= \frac{1}{N} \sum_{n=0}^{N-1} \sum_{l=0}^{N-1} h\left(n,\, l\right) \exp\left(-\mathrm{j}\frac{2\pi}{N}\left(nd + lk\right)\right) \\ &= \frac{1}{N} \sum_{n=0}^{N-1} \sum_{l=0}^{N-1} \sum_{i=1}^{N_s} a\left(i,\, l\right) \exp\left(\mathrm{j}2\pi f_{D_i} nT\right) \exp\left(-\mathrm{j}\frac{2\pi}{N}\left(nd + lk\right)\right) \\ &= \frac{1}{N} \sum_{n=0}^{N-1} \sum_{l=0}^{L-1} \sum_{i=1}^{N_s} a\left(i,\, l\right) \exp\left(-\mathrm{j}\frac{2\pi kl}{N}\right) \exp\left(\mathrm{j}2\pi n\left(\frac{-d}{N} + f_{D_i} T\right)\right) \end{aligned} \tag{2.9}$$

where $\frac{-N}{2} \leq d < \frac{N}{2}$ and $0 \leq k \leq N-1$, $k, d \in \mathbb{Z}$.

The variation of $H^F\left(d,\, k\right)$ along the dimension d represents the spreading in the Doppler frequency domain because of the relative motion of the receiver. As we shall see in Chapter 3, this spreading is the source of ICI. Spreading in the delay domain is controlled by the multi-path channel, as mentioned above.

Interestingly, both phenomenon have a dual relationship to each other. On the one hand, the time delay spreading of the received signal due to a multi-path channel controls the channel coherence bandwidth, i.e., the frequency range over which the channel frequency response $H^F\left(d,\, k\right)$ can be approximated to be constant. A 50% coherence bandwidth can be computed as [Rap96] $B_c = \frac{1}{5\tau_{max}}$, where τ_{max} is the maximum channel impulse response delay spread. On the other hand, the Doppler frequency spread controls the coherence time, i.e., the period of time over which the channel impulse response $h\left(n,\, l\right)$ can be assumed to be constant. A 50% coherence time interval can be computed as [Rap96] $T_c = \frac{9}{16\pi f_{D,max}}$.

2.1.2. Multi-Carrier Transmission

The idea of OFDM has emerged a long time ago as early as the 1966 paper of Chang [Cha66]. However, it was only considered for practical implementation when an efficient implementation was proposed using the FFT. For more information about the history of the development of OFDM, the interested reader can refer to [Wei09].

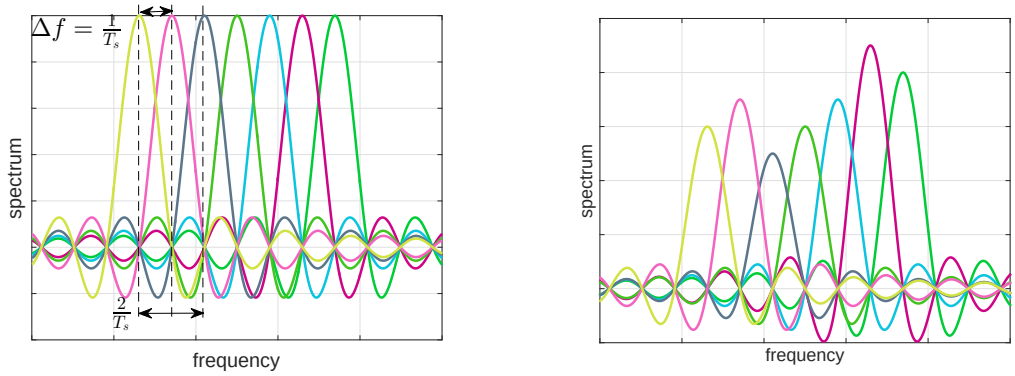

(a) Transmitted (b) Received

Figure 2.1.: Spectrum overlap of 7 subcarriers within an OFDM symbol

In general, if the symbol duration T_s is much larger than the maximum delay spread $T_s >> \tau_{max}$ or alternatively the signal bandwidth is much smaller than the coherence bandwidth $B_s << B_c$, the channel is considered as a "flat" channel, i.e., the received signal can be considered to be a version of the transmitted signal weighted by a complex scalar factor. Thus very low equalization effort is required. Indeed, this is exactly the basic idea of an OFDM system. The idea is to divide the total bandwidth of the signal B_s into smaller subchannels $B_{sc} = \frac{B_s}{N}$, referred to as subcarriers, and transmit the information in parallel over these subchannels. If the number of subchannels, N, is large enough such that $B_{sc} << B_c$, the channel experienced over every subchannel is "flat" and hence a zero-forcing (ZF) equalizer is sufficient to remove the distortion in the frequency domain. In the literature, it is common to refer to subchannels as subcarriers and to the subchannel bandwidth B_{sc} as the subcarrier spacing Δf. From here on, for convenience, we stick to this notation.

To provide the required orthogonality between the subcarriers:

1. The subcarriers are arranged in the frequency domain such that the frequency spacing between the subsequent subcarriers is $\Delta f = \frac{1}{T_s} = \frac{1}{NT}$, where T is the elementary period between two successive samples in the time domain. As shown in Figure 2.1, such an arrangement guarantees that at the frequency sampling point of any subcarrier k, no other contribution from any other subcarrier $k^{'} \neq k$ exists.

2. Every OFDM symbol is appended at the beginning by a guard interval (GI) which in practice contains a duplicate of the last N_{GI} samples of the OFDM symbol and hence is referred to as cyclic prefix (CP), where $N_{GI} \geq L - 1$.

The first requirement is sufficient to guarantee that subcarriers do not interfere with each other, at $k \in Z$, over a flat fading channel. With this requirement, every subcarrier within an OFDM symbol is located at an integer multiple of a basic frequency $\frac{1}{T_s}$. Since the dot product between two different sinusoids which are integer multiples of a

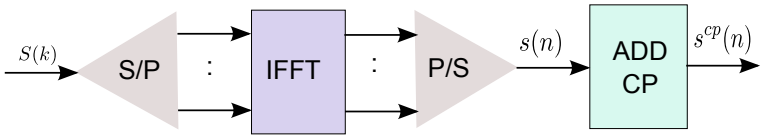

(a) OFDM transmitter block diagram

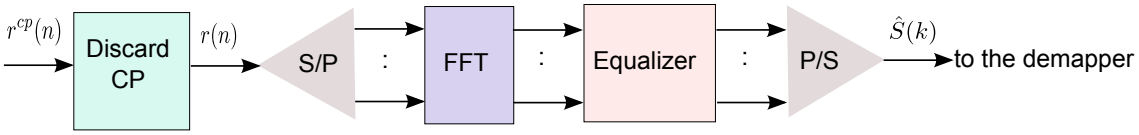

(b) OFDM receiver block diagram

Figure 2.2.: OFDM transmitter and receiver block diagrams

fundamental frequency, $\frac{1}{T_s}$, over a whole period (inverse of the fundamental frequency, i.e., T_s) is zero, orthogonality is satisfied over the symbol time T_s. This can be indicated in the following equation (see Chapter 11 in [Bul00])

$$\int_0^{T_s} \sin\left(\frac{m\pi t}{T_s}\right) \sin\left(\frac{n\pi t}{T_s}\right) dt = 0 \quad \forall m, n \in \mathbb{Z}, m \neq n. \tag{2.10}$$

The second requirement is necessary to guarantee the orthogonality over frequency selective fading channels. The CP has two advantages: first it avoids inter-block interference (IBI) between successive OFDM symbols. IBI can also be avoided with a zero GI between successive OFDM symbols. Second, it guarantees the orthogonality between each subcarrier and all the delayed versions (because of the echoes) of neighbor subcarriers and thus avoiding ICI. Another point of view to interpret the role of the CP is that, with it included, the received part of the OFDM symbol can be modeled as a circular convolution between the transmitted signal and the communication channel impulse response, which allows to map the time domain convolution to a multiplication in the frequency domain after applying an FFT operation [OSB99]

$$s\left(n\right) \circledast h\left(n\right) \Leftrightarrow S\left(k\right) H\left(k\right), \tag{2.11}$$

which greatly simplifies the task of the equalizer block since it now deals with equalizing a flat fading channel instead of a multi-path channel, assuming $B_{sc} << B_c$ as mentioned above.

In Chapter 3, we put down the mathematical model of the received OFDM signal, where the role of the CP is once again highlighted. The block diagrams of the OFDM transmitter and receiver are shown in Figures 2.2a and 2.2b, respectively.

2.2. Digital Terrestrial Broadcasting Systems

Figure 2.3 shows a map of the used terrestrial broadcasting systems around the world[1]. The most widely used system in Europe, Africa, Australia and most of Asia is the DVB-T system depicted in blue. Though initially designed for fixed rooftop antennas, it is reported that in networks dimensioned for portable indoor reception (e.g. Germany) it could be possible to provide commercial services to vehicles [GB13, Rei05]. In this case, techniques such as receive antenna diversity, hierarchical modulation and Application Layer– Forward Error Correction could increase the robustness of transmission [LSGBGC12].

The North American Advanced Television Systems Committee 2.0 (ATSC 2.0) A/53 [ATSa], developed in the early 1990s as one of the first digital terrestrial broadcasting standards, is based on a single carrier transmission scheme which uses vestigial sideband (VSB) modulation. The physical layer of the mobile handheld standard ATSC 2.0 A/153 was enhanced by more robust channel coding, time interleaving and more frequent training symbol sequences. ATSC 2.0 A/153 [ATS09] is also designed to be backward compatible with the A/53 fixed system. In March 2013, a call for proposals was made for the next Advanced Television Systems Committee 3.0 (ATSC 3.0) standard [ATSb]. In October 2013, Advanced Television Systems Committee (ATSC) announced the summary of responses [ATS13], including a proposal from the DVB. Most of the responses, including LG Electronics, Zenith and Harris Broadcast, Samsung and Sony, Technicolor and DVB proposed a multi-carrier based standard for the next generation broadcast television standard in North America. In particular, many proposals are based on DVB-T2.

The digital terrestrial broadcasting system in China Digital Terrestrial Multimedia Broadcast (DTMB), [dtm06] supports both single-carrier and multi-carrier modulation. A pseudo-noise (PN) sequence is used as a frame header to mitigate intersymbol interference (ISI) instead of a CP. In addition, Chinese Mobile Multi-Media Broadcast System (CMMB) is a mixed satellite/terrestrial broadcasting system designed to provide TV and radio services to vehicles and handheld devices with small screens. CMMB is based on OFDM modulation to mitigate multi-path fading.

T-DMB employed in South Korea and Integrated Services Digital Broadcasting-Terrestrial (ISDB-T) employed in Japan and South America have been successfully deployed for portable reception [CLB+07, FA08]. Except for a time interleaver and splitting the frequency band into 13 segments, ISDB-T is quite similar in architecture to DVB-T. Being the most widely deployed system in Europe, Asia and Africa and given the fact that solutions developed for mobile DVB-T and DVB-T2 reception can also be adopted in ISDB-T and next generation ATSC 3.0, we shall focus in this thesis on the DVB-T and DVB-T2 standards.

[1]The map, however, does not include Terrestrial Digital Media Broadcasting (T-DMB), the digital terrestrial broadcasting system in South Korea.

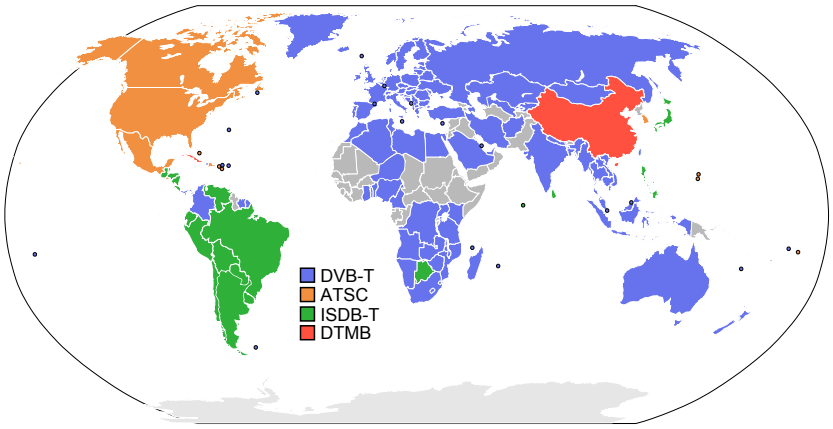

Figure 2.3.: Map of the employed terrestrial broadcasting standards worldwide from [Wik15].

2.3. DVB Family of Standards

DVB is a collection of international open standards for digital television, they include transmission over

1. Satellite: Digital Video Broadcast-Satellite Standard (DVB-S), Second Generation Digital Video Broadcast-Satellite Standard (DVB-S2) and Extended Second Generation Digital Video Broadcast-Satellite (DVB-S2X)

2. Cable television: Digital Video Broadcast-Cable Standard (DVB-C) and Second Generation Digital Video Broadcast-Cable Standard (DVB-C2)

3. Terrestrial television: DVB-T and DVB-T2

4. Handheld devices: Digital Video Broadcast Handheld Standard (DVB-H) and Digital Video Broadcast Next Generation Handheld (DVB-NGH)

In this thesis, we focus on mobile reception from terrestrial or handheld devices, For more information about the rest of the family of standards, the interested reader can refer to the comprehensive overview in [Rei05].

2.3.1. Digital Video Broadcasting-Terresterial (DVB-T/DVB-T2)

In Figure 2.4, we can see the block diagram of a DVB-T system [ETS09a, ETS11]. Reed Solomon codes are used as outer channel coding scheme. For input bit-error rate less than 2×10^{-4}, Reed Solomon codes are able to reduce the bit-error rate to about 10^{-11} [ETS11]. Convolutional codes are used as inner channel coding schemes. A convolutional interleaver is added as an outer interleaver with an interleaving depth $D_I = 12$. An inner frequency interleaver is built as a group of joined blocks of de-multiplexer, bit interleaver

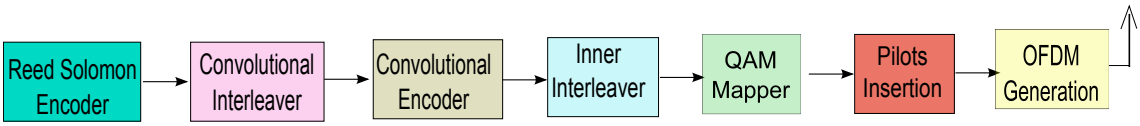

Figure 2.4.: DVB-T transmitter

and symbol-interleaver. After that comes the quadrature amplitude modulation (QAM) mapper which allows for $4, 16$ and 64QAM modulation schemes. Three types of reference information exist within a normal DVB-T OFDM symbol

1. transmitter parameter signalling (TPS) subcarriers are used for signaling parameters related to the transmission scheme

2. scattered pilot (SP) subcarriers are uniformly spaced inside an OFDM symbol and are used for channel estimation, as we shall see in section 2.4.

3. continual pilot (CoP) subcarriers, where 'continual' means they occur at all OFDM symbols. They are mainly used for fine synchronization and as we shall see later, for noise estimation.

SPs and CoPs are modulated according to a pseudo-random binary sequence (PRBS), $\mathbf{w}_{PRBS}(k)$, corresponding to their respective carrier index k. They are also boosted with a power of $\frac{16}{9}$. For more information about how to build the reference sequences, the interested reader can refer to [ETS09a, ETS11].

In Figure 2.5, we can see the block diagram of a DVB-T2 transmitter, which in comparison to a DVB-T transmitter has the following enhancements/features:

1. stronger channel codes: Using the capacity achieving low density parity check (LDPC) codes. A "quasi-error" free performance is achieved after Bose, Chaudhuri, and Hocquenghem (BCH) encoder, when the BER after LDPC is $< 10^{-7}$ [ITU12, ETS09b]. To keep simulation times reasonable, some references consider a BER of 10^{-4} after LDPC, which corresponds to a BER of 10^{-7} after BCH [Sch, SS13].

2. addition of a time interleaver whose depth can reach 1023 frames to provide better time diversity in mobile channels [GVGBC10].

3. eight possible pilot patterns (PP1 to PP8) with different pilot spacings, to cope with the needs of transmission over different channels.

4. rotated constellations and distributed multiple input single output (MISO) technique, based on the Alamouti code.

The abovementioned enhancements (and others which are not mentioned here but can be found in [DVB09, GB13]) allowed DVB-T2 to achieve 50% capacity increase over its predecessor [GB13, VBT$^+$09], at the expense of a significant increase in complexity and chip size. That is why the DVB Consortium has introduced the T2-Lite profile [ETS09b], which supports only a subset of DVB-T2 modes that are best suited for mobile reception.

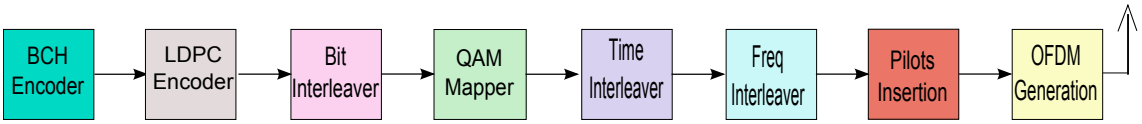

Figure 2.5.: DVB-T2 transmitter

In both standards DVB-T and DVB-T2, a guard band exists in the normal OFDM symbol, i.e., out of the N subcarriers only N_a subcarriers carry information and the rest are null subcarriers. Guard bands are required to limit adjacent channel interference as explained in Clause 4.3.2 in [ETS11]. The active subcarrier then consist of N_{data} data subcarriers and N_{pilots} pilots.

2.3.2. Digital Video Broadcasting-Handheld (DVB-H/DVB-NGH)

DVB-H reuses the physical layer of DVB-T with some enhancements over the link layer. This enabled DVB-H to share the network infrastructure of DVB-T [FA08]. The introduced enhancements are mostly over the link layer, and they include a power saving technique, which is quite useful for handheld devices known as time slicing and additional forward error correction (FEC) at the link layer. Although DVB-H was officially endorsed by the European Commission, commercial DVB-H services have been progressively switched off after being deployed in some European countries, because of the lack of a successful business model [GB13].

In 2009, the DVB group announced a call for technologies for the second generation of DVB-H, i.e., DVB-NGH. The standard was published in 2013. Further gains compared to the existing DVB-T2 are achieved via exploring the diversity in the three dimensions, by incorporating long time interleaving, time frequency slicing (TFS) and multiple input multiple output (MIMO) technology. Additional features can also be found extensively in [GB13, DVB12]. A major advantage of DVB-NGH is its ability to co-exist with DVB-T2 infrastructure thanks to the future extension frame (FEF)s of DVB-T2 [ETS09b]. FEFs are, according to the DVB-T2 specifications, silent periods of time which can be used to transmit something other than DVB-T2. This feature is introduced in the system to allow for co-existance with future modified systems.

2.3.3. DVB-T/T2 and DVB-NGH Channel Models

In [DVB09, ETS09a, NGH10], a list of the channel models for the terrestrial/handheld standards can be found. Among those, the following two channels are the most relevant to this work:

1. typical urban 6-tap channel (TU6) channel: defined originally in [COS89]. It emulates the terrestrial propagation in an urban channel. It comprises 6 taps which follow the classical Jakes Doppler spectrum. In Table 2.1, the channel power delay profile of the TU6 channel is listed.

Tap number	Delay [usec]	Power[dB]
1	0.0	−3
2	0.2	0
3	0.5	−2
4	1.6	−6
5	2.3	−8
6	5	−10

Table 2.1.: Typical urban 6 tap channel power delay profile

2. mobile TU6 based single frequency network (SFN). SFN is a network in which several transmitters are modulated with the same signal and broadcast at the same frequency. Owing to the robustness of OFDM against multi-path channels, the received signals from different transmitters can contribute constructively to the received OFDM signal as long as the maximum delay lies within the guard interval length. The maximum delay then determines the maximum allowed distance between transmitters within an SFN. Mobile TU6 based SFN emulates the terrestrial propagation in an urban area in an SFN, where it is the sum of all independent TU6 channel models, each representing a transmitter. We refer to this channel as single frequency network typical urban 6 tap channel (SFN-TU6). In [NGH10], SFN-TU6 is defined for the cases of two transmitters: double typical urban 6 tap channel (2TU6) and three transmitters: triple typical urban 6 tap channel (3TU6). In this work, we will be only interested in the 2TU6 channel defined with parameters τ_2 and k_2, which describe the delay and the gain of the second channel relative to the first one, given in sec and dB, respectively. In the z domain, the channel transfer function of the resultant 2TU6 channel can be written as

$$H_{2TU6}(z) = H_{TU6,1}(z) + 10^{(0.1k_2)} H_{TU6,2}(z)\, z^{\frac{-\tau_2}{T}}, \tag{2.12}$$

where $H_{TU6,1}(z)$ and $H_{TU6,2}(z)$ are two independent realizations of the TU6 channel from two different transmitters.

2.4. Channel Estimation in DVB-T/T2

In DVB-T/T2, the transmitted pilots used for channel estimation are scattered in the time and frequency domain as shown in Figure 2.6, and hence the name "scattered pilots". The pilot density is controlled via the parameters D_x and D_y, which control the pilot spacing in frequency and time respectively. The pattern shown in Figure 2.6 is for $D_x = 3$ and $D_y = 4$, which corresponds to the pilot pattern used in DVB-T and the PP1 pilot pattern used in DVB-T2. For more information about how the different pilots patterns in DVB-T/T2 can be built, the reader can refer to [ETS09a, ETS11, ETS09b, DVB09].

Channel estimation in DVB-T/T2 can be done using interpolation algorithms as in [MOP07, LC06, AK05] or using domain transfer methods [YS12]. In domain transfer methods, inverse fast Fourier transform (IFFT) is applied on the pilot symbols to get

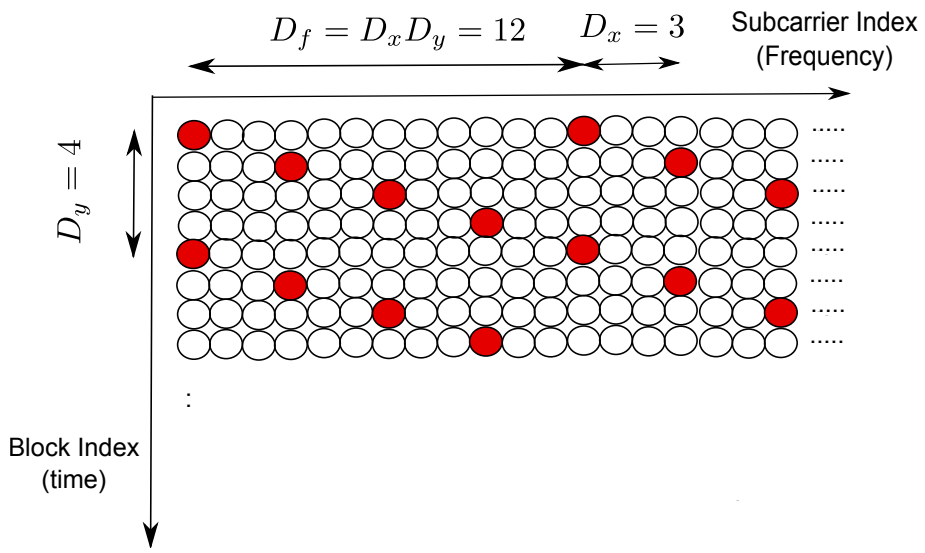

Figure 2.6.: SPs arrangement in DVB-T/T2

the channel impulse response (CIR) in the time domain. Noise reduction on the CIR is possible because the number of SPs in one OFDM symbol is larger than the number of channel taps [2] L, therefore suppressing the noisy taps at the end can lead to noise reduction. The channel frequency response (CFR) can be obtained by applying FFT on the obtained CIR. However, if the number of SPs is not a power of 2, as in our system because of the guard band, this technique can fail as explained in [Kow14, MOP07]. Therefore, in our work we do not consider further domain-transfer methods.

2.4.1. Channel Interpolation

Using the received SPs, the CFR can be estimated using interpolation algorithms. Using the sampling theorem, an upper bound for the pilot spacing in the time and frequency domains, for reliable construction of the CFR, is computed as [MOP07]

$$D_f \leq \frac{1}{\tau_{max} \Delta f} \tag{2.13}$$

$$D_t \leq \frac{1}{2 f_{D,max} \left(N + N_{GI}\right) T}. \tag{2.14}$$

Practically the distance should be reduced to half of that in (2.13) and (2.14) [MOP07, HKR97] to relax the requirements of the used interpolation filter, i.e., (2.13) and (2.14) can be re-written as

[2] This point will be clearer with the discussion presented next in section 2.4.1, where the maximum allowable distance between two pilots for successful channel estimation is studied.

$$D_f \leq \frac{1}{2\tau_{max}\Delta f} \tag{2.15}$$

$$D_t \leq \frac{1}{4f_{D,max}\left(N+N_{GI}\right)T}. \tag{2.16}$$

Note that the number of SPs per OFDM symbol N_{SP} is equivalent to

$$N_{SP} = \left\lfloor \frac{N}{D_f} \right\rfloor, \tag{2.17}$$

and given the fact that the denominator in (2.15) can be written as $\tau_{max}\Delta f = TL\Delta f = \frac{TL}{NT} = \frac{L}{N}$, (2.15) can be rewritten as

$$D_f \leq \frac{N}{2L}. \tag{2.18}$$

Equations (2.17) and (2.18) can be merged together as

$$N_{SP} = \frac{N}{D_f} \geq \frac{2LN}{N} = 2L, \tag{2.19}$$

which proves the aforementioned point at the beginning of this section concerning the relationship between the number of SPs and the channel length.

Channel estimation by interpolation requires a first step of obtaining initial channel estimates at the SPs positions. This can be done as

$$\hat{H}\left(k\right) = \frac{R\left(k\right)}{S\left(k\right)}, \quad \forall k \in \Omega_{SP} \tag{2.20}$$

where Ω_{SP} is the set which holds the indices of the SPs subcarrier positions, $R\left(k\right)$ and $S\left(k\right)$ are the received and transmitted signals at subcarrier position k, respectively.

As a second step, an interpolation is performed. Interpolation can be done in both time and frequency directions simultaneously or in two cascaded stages. In the cascaded scheme, performing time interpolation first provides additional reference points (i.e. a more denser grid) for the next step of frequency domain interpolation. In our case, however, with a fast time-varying channel and long FFT sizes, the pilot spacing in the time domain can no longer guarantee enough correlation between the reference points. For example, at a Doppler shift $f_{D,max} = 100\,\text{Hz}$, FFT size of $N = 8192$ subcarriers, a guard interval of $N_{GI} = 2048$ samples and an elementary period $T = \frac{7}{64}$ usec (8 MHz channel), $D_t \leq \frac{1}{4f_{D,max}(N+N_{GI})T} = 2.23$ which is smaller than the smallest pilot spacing in the most dense pilot pattern PP1. Therefore, we consider only 1D frequency interpolation schemes in this thesis.

Interpolation schemes include:

1. polynomial based interpolation: In general, as described in [Kow14], polynomial based interpolation (piece-wise or spline) can be implemented as a filtering technique, which can be more computationally efficient. Polynomial based interpolation schemes can be classified into

a) piece-wise interpolation: The CFR is divided into $\frac{N_{SP}-1}{i_o}$ segments, where i_o is the order of the polynomial used. For example, in linear interpolation, the channel is estimated as a linear function on the interval between every two consecutive SPs.

b) spline based interpolation as in [KHJ03, CEPB02, FAPBRB+11]. The CFR is divided into $N_{SP}-1$ segments, $Q_b \forall b \in [1, N_{SP}-1]$.
Figure 2.7 shows the difference between piece-wise interpolation and spline based interpolation. As shown, piece-wise interpolation results in abrupt changes in the slope of the fitted polynomials at the junction of the segments, since the channel estimate on each segment is calculated independently of the other segments. Spline based interpolation, on the other hand, can overcome such a problem by enforcing extra continuity constraints on the fitted curve [FAPBRB+11]. For a spline polynomial of order i_o, up to the $(i_o-1)^{st}$ derivatives of the polynomial at every segment are forced to be continuous at the junctions. For example using third order spline polynomial interpolation, the algorithm puts the constraint of continuity on the 0^{th}, 1^{st} and 2^{nd} derivative of the polynomial at the junctions as follows:

$$\begin{aligned} Q_b\left(k_{b+1}\right) &= Q_{b+1}\left(k_{b+1}\right) \\ \dot{Q}_b\left(k_{b+1}\right) &= \dot{Q}_{b+1}\left(k_{b+1}\right) \\ \ddot{Q}_b\left(k_{b+1}\right) &= \ddot{Q}_{b+1}\left(k_{b+1}\right), \end{aligned} \tag{2.21}$$

where $\dot{Q}_b$ and $\ddot{Q}_b$ are the first and second derivatives of the estimated channel at the b^{th} segment and k_{b+1} is the common scattered pilot between the two consecutive segments Q_b and Q_{b+1}. First order spline interpolation reduces to linear interpolation

2. low pass interpolation: For example in [LC06], a 1-D raised cosine filter is used to estimate the CFR. In general, the bandwidth of the low pass filter should achieve a trade-off between capturing the CFR and noise suppression.

3. Wiener interpolation [Hay01]: which gives the best performance. Based on an MMSE criteria, the optimum Wiener filter coefficients needed to estimate the subcarrier k can be found as

$$\mathbf{U}_{(N_{SP}\times 1)}(k) = \mathbf{R}^{-1}_{\hat{H}_p,(N_{SP}\times N_{SP})}\mathbf{P}_{(N_{SP}\times 1)}(k), \tag{2.22}$$

where $\mathbf{R}_{\hat{H}_p}$ is the autocorrelation matrix of $\hat{H}$ at the pilot subcarriers positions. $\mathbf{R}_{\hat{H}_p}$ can be built as

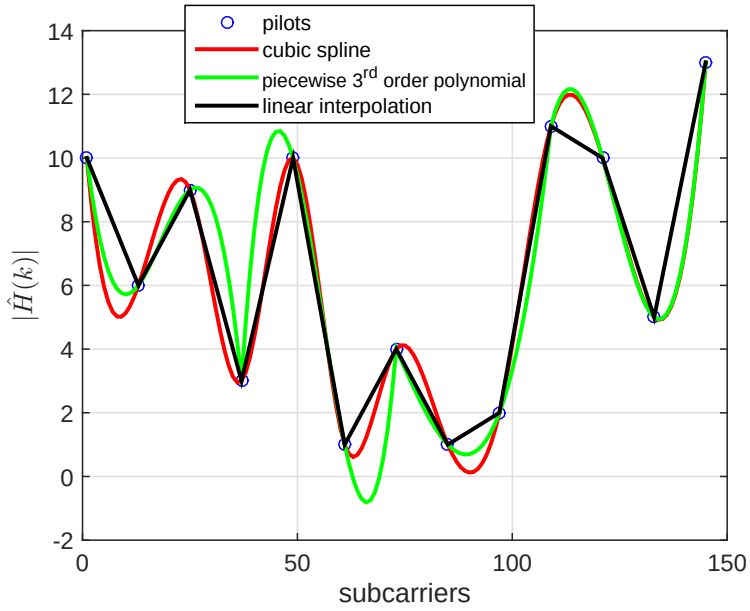

Figure 2.7.: Piece-wise Interpolation vs cubic spline

$$\mathbf{R}_{\hat{H}_p} = \begin{bmatrix} E\left\{\hat{H}_p(0)\,\hat{H}_p^*(0)\right\} & E\left\{\hat{H}_p(0)\,\hat{H}_p^*(1)\right\} & \dots & E\left\{\hat{H}_p(0)\,\hat{H}_p^*(N_{SP}-1)\right\} \\ E\left\{\hat{H}_p(1)\,\hat{H}_p^*(0)\right\} & E\left\{\hat{H}_p(1)\,\hat{H}_p^*(1)\right\} & \dots & E\left\{\hat{H}_p(1)\,\hat{H}_p^*(N_{SP}-1)\right\} \\ \vdots & \vdots & \ddots & \vdots \\ E\left\{\hat{H}_p(N_{SP}-1)\,\hat{H}_p^*(0)\right\} & E\left\{\hat{H}_p(N_{SP}-1)\,\hat{H}_p^*(1)\right\} & \dots & E\left\{\hat{H}_p(N_{SP}-1)\,\hat{H}_p^*(N_{SP}-1)\right\} \end{bmatrix}, \tag{2.23}$$

where $\hat{\mathbf{H}}_p$ is a $N_{SP} \times 1$ vector of the estimated channel at the pilot subcarrier positions, from (2.20). $\mathbf{P}(k)$ is the cross-correlation vector between the channel at the current subcarrier position k and the channel at the SP positions. $\mathbf{P}(k)$ can be computed as

$$\mathbf{P}(k) = \begin{bmatrix} E\left\{\hat{H}_p(k)\,\hat{H}_p^*(0)\right\} \\ E\left\{\hat{H}_p(k)\,\hat{H}_p^*(1)\right\} \\ \vdots \\ E\left\{\hat{H}_p(k)\,\hat{H}_p^*(N_{SP}-1)\right\} \end{bmatrix}. \tag{2.24}$$

In practice, $\mathbf{R}_{\hat{H}_p}$ and $\mathbf{P}(k)$ are computed given some knowledge about the channel model. It is common to assume an exponential delay profile and a Jakes Doppler spectrum to compute the channel auto-correlation in frequency and time domain respectively. In this case, knowledge of the maximum delay spread τ_{max} and the maximum Doppler shift $f_{D,max}$ are required to build the matrices $\mathbf{R}_{\hat{H}_p}$ and $\mathbf{P}(k)$. In reality, these pa-

rameters can be estimated with some error. In [Kow14], the effect of a mismatch in the estimation of these parameters is investigated. Because of its need to acquire information about the channel, Wiener interpolation is not further considered in this thesis.

As concluded in [Kow14, KHJ03], higher order polynomial interpolation can better track more frequency selective channels (or equivalently can support larger pilot spacing) compared to first order polynomial linear interpolation. However, higher order polynomial interpolation show higher sensitivity to additive white Gaussian noise (AWGN) and Doppler shifts [3]. In addition, higher order polynomial interpolation require higher complexity. Low pass filtering based methods can achieve a good suppression behavior if the filter bandwidth, frequency shift and roll-off factor are properly optimized for the estimated channel [Kow14]. Because our focus in this work is on developing low complexity algorithms for noisy mobile channels and to avoid the need of optimizing too many variables, we only use simple first order linear interpolation for channel estimation.

2.5. Noise Estimation in DVB-T/T2

Noise information after equalization is needed as an input to the demapper block for the computation of the log-likelihood ratio (LLR) information, needed in channel decoding. In addition, some equalization schemes require knowledge of the noise information, especially in multiple antenna reception, as we shall see in Chapter 3. In [ZM09, ZM10], a preamble based SNR estimation method is proposed. In [Li10], a low complexity blind algorithm is used to estimate the SNR of an OFDM signal. In this thesis, we compute the noise information per OFDM symbol using CoPs and we refer to this scheme as pilot assisted noise estimate (PANE). Conventionally, SNR information at the channel output is estimated per OFDM symbol for DVB-T/T2 signals as in [GEV12], which is valid as long as the white noise assumption is valid. The estimated noise variance per OFDM symbol can then be estimated as

$$\hat{\sigma^2} = \frac{1}{N_{CoP}} \sum_{\iota \in \Omega_{CoP}} \sigma^2(\iota) \tag{2.25}$$

where Ω_{CoP} is the set containing the indices of all N_{CoP} CoPs and N_{CoP} is the total number of CoPs per OFDM symbol and $\sigma^2(\iota)$ is the noise information at the ι^{th} CoP subcarrier position and is computed as

$$\sigma^2(\iota) = \|R(\iota) - H(\iota, \iota) S(\iota)\|^2 . \tag{2.26}$$

In section 4.4, we discuss an enhanced combining scheme which utilizes the colored nature of the ICI noise, where we propose a way to compute $\hat{\sigma^2}(k)$.

[3] As we shall see later, Doppler shift can also be regarded as a type of Gaussian noise.

3. Mobile Reception of Multi-Carrier Signals

3.1. Mobile Orthogonal Frequency Division Multiplexing

OFDM has emerged as an attractive modulation scheme in high speed communication systems. Its robustness against frequency selective channels and simple transciever structure made it the technique of choice in many digital broad-band applications, for example asymmetric digital subscriber line (ADSL), LTE and DVB. In section 2.1.2, we explained the motivation and the basic idea of an OFDM system, where the QAM symbol stream is de-multiplexed into N parallel low rate substreams, which are modulated over N subcarriers. The bandwidth of each subcarrier is small enough, $B_{sc} << B_c$, to assume a flat (non-selective) channel. Although the sent subcarriers overlap in time and frequency, the waveforms are designed to be orthogonal as discussed in section 2.1.2.

However, because of the poor localization characteristics of the rectangular impulse adopted, OFDM is sensitive to timing and frequency offsets. In addition, long FFT sizes renders the OFDM symbol sensitive to the time selectivity of the mobile channel. Time variations corrupt the orthogonality of the OFDM subcarriers, resulting in ICI. This has been a motivation for a new class of non-orthogonal waveforms which possesses better localization characteristics and are more immune against time-varying channels [WJK+14], currently investigated for the upcoming 5th generation mobile network (5G) standard.

In a wireless environment, the multi-path channel is time varying because of the mobility of the user giving rise to ICI. ICI could also arise because of unknown carrier frequency offset. This is, however, out of the scope of this thesis. In large FFT sizes, the total ICI impacting one subcarrier is the result of interferences from a large number of $N - 1$ subcarriers. Therefore, based on the central limit theorem (CLT), as noted in [HM11] and many references within, ICI is usually approximated as a source of Gaussian noise for large FFT sizes.

In this Chapter, we discuss the ICI model in an OFDM system due to a time varying multi-path channel. We describe some common receivers to deal with the ICI problem in SISO and SIMO systems.

3.1.1. Inter-Carrier Interference

At the transmitter side of an OFDM system, the time domain output of the IFFT block is given by

$$s(n) = \frac{1}{\sqrt{N}} \sum_{k=0}^{N-1} S(k)\, e^{\frac{\mathrm{j}2\pi kn}{N}}, \tag{3.1}$$

where $S(k)$ is the frequency domain QAM symbol at subcarrier k, and N is the FFT size. We assume the QAM symbols $S(k)$ to be i.i.d. symbols with unit energy,

$$E_S = E\left\{|S(k)|^2\right\} = 1. \tag{3.2}$$

Pilot subcarriers are boosted, as mentioned earlier in section 2.3.1, according to [ETS11, DVB09]. At the transmitter side, a cyclic prefix is inserted between successive OFDM symbols. If the channel impulse response is shorter than the length of the guard interval, as mentioned in section 2.1.2, ISI is eliminated.

At the receiver side, the sampled time domain signal is

$$\begin{aligned} r(n) &= s(n) \star h(n,\, l) + x(n) \\ &= \sum_{l=0}^{L-1} h(n,\, l)\, s(n-l) + x(n), \end{aligned} \tag{3.3}$$

where $\star$ is the convolution operator, $h(n,\, l)$ is the l^{th} tap of the time varying multi-path FIR channel model at the n^{th} time instant, L is the multi-path channel length and $x(n)$ is the AWGN signal in the time domain with noise variance σ^2. We assume the channel power is normalized to 1 thus the SNR at the receiver side, Γ, is defined as $\Gamma = -10 \log \sigma^2$.

Applying FFT at the receiver side (after removal of the cyclic prefix), we get the frequency domain signal

$$\begin{aligned} R(k) &= \frac{1}{\sqrt{N}} \sum_{n=0}^{N-1} r(n) e^{\frac{-\mathrm{j}2\pi kn}{N}} \\ &= \frac{1}{\sqrt{N}} \sum_{n=0}^{N-1} \sum_{l=0}^{L-1} h(n,\, l)\, s(n-l) e^{\frac{-\mathrm{j}2\pi kn}{N}} + \underbrace{\frac{1}{\sqrt{N}} \sum_{n=0}^{N-1} x(n)\, e^{\frac{-\mathrm{j}2\pi kn}{N}}}_{X(k)}, \end{aligned} \tag{3.4}$$

where $X(k)$ is the AWGN spectral component at subcarrier position k with noise variance σ^2. Plugging (3.1) into (3.4)

$$
\begin{aligned}
R(k) &= \frac{1}{N}\sum_{n=0}^{N-1}\sum_{l=0}^{L-1}\sum_{k'=0}^{N-1} h(n,\,l)\,S\left(k'\right)e^{\frac{\mathrm{j}2\pi k'(n-l)}{N}}e^{\frac{-\mathrm{j}2\pi kn}{N}} + X(k) \\
&= \frac{1}{N}\sum_{n=0}^{N-1}\sum_{l=0}^{L-1} h(n,\,l)\,S(k)\,e^{\frac{-\mathrm{j}2\pi kl}{N}} \\
&+ \frac{1}{N}\sum_{n=0}^{N-1}\sum_{l=0}^{L-1}\sum_{k'\neq k}^{N-1} h(n,\,l)\,S\left(k'\right)e^{\frac{-\mathrm{j}2\pi k' l}{N}}e^{\frac{-\mathrm{j}2\pi(k-k')n}{N}} + X(k) \\
&= S(k)\sum_{l=0}^{L-1} h^{avg}(l)\,e^{\frac{-\mathrm{j}2\pi kl}{N}} + \frac{1}{N}\sum_{k'\neq k}^{N-1} S\left(k'\right)\sum_{n=0}^{N-1}\sum_{l=0}^{L-1} h(n,\,l)\,e^{\frac{-\mathrm{j}2\pi k' l}{N}}e^{\frac{-\mathrm{j}2\pi(k-k')n}{N}} + X(k), \\
&= \underbrace{S(k)\,H(k)}_{desired} + \underbrace{\sum_{k'\neq k}^{N-1} S\left(k'\right)\frac{1}{N}\sum_{n=0}^{N-1}\sum_{l=0}^{L-1} h(n,\,l)\,e^{\frac{-\mathrm{j}2\pi k' l}{N}}e^{\frac{-\mathrm{j}2\pi(k-k')n}{N}}}_{ICI} + X(k), \qquad (3.5)
\end{aligned}
$$

where $h^{avg}(l) = \frac{1}{N}\sum_{n=0}^{N-1} h(n,\,l)$ is the average value of the time varying channel tap index l. $H(k)$ is a scaled version of the FFT of $h^{avg}(l)$ by a factor of $\sqrt{N}$. In fact, $H(k)$ is equivalent to $H^F(d,\,k)$ given in (2.9), for $d = 0$, i.e, $H(k) = H^F(0,\,k)$.

The first term thus indicates the contribution of $S(k)$ on $R(k)$. The second term is the interference of every other sent subcarrier $S\left(k'\right)$ on $R(k)$. In case of a static channel, i.e., channel is no longer dependent on n, $h(n,\,l) = h(l)$, the second term will vanish since

$$
\begin{aligned}
\frac{1}{N}\sum_{n=0}^{N-1}\sum_{l=0}^{L-1} h(n,\,l)\,e^{\frac{-\mathrm{j}2\pi k' l}{N}}e^{\frac{-\mathrm{j}2\pi(k-k')n}{N}} &= \sum_{l=0}^{L-1} h(l)\,e^{\frac{-\mathrm{j}2\pi k' l}{N}}\frac{1}{N}\sum_{n=0}^{N-1} e^{\frac{-\mathrm{j}2\pi(k-k')n}{N}} \\
&= \sum_{l=0}^{L-1} h(l)\,e^{\frac{-\mathrm{j}2\pi k' l}{N}}\delta(k-k'), \qquad (3.6)
\end{aligned}
$$

which is zero for $k' \neq$k.

The ICI includes the term $\frac{1}{N}\sum_{n=0}^{N-1}\sum_{l=0}^{L-1} h(n,\,l)\,e^{\frac{-\mathrm{j}2\pi k' l}{N}}e^{\frac{-\mathrm{j}2\pi(k-k')n}{N}}$, which we can recognize as the 2D N based FFT transform of the time-varying multi-path channel $h(n,\,l)$ presented in (2.9) as $H^F\left(d,\,k'\right)$, with d referred to as subcarrier off-diagnal distance defined as $d = k - k'$. Thus,

$$
H^F\left(k-k',\,k'\right) = \frac{1}{N}\sum_{n=0}^{N-1}\sum_{l=0}^{L-1} h(n,\,l)\,e^{\frac{-\mathrm{j}2\pi k' l}{N}}e^{\frac{-\mathrm{j}2\pi(k-k')n}{N}} \qquad (3.7)
$$

represents the interference of subcarrier $k^{'}$ on subcarrier k.

In the rest of this thesis, we shall use $H\left(k,\, k^{'}\right)$ instead of $H^{F}\left(k-k^{'},\, k^{'}\right)$ to indicate the ICI effect of subcarrier $k^{'}$on subcarrier k. Equation (3.5) can then be written as

$$R\left(k\right)=H\left(k,\, k\right)S\left(k\right)+\sum_{k^{'}\neq k}H\left(k,\, k^{'}\right)S\left(k^{'}\right)+X\left(k\right)\quad\forall k,=0,1,\ldots,N-1. \tag{3.8}$$

Equation (3.8) can be written in a matrix form as follows

$$\mathbf{R}_{(N\times1)}=\mathbf{H}_{(N\times N)}\mathbf{S}_{(N\times1)}+\mathbf{X}_{(N\times1)}, \tag{3.9}$$

where $\mathbf{R}$ is the output vector of the FFT at the receiver side, $\mathbf{S}$ is the vector of the QAM symbols at the transmitter side and $\mathbf{X}$ is the vector of the noise subcarriers. $\mathbf{H}$ is the frequency domain channel matrix given by

$$\mathbf{H}=\mathbf{F}_{N}\mathbf{g}^{CP}\mathbf{F}_{N}^{H}, \tag{3.10}$$

where $\mathbf{g}^{CP}$ is the original $(N\times N)$ time delay channel matrix after dropping the CP, which can be constructed as $g^{CP}\left(n,l\right)=h\left(n,\,\left(n-l\right)_{N}\right)$. $\mathbf{F}_{N}$ is the $(N\times N)$ normalized FFT matrix, built as

$$F\left(r,\, c\right)=\frac{1}{\sqrt{N}}e^{\frac{-j2\pi rc}{N}}. \tag{3.11}$$

In the case of a static channel, $\mathbf{g}^{CP}$ is a circulant matrix built as [WBZS10]

$$\mathbf{g}^{CP}=\begin{bmatrix} h\left(0\right) & 0 & \ldots & 0 & h\left(L-1\right) & \ldots & h\left(1\right)\\ \vdots & \ddots & \ddots & & \ddots & \ddots & \vdots\\ \vdots & & \ddots & \ddots & & \ddots & h\left(L-1\right)\\ h\left(L-1\right) & & & \ddots & & & 0\\ 0 & \ddots & & & \ddots & \ddots & \vdots\\ \vdots & \ddots & \ddots & & & \ddots & 0\\ 0 & \ldots & 0 & h\left(L-1\right) & \ldots & \ldots & h\left(0\right) \end{bmatrix} \tag{3.12}$$

and hence is diagonalizable by the FFT matrix. This is due to the fact that the eigenvectors of a circulant matrix are the columns of a Fourier matrix of the same size. This means that in (3.8), $H\left(k,\, k^{'}\right)=0\quad\forall k\neq k^{'}$ and hence there is no ICI. In case of a time varying channel, the off-diagonal coefficients of the matrix $\mathbf{H}$ are no longer zero, resulting in ICI. The higher the Doppler shift, the higher the magnitudes of the off-diagonal coefficients and the more effective the ICI is. In Figures 3.1 and 3.2, the coefficients of the normalized channel matrix $\mathbf{H}_{n}$ are depicted for a flat fading channel at different normalized Doppler shifts $f_{D,norm}$ of 1×10^{-4} and 0.2 respectively, where $f_{D,norm}$ is defined as

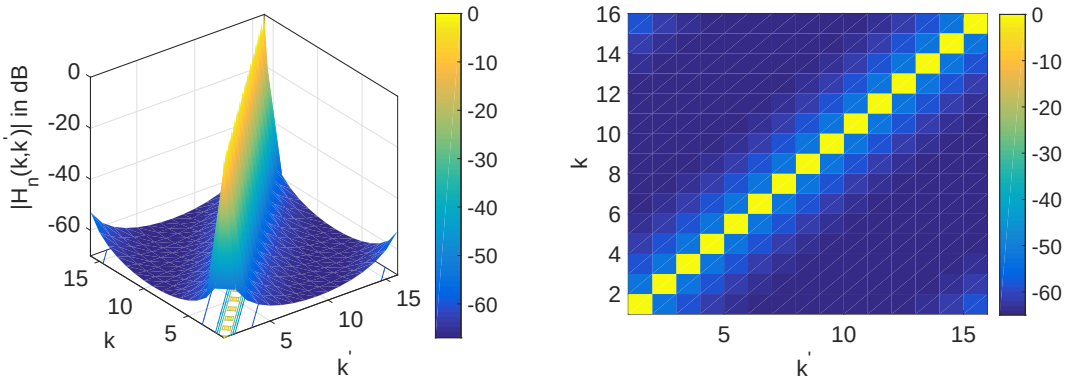

(a) 3D plot of the coefficients in the channel matrix $\mathbf{H}_n$ using a frequency flat fading channel and at a normalized Doppler frequency of 1e-4

(b) 2D contour of the coefficients in the channel matrix $\mathbf{H}$ using a frequency flat fading channel and at a normalized Doppler frequency of 1e-4.

Figure 3.1.: The coefficients in the channel matrix $\mathbf{H}$ using a frequency flat fading channel and at a normalized Doppler frequency of 1e-4

$$f_{D,norm} = \frac{f_{D,max}}{\Delta f}. \tag{3.13}$$

The elements inside the channel matrix $\mathbf{H}_n$ are normalized with respect to the main diagonal, $H_n\left(k,\, k^{'}\right) = \frac{H\left(k,k^{'}\right)}{H(k,k)}$.

As can also be noted, most of the energy outside the main diagonal in $\mathbf{H}$ is concentrated in the few off-diagonals around the main diagonal, and decreases steadily as the distance from the main diagonal increases. This property is proven to be very useful, since the matrix can often be approximated by its banded version, where only a limited number of $2D$ diagonals, around the main diagonal, need to be considered rather than the whole $(N \times N)$ matrix. In such case, D denotes the number of diagonals in each direction around the main diagonal. As we shall see, this approximation can significantly reduce the complexity of the receiver equalization step. The higher the Doppler shift, the more energy is 'leaked' outside the main diagonal, and hence a higher value of D has to be considered for a more accurate approximation of the matrix $\mathbf{H}$.

We can also notice the existence of high energy regions at the edges of the matrix. This is because of the circular nature of the ICI, the subcarriers at the edge of the OFDM symbol interfere with those at the beginning of the OFDM symbol. In other words, the subcarrier at the 0^{th} position receives equally strong interference from the subcarriers at positions $N-1$ and 1.

3.1.2. Inter-Carrier Interference in a Frequency Selective Channel

From (3.8), the interference signal $I\,(k)$ can be written as

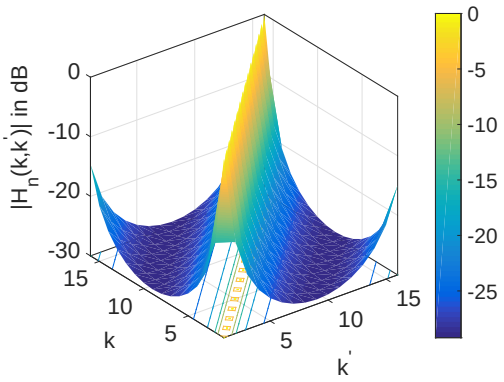

(a) 3D plot of the coefficients in the channel matrix $\mathbf{H}_n$ using a frequency flat fading channel and at a normalized Doppler frequency of 0.2

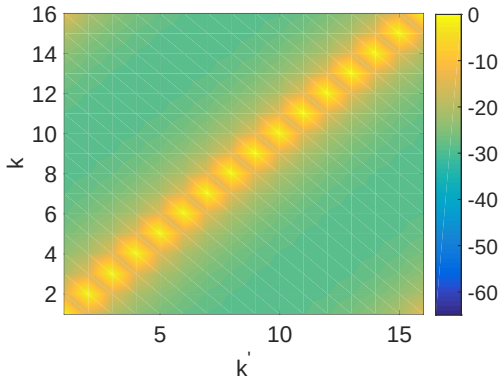

(b) 2D contour of the coefficients in the channel matrix $\mathbf{H}_n$ using a frequency flat fading channel and at a normalized Doppler frequency of 0.2.

Figure 3.2.: The coefficients in the channel matrix $\mathbf{H}_n$ using a frequency flat fading channel and at a normalized Doppler frequency of 0.2

$$I(k) = R(k) - H(k,\, k)\, S(k) - X(k) = \sum_{k' \neq k} H\left(k,\, k'\right) S\left(k'\right). \tag{3.14}$$

The expected value of the ICI power can then be written as

$$\begin{aligned} E\left\{\left|I(k)\right|^2\right\} &= E\left\{I(k)\, I^*(k)\right\} \\ &= E\left\{\sum_{k' \neq k} H\left(k,\, k'\right) S\left(k'\right) \sum_{k' \neq k} H^*\left(k,\, k'\right) S^*\left(k'\right)\right\}. \end{aligned} \tag{3.15}$$

Assuming an uncorrelated source with zero mean, $E\left\{S(k)\, S^*\left(k'\right)\right\} = 0 \quad \forall k \neq k'$ and no correlation between $H\left(k,\, k'\right)$ and $S\left(k'\right)$

$$\begin{aligned} E\left\{\left|I(k)\right|^2\right\} &= E\left\{\sum_{k' \neq k} \left|H\left(k,\, k'\right)\right|^2 \left|S\left(k'\right)\right|^2\right\} \\ &= E_S E\left\{\sum_{k' \neq k}^{N-1} \left|H\left(k,\, k'\right)\right|^2\right\} \overset{(3.2)}{=} E\left\{\sum_{k' \neq k}^{N-1} \left|H\left(k,\, k'\right)\right|^2\right\}. \end{aligned} \tag{3.16}$$

Equation (3.16) indicates that the colored nature of the ICI power stems from the colored nature of the off-diagonal ICI coefficients. In Figure 3.3, we show the magnitudes

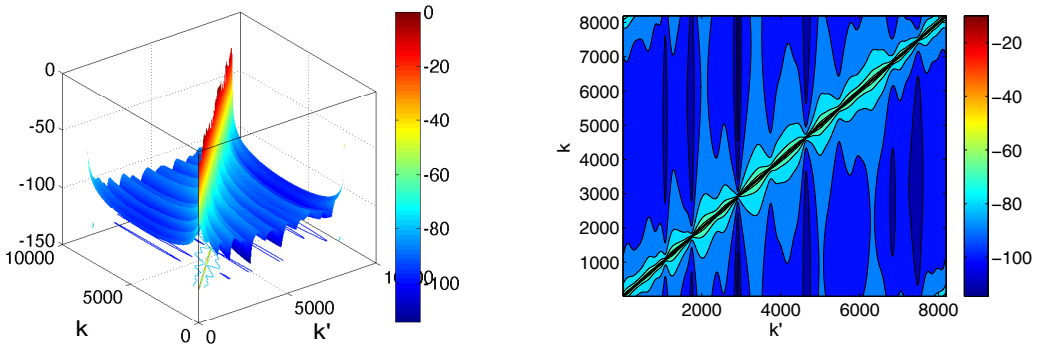

(a) 3D plot of the normalized absolute values of the coefficients in the channel matrix $\mathbf{H}_n$ of the TU6 channel and at a normalized Doppler frequency of 0.2

(b) 2D contour of the normalized absolute values of the coefficients in the channel matrix $\mathbf{H}_n$ of the TU6 channel and at a normalized Doppler frequency of 0.2.

Figure 3.3.: The coefficients in the channel matrix $\mathbf{H}_n$ of the TU6 channel and at a normalized Doppler frequency of 0.2

of the normalized coefficients of $\mathbf{H}_n\left(k,\, k^{'}\right)$ for a frequency selective channel, namely the TU6 channel, defined in section 2.3.3, using an 8k FFT. Unlike the Toeplitz structure in the $2D$ flat fading channel matrix shown in Figure 3.1 and 3.2, the frequency selectivity of the channel matrix shown in Figure 3.3 is clearly visible in the main diagonal as well as in the off-diagonal coefficients.

In Figure 3.4, we plot the normalized ICI power computed as $\left|I_{norm}\left(k\right)\right|^2 = \frac{|I(k)|^2}{\frac{1}{N}\sum_{k=0}^{N-1}|I(k)|^2}$ for a 64 point FFT OFDM symbol at a normalized Doppler frequency $f_{D,norm} = 0.2$ for a 64QAM constellation, where $I\left(k\right)$ is computed using (3.14). The frequency selectivity of the interference signal is clearly visible in the doubly selective channel (frequency selective and time selective) compared to the flat fading time varying channel. In other words, different subcarriers undergo different levels of ICI in a doubly selective channel. This observation served as a motivation for two proposed receiver architectures namely: an MMSE-ASW ICIC explained in section 3.2.1.1 and an enhanced MRC scheme explained in section 4.4.

3.1.3. Inter-Carrier Interference Modeling

Various models have been proposed to describe ICI in mobile OFDM systems. We follow models based on Taylor expansions [pMGLHB07, MC05, Ser12]. Up to a normalized Doppler shift of 20%, a linear approximation is sufficient [MC05] over a time duration T_s . It uses information about the time evolution of the average channel $h^{avg}\left(l\right)$ between two successive OFDM symbols. Therefore we consider only a first order Taylor approximation. In the following, we derive a piece-wise linear channel model with a constant slope over the time duration $2T_s$ (previous and next OFDM symbols) to approximate

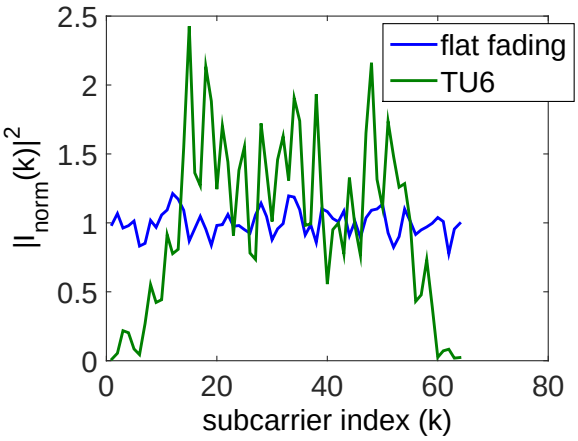

Figure 3.4.: Normalized ICI power per frequency bin $|I_{norm}(k)|^2$

the channel time variations[1].

Starting with (3.3), the time domain received signal can be written as

$$\begin{aligned} r(n) &= \sum_{l=0}^{L-1} h(n,\, l)\, \frac{1}{\sqrt{N}} \sum_{k=0}^{N-1} S(k)\, e^{\frac{\mathrm{j}2\pi k(n-l)}{N}} + x(n) \\ &= \frac{1}{\sqrt{N}} \sum_{k=0}^{N-1} \underbrace{\sum_{l=0}^{L-1} h(n,\, l)\, e^{\frac{-\mathrm{j}2\pi kl}{N}}}_{H_k(n)} S(k)\, e^{\frac{\mathrm{j}2\pi kn}{N}} + x(n) \\ &= \frac{1}{\sqrt{N}} \sum_{k=0}^{N-1} H_k(n)\, S(k)\, e^{\frac{\mathrm{j}2\pi kn}{N}} + x(n)\,, \end{aligned} \tag{3.17}$$

where $H_k(n)$ is the CFR of subcarrier k at time index n. The channel information acquired through the pilot assisted channel estimate (PACE) represents the time domain average channel throughout the N time instants $h^{avg}(l)$ [Kaz11]. In addition, it can be demonstrated that the mean squared error (MSE) $E\left[|h^{avg}(l) - h(n,\, l)|^2\right]$is minimized for $n_0 = \frac{N}{2}$-1$\approx \frac{N-1}{2}$ [MC05]. Therefore, we consider linearization of $H_k(n)$ around the middle point n_0 using Taylor series expansion as:

$$H_k(n) \approx H_k(n_0) + \dot{H}_k(n_0)\,(n - n_0)\,. \tag{3.18}$$

where $\dot{H}_k(n_0)$ is the first derivative of the CFR of subcarrier k at time index n_0. Plugging (3.18) in (3.17) and applying FFT, the received signal at subcarrier position k can be approximated as [pMGLHB07]

[1]With the longer duration over which the channel is assumed constant, we expect an upper limit of 10% normalized Doppler shift over which the linear approximation is valid.

$$
\begin{aligned}
R(k) &= \frac{1}{\sqrt{N}} \sum_{n=0}^{N-1} r(n) e^{\frac{-\mathrm{j}2\pi kn}{N}} \\
&= \frac{1}{N} \sum_{k'=0}^{N-1} \sum_{n=0}^{N-1} H_{k'}(n) S\left(k'\right) e^{\frac{-\mathrm{j}2\pi\left(k-k'\right)n}{N}} + X(k) \\
&\overset{(3.18)}{\approx} \sum_{k'=0}^{N-1} H_{k'}(n_0) S\left(k'\right) \underbrace{\frac{1}{N} \sum_{n=0}^{N-1} e^{\frac{-\mathrm{j}2\pi\left(k-k'\right)n}{N}}}_{\delta\left(k-k'\right)} \\
&+ \frac{1}{N} \sum_{k'=0}^{N-1} \dot{H}_{k'}(n_0) S\left(k'\right) \sum_{n=0}^{N-1} (n-n_0) e^{\frac{-\mathrm{j}2\pi\left(k-k'\right)n}{N}} + X(k) \\
&\approx H_k(n_0) S(k) + \sum_{k'=0}^{N-1} \dot{H}_{k'}(n_0) \Xi\left(k,\, k'\right) S\left(k'\right) + X(k), \qquad (3.19)
\end{aligned}
$$

where the leakage coefficient $\Xi\left(k,\, k'\right)$ is written as

$$
\Xi\left(k,\, k'\right) = \frac{1}{N} \sum_{n=0}^{N-1} (n-n_0) e^{\frac{-\mathrm{j}2\pi\left(k-k'\right)n}{N}}. \qquad (3.20)
$$

$\dot{H}_{k'}(n_0) \Xi\left(k,\, k'\right) S\left(k'\right)$ denotes the ICI effect of subcarrier k' on subcarrier k. Note that $\Xi(k,\, k) = 0$. For small values of $\frac{\left|k-k'\right|}{N}$, $\Xi\left(k,\, k'\right)$ can be approximated as [Ser12, STJ08]

$$
\Xi\left(k,\, k'\right) \approx \frac{1}{-\mathrm{j}\sin\left(\frac{2\pi\left(k-k'\right)}{N}\right)} \approx \frac{N}{-\mathrm{j}2\pi\left(k-k'\right)} = \frac{N}{-\mathrm{j}2\pi d}, \qquad (3.21)
$$

It can be noticed how the value of the leakage coefficient $\Xi\left(k,\, k'\right)$ decreases as the absolute value of the off-diagonal distance $|d|$ increases. This is intuitively satisfying since closer subcarriers have stronger interference effect compared to further ones.

The channel derivative of each subcarrier, $\dot{H}_{k'}(n_0)$, can be obtained as:

$$
\dot{H}_{k'}(n_0) = \frac{H_{k'}^{+1}(n_0) - H_{k'}^{-1}(n_0)}{2N}, \qquad (3.22)
$$

where $H_{k'}^{+1}(n_0)$ and $H_{k'}^{-1}(n_0)$ are the estimated channel coefficients from the following and previous OFDM symbols respectively. As mentioned earlier, these coefficients can be estimated using PACE. Equation (3.22) indicates that in order to compute the ICI

coefficients based on first order Taylor expansion, three OFDM symbols have to be buffered, such that the ICI coefficients of the middle OFDM symbol are computed.

Comparing (3.8) with (3.19), the ICI coefficient $H\left(k,\, k^{'}\right)$ can be computed using (3.21) and (3.22) as

$$\begin{aligned} H\left(k,\, k^{'}\right) &= \dot{H}_{k^{'}}\left(n_0\right)\Xi\left(k,\, k^{'}\right) \\ &\overset{(3.21,3.22)}{\approx} \mathrm{j}\frac{H^{+1}\left(k^{'},\, k^{'}\right) - H^{-1}\left(k^{'},\, k^{'}\right)}{4\pi\left(k-k^{'}\right)} \\ &= \kappa\frac{v\left(k^{'}\right)}{k-k^{'}}, \quad k \neq k^{'} \end{aligned} \tag{3.23}$$

where $H^{+1}\left(k^{'},\, k^{'}\right) = H_{k^{'}}^{+1}\left(n_0\right)$, $H^{-1}\left(k^{'},\, k^{'}\right) = H_{k^{'}}^{-1}\left(n_0\right)$,$\kappa = \frac{\mathrm{j}}{4\pi}$, $v\left(k^{'}\right) = H^{+1}(k^{'},k^{'}) - H^{-1}(k^{'},k^{'})$.

3.2. Algorithms for Single Input Single Output Equalizers

At the receiver side, the PACE block is used to estimate the channel coefficients which represent the elements on the main diagonal of the channel frequency matrix. In a static environment, the channel frequency matrix consists only of that main diagonal. Therefore, only a simple ZF operation is needed to recover the symbol estimates. In a mobile environment, using only ZF, and thereby neglecting the ICI, would result in an error floor in the BER which increases as the Doppler shift increases.

From (3.21), we can see that the magnitude of the off-diagonal coefficients decreases with $\frac{1}{|d|}$, as the distance from the main diagonal d increases. This is demonstrated in Figures 3.1 and 3.2. As mentioned earlier, this banded structure of the channel frequency matrix allows us to ignore the off-diagonal coefficients after a certain offset D from the main diagonal, as shown in Figure 3.5. In this section, we introduce the classical equalizer algorithms, which we apply to mitigate ICI in OFDM signals, namely MMSE based equalization and PIC. In this work, we also refer to an equalizer block which considers ICI (not ZF) as ICIC. We rely on the aforementioned linear model in (3.23) to calculate the off-diagonal coefficients in the channel frequency matrix.

3.2.1. Minimum Mean Squared Error ICIC

Recalling the linear model in (3.9)

$$\mathbf{R}_{(N\times 1)} = \mathbf{H}_{(N\times N)}\mathbf{S}_{(N\times 1)} + \mathbf{X}_{(N\times 1)}. \tag{3.24}$$

An MMSE receiver seeks minimizing the mean square error given by

$$||\mathbf{S}_{(N\times 1)} - \hat{\mathbf{S}}_{(N\times 1)}||^2, \tag{3.25}$$

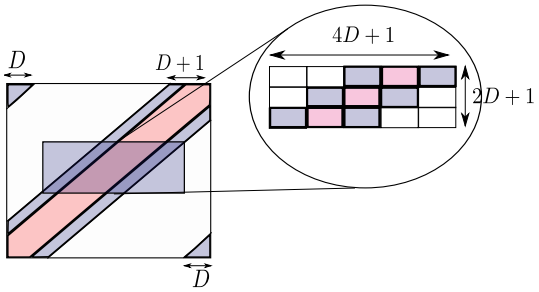

Figure 3.5.: Banded Matrix Structure and Sliding Window

where $\hat{\mathbf{S}} = \tilde{\mathbf{W}}^H_{f,(N\times N)}\mathbf{R}$.

$\tilde{\mathbf{W}}_{f,(N\times N)}$ is the MMSE receiver matrix computed as [Kay93]

$$\tilde{\mathbf{W}}_{f,(N\times N)} = (\mathbf{H}\mathbf{H}^H + \mathbf{C}_{\text{Noise}})^{-1}\mathbf{H}, \tag{3.26}$$

where ^{H} is the Hermitian operator and $\mathbf{C}_{\text{Noise}}$ is the noise covariance matrix, set as $\mathbf{C}_{\text{Noise}} = \sigma^2\mathbf{I}$ in an AWGN environment. More elaboration about how $\mathbf{C}_{\text{Noise}}$ is built in our system can be found in section A.1.

With large FFT sizes, such as N = 8k, the complexity of computing the matrix $\tilde{\mathbf{W}}_{f,(N\times N)}$ according to (3.26) becomes prohibitive. A more practical approach is to use a sliding window of size $(2D + 1 \times 4D + 1)$ [LKAD06] like the one shown in Figure 3.5. In this approach, the algorithm iterates over all subcarriers from 0 to $N - 1$, each iteration centering the window over the corresponding subcarrier and thus considering only $2D$ sub- and super off-diagonals while ignoring the rest. The corresponding system model can then be written as

$$\bar{\mathbf{R}}_{(2D+1\times 1)}(k) = \bar{\mathbf{H}}_{(2D+1\times 4D+1)}(k)\bar{\mathbf{S}}_{(4D+1\times 1)}(k) + \bar{\mathbf{X}}_{(2D+1\times 1)}(k), \tag{3.27}$$

where the window of received subcarrier symbols $\bar{\mathbf{R}}(k)$, the vector of sent symbol subcarriers $\bar{\mathbf{S}}_{(4D+1\times 1)}(k)$ and the vector of noise subcarriers $\bar{\mathbf{X}}(k)$ are defined as

$$\bar{\mathbf{R}}(k) = \begin{bmatrix} R(k-D) \\ \vdots \\ R(k) \\ \vdots \\ R(k+D) \end{bmatrix}, \tag{3.28}$$

$$\bar{\mathbf{S}}_{4D+1\times 1}(k) = \begin{bmatrix} S(k-2D) \\ \vdots \\ S(k) \\ \vdots \\ S(k+2D) \end{bmatrix} \tag{3.29}$$

and

$$\bar{\mathbf{X}}(k) = \begin{bmatrix} X(k-D) \\ \vdots \\ X(k) \\ \vdots \\ X(k+D) \end{bmatrix}. \tag{3.30}$$

The MMSE receiver matrix is then computed only for a subchannel matrix $\bar{\mathbf{H}}$ of size $(2D+1 \times 4D+1)$ instead of that of size $(N \times N)$

$$\tilde{\mathbf{W}}_{f,(2D+1\times 4D+1)}(k) = (\bar{\mathbf{H}}(k)\,\bar{\mathbf{H}}^{H}(k) + \bar{\mathbf{C}}_{\text{Noise,(2D+1×2D+1)}})^{-1}\bar{\mathbf{H}}(k). \tag{3.31}$$

The subchannel matrix $\bar{\mathbf{H}}$ is written for $D = 1$ as

$$\bar{\mathbf{H}}(k) = \begin{bmatrix} H(k-1,\,k-2) & H(k-1,\,k-1) & H(k-1,\,k) & 0 & 0 \\ 0 & H(k,\,k-1) & H(k,\,k) & H(k,\,k+1) & 0 \\ 0 & 0 & H(k+1,\,k) & H(k+1,\,k+1) & H(k+1,\,k+2) \end{bmatrix}. \tag{3.32}$$

The overall complexity of the windowed MMSE-ICIC approach is then $O(N(2D+1)^3)$ compared to $O(N^3)$ when the full matrix is used as in (3.26). In this case, however, the noise variance includes the variance of the AWGN plus the residual ICI power due to the unconsidered interferers outside the window range. The reader can refer to Appendix A for more information.

The windowed MMSE-ICIC is applied differently to every subcarrier. Therefore the filtering vector $\tilde{\mathbf{W}}_{f,(2D+1\times 1)}$ is computed as

$$\tilde{\mathbf{W}}_{f,(2D+1\times 1)}(k) = (\bar{\mathbf{H}}(k)\,\bar{\mathbf{H}}^{H}(k) + \bar{\mathbf{C}}_{\text{Noise,(2D+1×2D+1)}})^{-1}\mathbf{H}_{main,(2D+1\times 1)}(k), \tag{3.33}$$

where $\mathbf{H}_{main,(2D+1\times 1)}(k) = \begin{bmatrix} H(k-1,\,k) \\ H(k,\,k) \\ H(k+1,\,k) \end{bmatrix}$ is the middle column of $\bar{\mathbf{H}}(k)$ and thus $\tilde{\mathbf{W}}_{f,(2D+1\times 1)}(k)$ is the middle row of $\tilde{\mathbf{W}}_{f,(2D+1\times 4D+1)}(k)$ in (3.31). The sent symbol on subcarrier k is estimated as

$$\tilde{S}(k) = \tilde{\mathbf{W}}^{H}_{f,(2D+1\times 1)}(k)\,\bar{\mathbf{R}}(k). \tag{3.34}$$

After filtering with $\tilde{\mathbf{W}}_{f,(2D+1\times 1)}$, $\tilde{S}(k)$ still needs to be normalized as follows

$$\hat{S}(k) = \frac{1}{\tilde{\mathbf{W}}^{H}_{f,(2D+1\times 1)}(k)\,\mathbf{H}_{main,(2D\times 1)}(k)}\tilde{S}(k). \tag{3.35}$$

3.2.1.1. Adaptive Sliding Window MMSE ICIC

In [ALS14], we have proposed an MMSE ICIC with an adaptive sliding window, namely MMSE-ASW ICIC.

The idea of MMSE-ASW ICIC is to adopt a different window size in a frequency selective channel depending on the degree of ICI to which each subcarrier is subjected relative to the power of the signal part such that a better trade-off between BER performance and complexity is achieved. In [ALS14], we choose the window size depending on the signal to interference ratio (SIR) at subcarrier position k, $\Upsilon_D(k)$, which we define as the ratio of the squared magnitude of the main diagonal element $|H(k,\,k)|^2$ of the channel matrix at subcarrier position k to an interference function $I_D(k)$

$$\Upsilon_D(k) = \frac{|H(k,\,k)|^2}{|I_D(k)|^2}, \tag{3.36}$$

We define the interference function $I_D(k)$ as the average interference magnitude obtained from the two interferes that are D subcarriers apart from the current subcarrier position k in both directions $(k \pm D)$

$$I_D(k) = 0.5\left(|H(k,\,k+D)| + |H(k,\,k-D)|\right). \tag{3.37}$$

The interference function is specifically defined as in (3.37) such that the SIR function is monotonically increasing with the number of subcarriers considered D, i.e., the signal to interference ratio function should increase as D increases. Using (3.23), the SIR function can be written as

$$\begin{aligned}\Upsilon_D(k) &= \left(\frac{|H(k,\,k)|}{0.5\frac{\kappa}{D}|\left(v(k+D)+v(k-D)\right)|}\right)^2 \\ &\approx \left(\frac{4\pi D|H(k,\,k)|}{|v(k)|}\right)^2,\end{aligned} \tag{3.38}$$

where in the last step, we assumed $v(k-D) \approx v(k) \approx v(k+D)$, which is equivalent to assuming a flat fading channel response at subcarrier positions $k-D$ to $k+D$. This assumption is justified for $D(k) << N$. Given a certain SIR threshold, Υ_{th}, the optimum D has to satisfy

$$\frac{4\pi D(k)\,|H(k,\,k)|}{|v(k)|} > \sqrt{\Upsilon_{th}} \tag{3.39}$$

The required $D(k)$ can then be determined as

$$D(k) = round\left(\frac{|v(k)|\sqrt{\Upsilon_{th}}}{4\pi|H(k,\,k)|}\right). \tag{3.40}$$

Using (3.40), the MMSE-ASW algorithm chooses the window size parameter $D(k)$ adaptively for each subcarrier k.

Step	Complexity (number of complex multiplications)
Matrix Multiplication $\bar{\mathbf{H}}(k)\bar{\mathbf{H}}^H(k)$	$(2D+1)^3$
Matrix Inversion $\left(\bar{\mathbf{H}}(k)\bar{\mathbf{H}}^H(k)+\bar{\mathbf{C}}_{\text{Noise},(2\text{D}+1\times 2\text{D}+1)}\right)^{-1}$	$\frac{2(2D+1)^3+3(2D+1)^2-5(2D+1)}{6}$
Matrix Multiplication $\left(\bar{\mathbf{H}}(k)\bar{\mathbf{H}}^H(k)+\bar{\mathbf{C}}_{\text{Noise},(2\text{D}+1\times 2\text{D}+1)}\right)^{-1}\cdot \mathbf{H}_{main,(2D+1\times 1)}(k)$	$(2D+1)^2$
Filtering and Normalization $\frac{1}{\tilde{\mathbf{W}}^H_{f,(2D+1\times 1)}(k)\mathbf{H}_{main,(2D+1\times 1)}(k)}\tilde{\mathbf{W}}^H_{f,(2D+1\times 1)}(k)\bar{\mathbf{R}}(k)$	$2(2D+1)+3$

Table 3.1.: Complexity of MMSE equalizer per subcarrier

3.2.1.2. Complexity Analysis

In this section, we assess the complexity vs BER performance of the MMSE-ASW ICIC . In Table 3.1, we compute the number of complex multiplications required by an MMSE ICIC which considers D subcarriers, assuming Gauss elimination is used for matrix inversion. We follow the steps in (3.33) to (3.35).

We assume the division operation such as the one in (3.40) to be more complex than a multiplication operation. We make a reasonable assumption that one division operation is three times more complex than one multiplication operation, such that the cost of computing $D(k)$ is taken into consideration. $D(k)$ can be determined through one division operation $\frac{|v(k)|}{|H(k,k)|}$, where $D(k)$ can then be determined using a lookup table in a second step. Therefore, an extra factor of 3 is added to the complexity of the MMSE-ASW algorithm. In the case when $D(k)=0$ is chosen by the MMSE-ASW ICIC, a simple ZF is applied with a complexity of one division operation, i.e., three multiplications.

3.2.1.3. Results on MMSE-ASW ICIC

In this section, we present simulation results for a DVB-T system for MMSE ICIC with fixed window size (FWS), MMSE-FWS ICIC (where the same D is chosen for all subcarriers) and for the proposed MMSE-ASW ICIC . The simulation settings are summarized in Table 3.2. We consider a Doppler frequency of 160 Hz, which corresponds to a velocity of 288 km/h assuming a carrier frequency of 600 MHz. The simulated channel is a TU6 channel. A maximum value of $D_{max}=2$ is set for the MMSE-ASW algorithm, which means the BER performance of the MMSE-ASW ICIC ($D_{max}=2$) can not be better than that of the conventional MMSE-FWS ICIC which uses $D=2$ for all subcarrier signals. On the other hand, because MMSE-ASW ICIC is allowed to use $D=2$ on some subcarriers, the BER performance can be better than that of

Parameter	Setting
System	DVB-T
BER	after Viterbi decoding in dependency of Doppler/SNR
CSI	PACE using linear interpolation
noise estimation	PANE after MMSE
Doppler shift	160 Hz
SNR	30 dB, noise free
Modulation	4 QAM , 16 QAM
Coding	Viterbi channel decoding with code rate(2/3) traceback depth=252
OFDM	8k FFT , $N_{GI} = 2048$ samples, $N_a = 6817$ subcarriers $N_{data} = 6048$ subcarriers
Channel	TU6 channel
ICIC	MMSE-FWS:$D = 0, 1, 2.$ MMSE- ASW:$D_{max} = 2$ PIC:$D = 1, 2, 3$

Table 3.2.: Simulation parameters used to produce results in Figures 3.6 and 3.10

a conventional MMSE-FWS ICIC which uses $D = 1$ over all subcarriers. PACE is conducted to obtain the main diagonal channel coefficients, using frequency only linear interpolation.

In Figure 3.6, the histograms of the selected values of $D(k)$ based on (3.40) for different values of Υ_{th} are displayed in a noise-free environment and at SNR = 30 dB, respectively. We notice that as Υ_{th} increases, a higher D is chosen more frequently by the algorithm.

To be able to analyze both the BER performance and the complexity of the proposed algorithm compared to that of the classical MMSE ICIC approach, we consider Figure 3.7. Every point in the plot carries information about the BER and complexity of MMSE-FWS or MMSE-ASW algorithms. The x-axis is the consumed complexity (number of multiplications) whereas the y-axis depicts the BER. At a Doppler frequency of 160 Hz and a noise free environment in Figure 3.7a, we observe that the MMSE-ASW ICIC with $\Upsilon_{th} = 4.5$ dB has both better BER performance and less complexity compared to those of the conventional MMSE-FWS ICIC ($D = 1$). Using a threshold of $\Upsilon_{th} = 4.5$ dB, only an average number of 13 multiplications are required as opposed to 51 multiplications needed with the conventional approach using fixed ($D = 1$) for all subcarriers. Therefore, about 74% reduction in complexity can be achieved at a Doppler frequency of 160 Hz using MMSE-ASW ICIC with $\Upsilon_{th} = 4.5$ dB. In a noisy environment, at $\Gamma = 30$ dB, MMSE-ASW ICIC with $\Upsilon_{th} = 4.5$ dB proves to be again of a better performance and less complexity compared to the conventional MMSE-FWS ICIC($D = 1$) as shown in Figure 3.7b, where it achieves almost the same complexity gain.

At a lower SNR, $\Gamma = 20$ dB, the quasi-error free BER occurs at a lower Doppler shift of $f_{D,max} = 140$ Hz, as shown in Figure 3.8. As the SNR decreases, a higher threshold is needed to deliver the same performance as that of MMSE-FWS ICIC with $D = 1$,

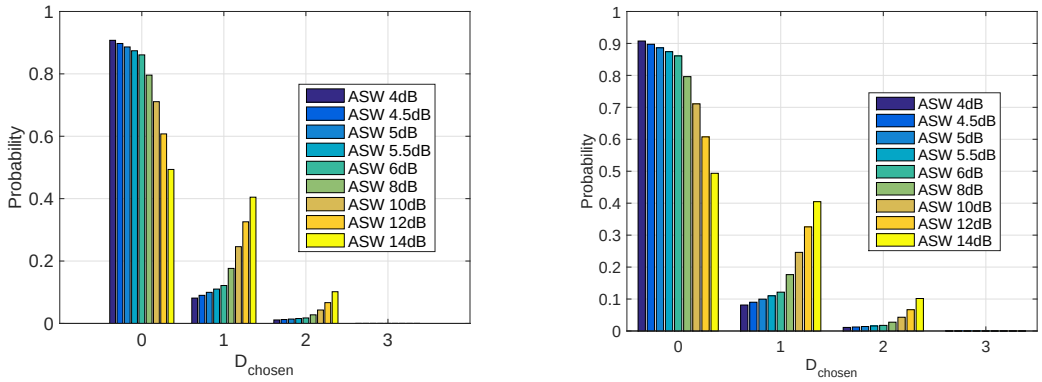

(a) noise free environment

(b) $\Gamma = 30\,\mathrm{dB}$

Figure 3.6.: Histograms of selected values of $D\,(k)$ based on (3.40) for different values of Υ_{th}, $f_{D,max} = 160\,\mathrm{Hz}$ using 4QAM modulation. Rest of simulation settings summarized in Table 3.2

namely a threshold of $\Upsilon_{th} = 5\,\mathrm{dB}$, as shown in Figure 3.8a.

In a hardware implementation of MMSE-ASW ICIC, it might be required to fix the complexity of the equalization step, i.e., assign fixed percentages of the subcarriers to a bank of MMSE equalizers with different window sizes. This restriction should reduce the degree of freedom of the MMSE-ASW ICIC equalizer on choosing the appropriate window size freely based on Υ_{th}. Therefore, we expect lower gains with a fixed complexity MMSE-ASW ICIC compared to those observed in Figures 3.7 and 3.8a.

3.2.2. Parallel Interference Canceler

A well known class of ICI cancelers is that of a PIC [ZZB05, MTV07a]. Figure 3.9 depicts the architecture of such a scheme.

The first stage of the ICIC is a ZF stage, which outputs initial estimates of all sent symbols $\hat{S}^{ZF}\,(k)$. The second stage involves using the estimated symbols $\hat{S}^{ZF}\,(k)$ and the off-diagonal estimates $H(k, k+d)$ to eliminate the ICI on every received subcarrier $R(k)$ as follows

$$\hat{R}(k) = R(k) - \sum_{d=-D, d\neq 0}^{D} H(k, k+d)\hat{S}^{ZF}(k+d). \tag{3.41}$$

The final output is obtained in the final stage by applying ZF on the ICI canceled received symbol estimates $\hat{R}(k)$ as:

$$\hat{S}(k) = \frac{\hat{R}k)}{H(k,k)} \tag{3.42}$$

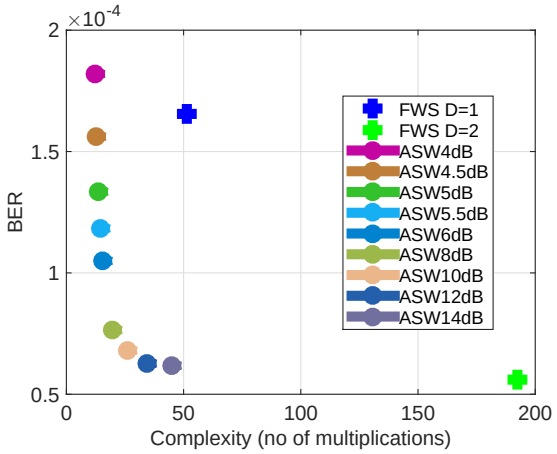

(a) noise free environment

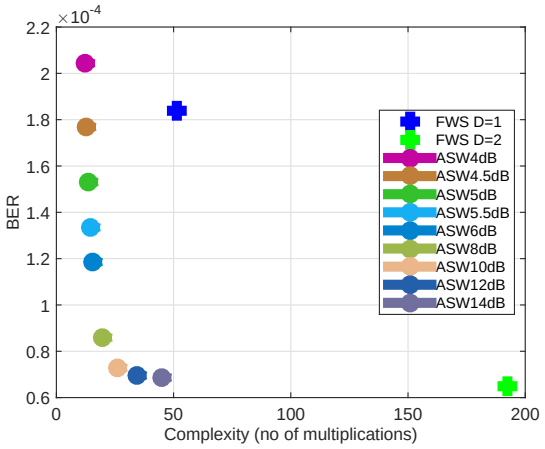

(b) $\Gamma = 30\,\mathrm{dB}$

Figure 3.7.: BER vs complexity plot $f_{D,max} = 160\,\mathrm{Hz}$ using 4QAM modulation. Rest of simulation settings summarized in Table 3.2

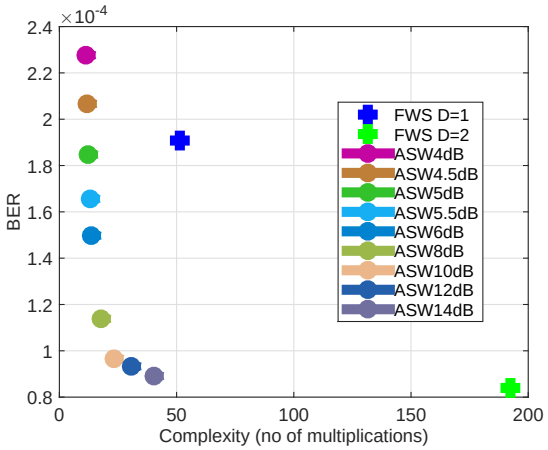

(a) BER vs complexity plot

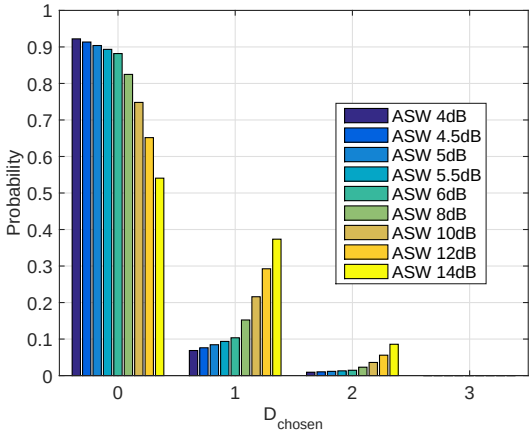

(b) Histogram of selected values of $D(k)$ based on (3.40) for different values of Υ_{th}

Figure 3.8.: BER vs complexity plot $f_{D,max} = 140\,\text{Hz}$ and $\Gamma = 20\,\text{dB}$ using 4QAM modulation. Rest of simulation settings summarized in Table 3.2

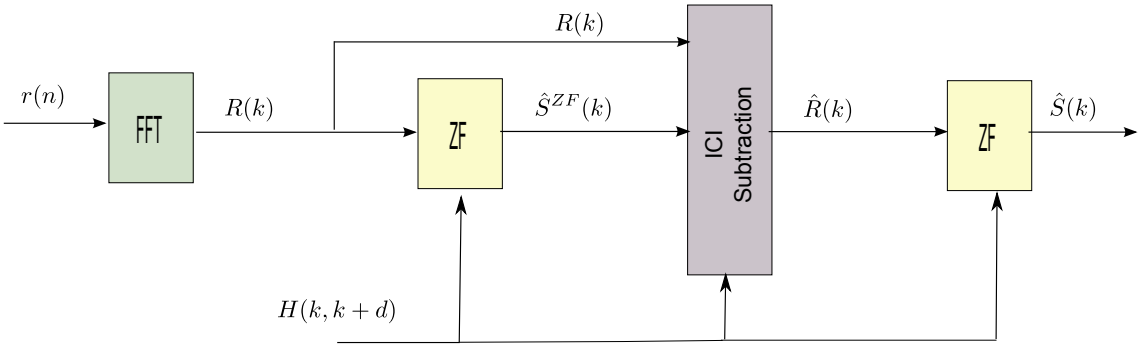

Figure 3.9.: architecture of PIC

In section 4.7.1.1, we shall elaborate again on this equalizer in the context of ICI cancellation in a multi-antenna receiver system.

3.2.3. Summary of Results of SISO ICI Equalizers

In Figure 3.10, we can see the BER performance vs Doppler shift and SNR using different equalizers. The simulation settings can be found in Table 3.2. As shown, ICI appears as an error floor especially through the performance of the ZF equalizer, which totally neglects the ICI, as shown in Figure 3.10a. In the rest of this thesis, we mainly rely on simulation results in dependency of the Doppler shift as the one shown in Figure 3.10b, where the improvement of one equalizer over the other is clear through the Doppler gain (achieving the same BER at a higher Doppler shift).

As shown, the best performance is achieved using MMSE-FWS ICIC with $D = 2$, at the expense of the highest complexity (192 multiplications per subcarrier operation according to Table 3.1). MMSE-FWS ICIC with $D = 2$ can achieve more than 20 Hz gain, around the quasi-error free BER, compared to a simple ZF equalizer which totally ignores ICI. Considering the same number of off-diagonals, $D = 2$, the PIC shows a worse BER performance than the corresponding MMSE with a gain of ~ 7 Hz at a much lower complexity. Increasing the number of the considered off-diagonals in a PIC beyond $D = 3$ does not yield a much better gain, which can be inferred from the marginal gain obtained by increasing D from $D = 2$ to $D = 3$ as shown in Figure 3.10b. Therefore, in the rest of this thesis, we shall consider a PIC with $D = 3$ and a MMSE-FWS ICIC with $D = 1$, bearing in mind that the latter is of higher computational complexity.

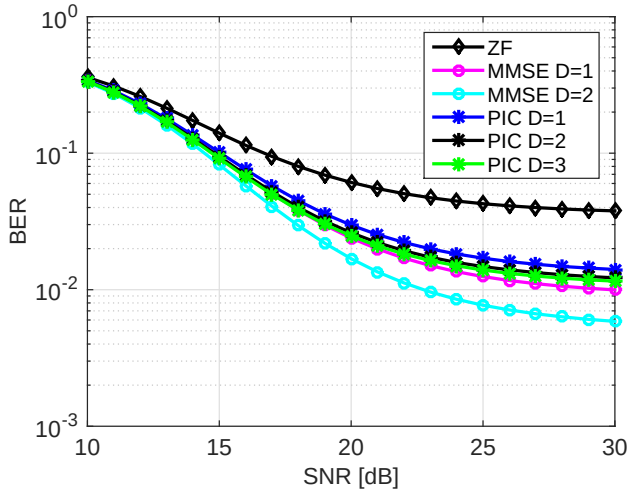

(a) $f_{D,max} = 150\,\text{Hz}$

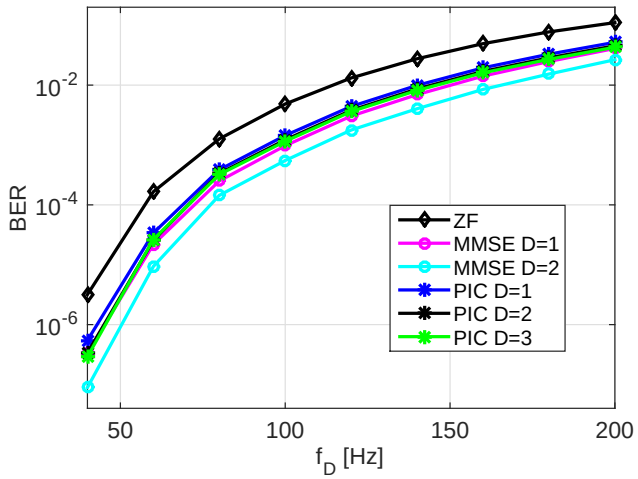

(b) $\Gamma = 30\,\text{dB}$

Figure 3.10.: BER comparison of several SISO equalizers. Using 16QAM modulation. Rest of simulation settings summarized in Table 3.2

4. Algorithms for Mobile SIMO Reception of Multi-Carrier Signals

In this Chapter, we investigate employing multiple antennas at the receiver side to achieve a better ICI mitigation in a time-varying channel. First, we start with a static multi-antenna receiver environment, where the received signal vector across the M different receive antennas can be written as

$$\check{\mathbf{R}}(k) = \check{\mathbf{H}}(k,\, k)\, S(k) + \check{\mathbf{X}}(k)\,, \tag{4.1}$$

where the $M \times 1$ received signal vector $\check{\mathbf{R}}(k)$, channel vector $\check{\mathbf{H}}(k,\, k)$ and noise vector $\check{\mathbf{X}}(k)$ can be written as

$$\check{\mathbf{R}}(k) = \begin{bmatrix} R_1(k) \\ \vdots \\ R_M(k) \end{bmatrix} \tag{4.2}$$

$$\check{\mathbf{H}}(k,\, k) = \begin{bmatrix} H_1(k,\, k) \\ \vdots \\ H_M(k,\, k) \end{bmatrix}, \tag{4.3}$$

and

$$\check{\mathbf{X}}(k) = \begin{bmatrix} X_1(k) \\ \vdots \\ X_M(k) \end{bmatrix}, \tag{4.4}$$

where $X_m(k)$ is the AWGN sample from antenna m at subcarrier position k with noise variance σ^2, as defined in (3.4), i.e., in this work, we consider the SNR per receive antenna instead of the total SNR at the receiver side. In general, the output signal of a linear SIMO combiner can be written as

$$\tilde{S}(k) = \tilde{\mathbf{W}}^H(k)\, \check{\mathbf{R}}(k)\,, \tag{4.5}$$

where the $M \times 1$ weighting vector $\tilde{\mathbf{W}}(k)$ can be written as

$$\tilde{\mathbf{W}}(k) = \begin{bmatrix} \tilde{W}_1(k) \\ \vdots \\ \tilde{W}_M(k) \end{bmatrix}. \tag{4.6}$$

Throughout this Chapter, We focus on the different methods used to set the weighting vector $\tilde{\mathbf{W}}(k)$.

4.1. Maximum Ratio Combining

In an environment where all antennas suffer from the same noise level and have spatially uncorrelated channel paths [1], the weighting vector of the MRC $\tilde{\mathbf{W}}_{mrc}(k)$ can be written as

$$\tilde{\mathbf{W}}_{mrc}(k) = \check{\mathbf{H}}(k,\, k) = \begin{bmatrix} H_1(k,\, k) \\ \vdots \\ H_M(k,\, k) \end{bmatrix}, \tag{4.7}$$

and thus the estimated signal can be set as

$$\tilde{S}(k) = \tilde{\mathbf{W}}_{mrc}^{H}(k)\, \check{\mathbf{R}}(k) = \sum_{m=1}^{M} H_m^*(k,\, k) R_m(k)\,. \tag{4.8}$$

Using (4.8), we can see how the antenna paths with higher channel power have more weight into the combined signal, which is intuitively satisfying since those antenna paths are more reliable. The conjugate operator applied on the channel coefficient $H_m^*(k,\, k)$ can be seen as a way to coherently combine the received signals, i.e., avoid the case where destructive interference can occur in the summand.

The final estimated signal still has to be normalized as follows

$$\hat{S}(k) = \frac{\tilde{S}(k)}{\tilde{\mathbf{W}}_{mrc}^{H}(k)\, \check{\mathbf{H}}(k,\, k)} \tag{4.9}$$

Alternatively, the weighting vector can be normalized as

$$\hat{\mathbf{W}}_{mrc}(k) = \frac{\tilde{\mathbf{W}}_{mrc}(k)}{\tilde{\mathbf{W}}_{mrc}^{H}(k)\, \check{\mathbf{H}}(k,\, k)}, \tag{4.10}$$

where the final estimated signal is then written as

$$\hat{S}(k) = \hat{\mathbf{W}}_{mrc}^{H}(k)\, \check{\mathbf{R}}(k)\,. \tag{4.11}$$

In general, any normalized linear SIMO combiner can be written as

$$\hat{\mathbf{W}}(k) = \frac{\tilde{\mathbf{W}}(k)}{\epsilon(k)}, \tag{4.12}$$

where the normalization factor $\epsilon(k)$ can be written as

$$\epsilon(k) = \tilde{\mathbf{W}}^{H}(k)\, \check{\mathbf{H}}(k,\, k)\,, \tag{4.13}$$

[1] In this work, we assume that the receiver antennas are spatially uncorrelated.

which we are going to use in all subsequent combiners.

In [HO02], the weighting vector of the MRC was derived in the case of asymmetric noise levels across the different antennas as

$$\tilde{\mathbf{W}}_{MRC}(k) = \check{\mathbf{C}}_{\text{Noise}}^{-1}\check{\mathbf{H}}(k,\, k) = \begin{bmatrix} \sigma_1^2 & & \\ & \ddots & \\ & & \sigma_M^2 \end{bmatrix}^{-1} \begin{bmatrix} H_1(k,\, k) \\ \vdots \\ H_M(k,\, k) \end{bmatrix}, \tag{4.14}$$

where $\check{\mathbf{C}}_{\text{Noise}}$ is the $(M \times M)$ autocorrelation matrix of the input AWGN noise vector across the M antennas and can be written as

$$\check{\mathbf{C}}_{\text{Noise}} = E\left\{\check{\mathbf{X}}(k)\,\check{\mathbf{X}}^H(k)\right\}. \tag{4.15}$$

Consequently, the combined signal with MRC is set as

$$\tilde{S}(k) = \sum_{m=1}^{M} \frac{H_m^*(k,\, k)}{\sigma_m^2} R_m(k). \tag{4.16}$$

Compared to (4.8), we can now see how the reliability of the information delivered across the different antennas $R_m(k)$ is weighted with the channel to noise power ratio rather than the channel power only.

In Figure 4.1, we show the gain of using antenna receiver diversity to mitigate ICI, using 2 antenna MRC and SISO ZF receivers. For a fair comparison, we fix the total SNR at the receiver side (sum of SNR of both receive antennas, $10^{0.1\Gamma} = 10^{0.1\Gamma_1} + 10^{0.1\Gamma_2}$) in the SIMO case to the SNR of the one receive antenna in the SISO case. The average noise level in both channels is also assumed to be identical. In the rest of this work, we show results for $M = 2$ antenna receivers. As shown in Figure 4.1a, as the Doppler frequency increases, the Doppler frequency gain (i.e., Doppler frequency achieved at a given BER) of MRC compared to SISO ZF increases. The simulation settings are summarized in Table 4.6. Similarly, a much lower error floor is encountered with MRC compared to SISO ZF.

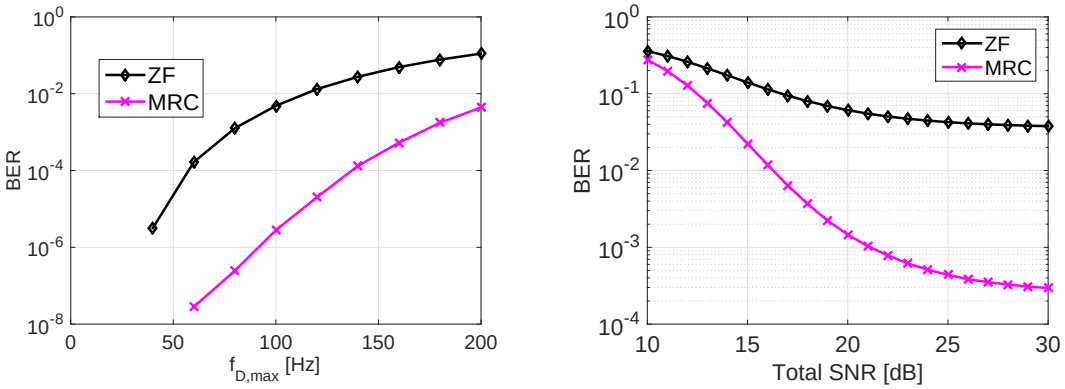

(a) BER vs Doppler frequency range at total SNR = 30 dB

(b) BER vs total SNR range at $f_{D,max} = 150$ Hz

Figure 4.1.: Gain from receive antenna diversity combining using $M = 2$ receive antennas. Simulation settings are summarized in Table 4.1.

Parameter	Setting
System	DVB-T
BER	after Viterbi decoding in dependency of Doppler shift and total SNR
CSI	PACE using linear interpolation
noise estimation fed to demapper	after MRC using (4.41)
SNR	30 dB
Modulation	64QAM
Coding	Viterbi decoding(2/3) traceback depth=252
OFDM	8k FFT , 2k samples GI
	$\Delta f = 1.116$ kHz, $N_a = 6817$ subcarriers, $N_{data} = 6048$ subcarriers
Channel	2×1 spatially uncorrelated TU6 channels
OFDM receiver	MRC

Table 4.1.: Simulation Parameters used in Figure 4.1

4.2. Optimum Combining

In a time-varying environment, (4.1) can be rewritten as

$$\check{\mathbf{R}}(k) = \check{\mathbf{H}}(k,\, k)\, S(k) + \sum_{d=-D_{simo},\, d\neq 0}^{D_{simo}} \check{\mathbf{H}}(k,\, k+d)\, S(k+d) + \check{\mathbf{X}}(k), \tag{4.17}$$

In [STJ08, Ser12], an expression for an ICI-aware linear SIMO combiner was independently derived. The expression is based in both cases on a combiner which takes into consideration knowledge of the ICI to maximize the SINR instead of maximizing the SNR, as in MRC. In [STJ08], the linear combiner is derived based on the concept of optimum combining in [Win84], derived initially for a co-channel interference problem. In [Ser12], the expression for the weighting coefficients is derived as a special MMSE combiner, referred to in the publication as $\mathbf{g}^{SINR}$. In [Ser12], a simplified combiner is further derived, referred to in the publication as $\mathbf{g}^{SDCC}$.

In this thesis, we refer to the original combiner in [STJ08] as optimum combining (OC), with a weighting filtering vector $\tilde{\mathbf{W}}_{OC}(k)$, and to the simplified version of [Ser12] as simplified Doppler compensation combining (SDCC), with a weighting filtering vector $\tilde{\mathbf{W}}_{SDCC}(k)$. First, we start with the derivation of the OC combiner. The combining vector takes ICI into consideration in the following optimization problem

$$\tilde{\mathbf{W}}_{OC}(k) = arg \min_{\tilde{\mathbf{W}}(k)} E\{|\tilde{\mathbf{W}}^H(k)\, \check{\mathbf{R}}(k) - S(k)|^2\}. \tag{4.18}$$

Solving (4.18) with the MMSE criteria leads to the following detector:

$$\begin{aligned}\tilde{\mathbf{W}}_{OC}(k) &= \left(\sum_{d=-D_{simo},\, d\neq 0}^{D_{simo}} \check{\mathbf{H}}(k,\, k+d)\, \check{\mathbf{H}}^H(k,\, k+d) + \check{\mathbf{H}}(k,\, k)\, \check{\mathbf{H}}^H(k,\, k) + \check{\mathbf{C}}_{\text{Noise}}\right)^{-1} \times \\ &\quad \check{\mathbf{H}}(k,\, k),\end{aligned} \tag{4.19}$$

where D_{simo} is the number of frequency off-diagonal coefficients considered in a SIMO combiner to differentiate it from D the number of frequency off-diagonal coefficients considered in the SISO equalizers. Further approximation on (4.19) leads to (see (6.42) in [Ver98]):

$$\begin{aligned}\tilde{\mathbf{W}}_{OC}(k) &= \left(\sum_{d=-D_{simo},\, d\neq 0}^{D_{simo}} \check{\mathbf{H}}(k,\, k+d)\, \check{\mathbf{H}}^H(k,\, k+d) + \check{\mathbf{C}}_{\text{Noise}}\right)^{-1} \check{\mathbf{H}}(k,\, k) \\ &= \mathbf{Z}^{-1}(k)\, \check{\mathbf{H}}(k,\, k),\end{aligned} \tag{4.20}$$

where, in general, the interference plus noise matrix $\mathbf{Z}(k)$ can be written as the summation of the ICI covariance matrix $\check{\mathbf{C}}_{\text{ICI}}(k)$ and the noise covariance matrix $\check{\mathbf{C}}_{\text{Noise}}$ defined in (4.15)

$$\mathbf{Z}(k) = \check{\mathbf{C}}_{\mathrm{ICI}}(k) + \check{\mathbf{C}}_{\mathrm{Noise}}, \tag{4.21}$$

with $\check{\mathbf{C}}_{\mathrm{Noise}}$ set ideally as $\begin{bmatrix} \sigma_1^2 & & \\ & \ddots & \\ & & \sigma_M^2 \end{bmatrix}$ in an AWGN environment. For more information about how $\check{\mathbf{C}}_{\mathrm{Noise}}$ is built in our system, the interested reader can refer to section 4.5.2. The ICI covariance matrix $\check{\mathbf{C}}_{\mathrm{ICI}}(k)$ is built as

$$\check{\mathbf{C}}_{\mathrm{ICI}}(k) = \sum_{d=-D_{simo},d\neq 0}^{D_{simo}} \check{\mathbf{H}}(k,\, k+d)\, \check{\mathbf{H}}^H(k,\, k+d), \tag{4.22}$$

where the off-diagonal channel vector $\check{\mathbf{H}}(k,\, k+d)$ can be written as

$$\check{\mathbf{H}}(k,\, k+d) = \begin{bmatrix} H_1(k,\, k+d) \\ \vdots \\ H_M(k,\, k+d) \end{bmatrix}, \tag{4.23}$$

where $H_m(k,\, k+d)$ is the interference of subcarrier $k+d$ on subcarrier k, received by antenna m.

4.3. Simplified Doppler Compensation Combining

In [Ser12], a simplified diversity combiner which takes ICI into consideration is proposed. Computation of the matrix $\check{\mathbf{C}}_{\mathrm{ICI}}(k)$ according to (4.22), requires $2D_{simo}$ vector multiplications, each vector of dimension $M \times 1$. This operation requires $2M^2 D_{simo}$ complex multiplications and hence grows linearly with the number of off-diagonals considered D_{simo}. Assuming sufficient frequency correlation in the CFR, the off-diagonal coefficient $H(k,\, k+d)$ in (3.23) can be approximated as

$$\begin{aligned} H(k,\, k+d) &= \kappa \frac{v(k+d)}{d} \\ &\approx \kappa \frac{v(k)}{d} = \frac{H(k+1,\, k)}{d}. \end{aligned} \tag{4.24}$$

Hence, the spatially stacked off-diagonal channel vector $\check{\mathbf{H}}(k,\, k+d)$ can be approximated as

$$\check{\mathbf{H}}(k,\, k+d) \approx \frac{1}{d} \begin{bmatrix} H_1(k+1,\, k) \\ \vdots \\ H_M(k+1,\, k) \end{bmatrix}. \tag{4.25}$$

The ICI covariance matrix in (4.22) can be approximated as

$$\begin{aligned}\check{\mathbf{C}}_{\mathrm{ICI}}(k) &= \sum_{d=-D_{simo},d\neq 0}^{D_{simo}} \check{\mathbf{H}}(k,\,k+d)\,\check{\mathbf{H}}^{H}(k,\,k+d),\\ &\approx \left(\sum_{d=-D_{simo},\,d\neq 0}^{D_{simo}} \left(\frac{1}{d}\right)^{2}\right)\check{\mathbf{H}}(k+1,\,k)\,\check{\mathbf{H}}^{H}(k+1,\,k)\\ &= \kappa^{2}\left(\sum_{d=-D_{simo},\,d\neq 0}^{D_{simo}} \left(\frac{1}{d}\right)^{2}\right)\check{\mathbf{V}}(k)\,\check{\mathbf{V}}^{H}(k), \end{aligned} \tag{4.26}$$

where $\check{\mathbf{V}}(k)$ can be written as

$$\check{\mathbf{V}}(k) = \begin{bmatrix} v_1(k) \\ \vdots \\ v_M(k) \end{bmatrix}, \tag{4.27}$$

where $v_m(k)$ is as defined in (3.23). Therefore, the simplified OC weighting vector can be written as

$$\begin{aligned}\tilde{\mathbf{W}}_{SDCC}(k) &= \left(\kappa^{2}\left(\sum_{d=-D_{simo},\,d\neq 0}^{D_{simo}} \left(\frac{1}{d}\right)^{2}\right)\check{\mathbf{V}}_{(M\times 1)}(k)\,\check{\mathbf{V}}^{H}_{(M\times 1)}(k) + \check{\mathbf{C}}_{\mathrm{Noise}}\right)^{-1}\check{\mathbf{H}}(k,\,k)\\ &= \left(c_{SDCC}\check{\mathbf{V}}_{(M\times 1)}(k)\,\check{\mathbf{V}}^{H}_{(M\times 1)}(k) + \check{\mathbf{C}}_{\mathrm{Noise}}\right)^{-1}\check{\mathbf{H}}(k,\,k), \end{aligned} \tag{4.28}$$

with

$$c_{SDCC} = 2\kappa^{2}\sum_{d=1}^{D_{simo}}\left(\frac{1}{d}\right)^{2}. \tag{4.29}$$

$\tilde{\mathbf{W}}_{SDCC}(k)$ is the SDCC weighting vector. Comparing (4.19) with (4.28), we can see the great reduction in complexity. The complexity of computing (4.28) is almost independent of the selected value of D_{simo}, except for the complexity of computing c_{SDCC} which can be computed once offline. The approximation made in (4.26) is equivalent to assuming $v_m(k - D_{simo}) = \cdots = v_m(k + D_{simo})$, i.e., a certain coherence bandwidth is assumed in the frequency domain, which is the same assumption we made in the derivation of MMSE-ASW ICIC in (3.38). In Figures 4.2 and 4.3, we can see the performance loss encountered because of the approximation in (4.26) on a frequency selective 2TU6 channel, defined in section 2.3.3, using PACE and genie-aided channel knowledge (GACN). The simulation settings are summarized in Table 4.2.

The authors then go on to further simplify the expression in (4.28). Applying the matrix inversion lemma (MIL) on the inversion step $\left(c_{SDCC}\check{\mathbf{V}}_{(M\times 1)}(k)\,\check{\mathbf{V}}^{H}_{(M\times 1)}(k) + \check{\mathbf{C}}_{\mathrm{Noise}}\right)^{-1}$

Parameter	Setting
System	DVB-T
BER	after Viterbi decoding in dependency of Doppler shift
CSI	PACE using linear interpolation, GACN
SNR	30 dB
Modulation	64 QAM
Coding	Viterbi decoding (2/3) traceback depth=252
OFDM	8k FFT , 0.25GI , $N_a = 6817$ subcarriers $N_{data} = 6048$ subcarriers
Channel	2×1 spatially uncorrelated 2TU6 channels $(\tau_{delay} = 0.05GI, k_2 = -3\,\text{dB})$ $(\tau_{delay} = 0.15GI, k_2 = -3\,\text{dB})$
OFDM Receiver	OC, SDCC:$D_{simo} = 1, 10, 15.$

Table 4.2.: Simulation Parameters used to produce results in Figures 4.2 and 4.3

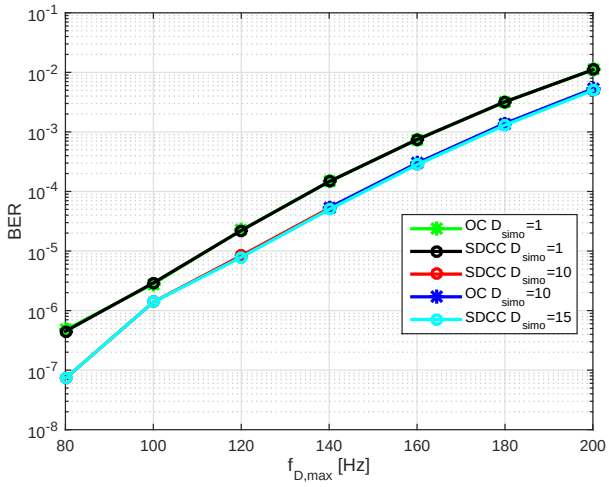

Figure 4.2.: Performance of OC vs SDCC for different values of D_{simo} in a 2TU6 channel with $(\tau_{delay} = 0.05GI, k_2 = -3\,\text{dB})$ and linear interpolation PACE. Simulation settings are summarized in Table 4.2.

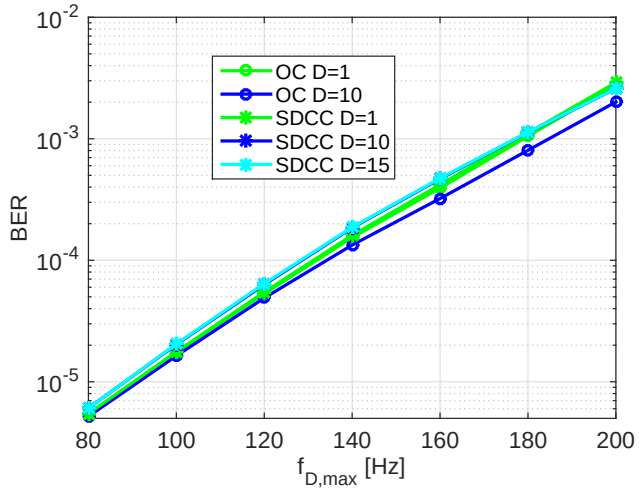

Figure 4.3.: Performance of OC vs SDCC for different values of D_{simo} in a 2TU6 channel with ($\tau_{delay} = 0.15GI, k_2 = -3\,\text{dB}$) and GACN. Simulation settings are summarized in Table 4.2.

yields

$$\begin{aligned}\tilde{\mathbf{W}}_{SDCC}(k) &= \left(c_{SDCC}\check{\mathbf{V}}(k)\check{\mathbf{V}}^H(k) + \check{\mathbf{C}}_{\text{Noise}}\right)^{-1}\check{\mathbf{H}}(k,\,k) \\ &\approx \frac{1}{\sigma^2}(\mathbf{I} - \frac{c_{SDCC}\check{\mathbf{V}}(k)\check{\mathbf{V}}^H(k)}{\sigma^2 + c_{SDCC}||\check{\mathbf{V}}(k)||^2})\check{\mathbf{H}}(k,\,k) \\ &\approx \check{\mathbf{H}}(k,\,k) - \frac{c_{SDCC}\check{\mathbf{V}}^H(k)\check{\mathbf{H}}(k,\,k)}{\sigma^2 + c_{SDCC}||\check{\mathbf{V}}(k)||^2}\check{\mathbf{V}}(k) \end{aligned} \tag{4.30}$$

where in the second step $\mathbf{C}_{\text{Noise}}$ is approximated as $\mathbf{C}_{\text{Noise}} \approx \sigma^2\mathbf{I}_M$. In the third step, the constant term $\frac{1}{\sigma^2}$ is eliminated because in any case $\tilde{\mathbf{W}}_{SDCC}(k)$ is going to be further normalized as in the OC (see (4.12)).

Comparing (4.30) with (4.28), we see how the complexity is reduced from $O(M^3)$ to $O(M)$ when the direct matrix inversion is avoided. However, a pitfall of (4.30) is that the last approximation in (4.30) assumes that all antennas have the same noise statistics, which is rarely the case in practice. Therefore, the reduction in complexity is expected to come at the cost of an inferior BER performance in practice when all antennas suffer from different noise levels. In this work, we use the non-approximated version of SDCC in (4.28).

The authors in [Ser12] then go on to present an even more simplified version which assumes a noise free reception, namely approximated zero forcing (aZF).

$$\tilde{\mathbf{W}}_{aZF}(k) = (\mathbf{I} - \frac{\check{\mathbf{V}}(k)\check{\mathbf{V}}^H(k)}{||\check{\mathbf{V}}(k)||^2})\check{\mathbf{H}}(k,\,k)\,. \tag{4.31}$$

4.4. Enhanced MRC with Colored Noise Information

In a mobile channel, the induced ICI presents itself as a source of Gaussian noise as mentioned earlier in this Chapter. Therefore, even in cases where both antennas have the same AWGN level, both antennas will encounter different level of total noise+ICI in a frequency selective mobile channel. In [HHDCC00], the authors proposed a modified MRC scheme for a time varying channel, where the SINR per antenna is computed, ϱ_m and used to modify the corresponding MRC weights. SINR per antenna can be written as $\varrho_m = \frac{E_S}{\sigma^2_{t,m}}$, where $\sigma^2_{t,m}$ is the total noise variance $\sigma^2 + \sigma^2_{ICI}$ on antenna m, which can be computed through PANE as explained in section 2.5. Therefore, (4.14) can be rewritten as

$$\tilde{\mathbf{W}}_{MRC}(k) = \check{\mathbf{C}}^{-1}\check{\mathbf{H}}(k,\, k) = \begin{bmatrix} \sigma^2_{t,1} & & \\ & \ddots & \\ & & \sigma^2_{t,M} \end{bmatrix}^{-1} \begin{bmatrix} H_1(k,\, k) \\ \vdots \\ H_M(k,\, k) \end{bmatrix}, \tag{4.32}$$

where $\check{\mathbf{C}}$ is the total noise+ICI covariance matrix.

In [AES15], we proposed an enhanced MRC scheme which considers the SINR per antenna and frequency bin, i.e., $\varrho_m(k)$. As we shall show in this section, significant gain can be achieved from considering the frequency variation of the noise covariance matrix, i.e., $\check{\mathbf{C}}(k)$ instead of $\check{\mathbf{C}}$.

Equations (4.32) and (4.16) can then be rewritten as

$$\tilde{\mathbf{W}}_{eMRC}(k) = \check{\mathbf{C}}^{-1}(k)\,\check{\mathbf{H}}(k,\, k) = \begin{bmatrix} \sigma^2_{t,1}(k) & & \\ & \ddots & \\ & & \sigma^2_{t,M}(k) \end{bmatrix}^{-1} \begin{bmatrix} H_1(k,\, k) \\ \vdots \\ H_M(k,\, k) \end{bmatrix} \tag{4.33}$$

and

$$\tilde{S}(k) = \sum_{m=1}^{M} \frac{H^*_m(k,\, k)}{\sigma^2_{t,m}(k)} R_m(k)\,. \tag{4.34}$$

Windowed Noise Estimation for DVB-T/T2 In [YA05], the problem of noise estimation in the presence of strong interference is considered. The authors assume a fully known OFDM symbol at the receiver side and propose to estimate the noise via a 2D moving average window in time and frequency.

Because of the lack of the temporal correlation between the channel impulse response samples in fast fading channels and the use of long OFDM symbols, we rely on the continual pilots to capture the total noise frequency selectivity in the frequency domain only. In Figure 4.4, we can see the noise power per continual pilot computed according to (2.26) for an 8k FFT DVB-T signal. The number of continual pilots, 132, is significantly

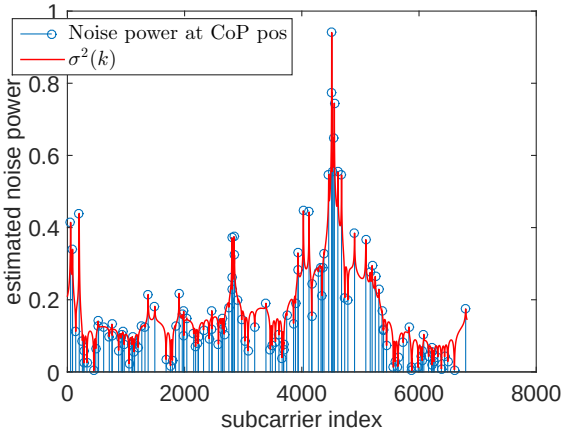

Figure 4.4.: Noise power captured by CoPs in a SISO TU6 channel, $\Gamma = 30\,\mathrm{dB}$ and $f_{D,norm} = 0.13$

smaller than the total number of active subcarriers, 6817. However, as we can see the total noise frequency selectivity can be captured well, using only the continual pilots.

In [AES15], we proposed to obtain a localized estimate of the noise power per subcarrier on each antenna, by considering only a window of the continual pilots around every subcarrier instead of one global average noise variance value per OFDM symbol, and to feed these values to the MRC to optimize its weights accordingly. Using a rectangular window of q continual pilots centered around the k^{th} subcarrier, the average input noise power at subcarrier position k can be computed as

$$\hat{\sigma_t^2}(k) = \frac{1}{q} \sum_{\iota \in \Omega_{CoP}^k(\iota)} \sigma^2(\iota), \tag{4.35}$$

where $\sigma^2(\iota)$ is computed as in (2.26) and Ω_{CoP}^k contains the indices of q continual pilots centered around the k^{th} subcarrier.

In Figure 4.5, we can see the MSE (normalized with respect to the maximum MSE) for different Doppler frequency shifts and channel lengths. We can see that, on the one hand, in a flat fading channel or in a static channel, where the total noise power is white, a larger window size gives a better performance. On the other hand, the higher the Doppler frequency shift in the frequency selective channel, the smaller the optimum window size should be. Thus, the optimum window size depends on the ratio of the colored noise to the total noise. The contribution of the colored noise increases as the Doppler shift increases or the frequency selectivity increases. Therefore, the optimum window size depends on the channel frequency selectivity, SNR and Doppler shift.

In [YA07], an MMSE filtering technique is proposed to deal with noise estimation in the presence of colored noise. The filtering coefficients are derived as a function of the noise covariance matrix and the AWGN noise power. In reality, such statistics need to be estimated which puts an overhead at the receiver side. In [AES15], we proposed to

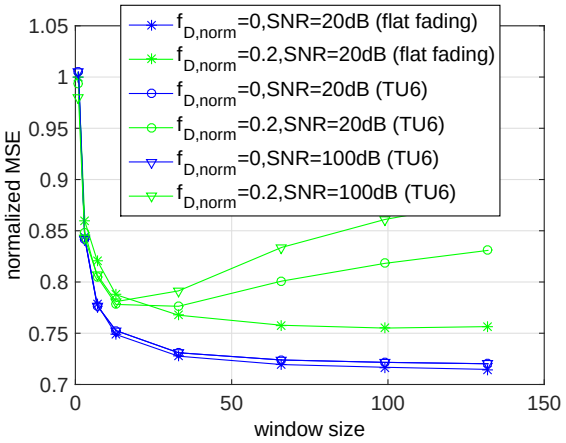

Figure 4.5.: Normalized MSE in a SISO receiver with respect to the maximum MSE, for $f_{D,norm} = 0$ and 0.2, 16QAM modulation and 8k FFT.

decrease the dependency of the performance of (4.35) on the window size by applying a simple weighting criterion depending on the distance of the considered CoP from the current subcarrier position. We therefore modify (4.35) as

$$\hat{\sigma_t^2}(k) = \frac{1}{\sum_{\iota \in \Omega_{CoP}^k(\iota)} A(k,\iota)} \sum_{\iota \in \Omega_{CoP}^k(\iota)} A(k,\iota)\, \sigma^2(\iota), \tag{4.36}$$

where we choose the weighting function $A(k,\iota)$ as

$$A(k,\iota) = \frac{1}{|k-\iota|}. \tag{4.37}$$

In Figure 4.6, we can see the actual input noise power (shown in blue). Using a window size of $q = 13$ CoPs (shown in red), the noise power can be tracked in a better way than by just setting it to the average noise power value as in (2.25) $\bar{\sigma^2} = \frac{1}{N_{CoP}} \sum_{\iota \in \Omega_{CoP}} \sigma^2(\iota)$ (shown in black), where N_{CoP} is the number of CoPs per OFDM symbol. We can also see that even a better tracking capability can be achieved using a window size of $q = 100$ samples combined with the proposed weighting criterion in (4.36) (shown in green).

In Figure 4.7, we compare the performance of MRC with different noise information according to (4.7),(4.32) and (4.33). The simulation settings are summarized in Table 4.3. As we can see, significant gain ($\sim 10\,\mathrm{Hz}$) can be achieved by considering the frequency variation of the ICI component using (4.33). In section 4.7.3, we show further results for different noise window sizes.

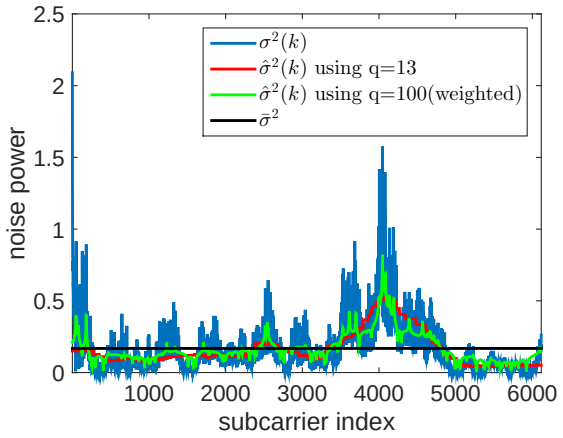

Figure 4.6.: Estimated Noise power captured in a SISO receiver by continual pilots in a TU6 channel $\Gamma = 30\,\mathrm{dB}$, 64QAM and $f_{D,norm} = 0.13$

Parameter	Setting
System	DVB-T
BER	after Viterbi decoding in dependency of Doppler shift
CSI	PACE using linear interpolation, GACN
SNR	30 dB
Modulation	64QAM
Coding	Viterbi decoding (2/3) traceback depth=252
OFDM	8k FFT , $N_{GI} = 2048$ samples, $N_a = 6817$ subcarriers, $N_{data} = 6048$ subcarriers
Channel	2×1 spatially uncorrelated TU6 channels
OFDM Receiver	MRC: (4.7),(4.32) and (4.33)

Table 4.3.: Simulation Parameters used to produce results in Figure 4.7

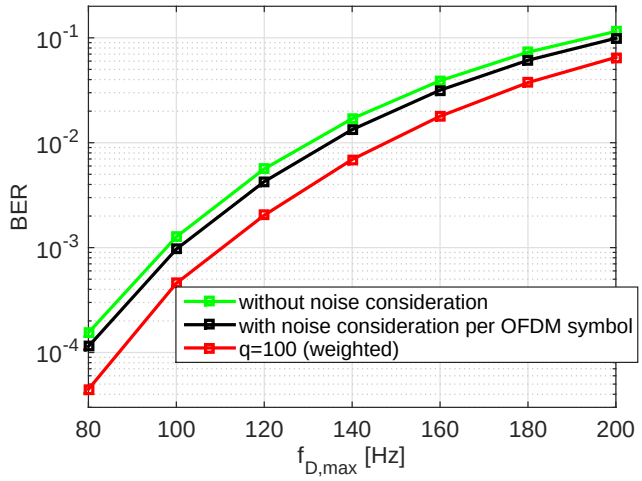

Figure 4.7.: Performance of MRC in a TU6 channel with different noise considerations. Simulation settings are summarized in Table 4.3.

4.5. Noise Estimation for SIMO Combining

4.5.1. Output Noise Estimation

After SIMO combining, the output noise can be written as

$$\hat{\sigma_t^2}(k) = \tilde{\mathbf{W}}^H(k)\, E\left\{\check{\mathbf{X}}_t(k)\,\check{\mathbf{X}}_t^H(k)\right\}\tilde{\mathbf{W}}(k), \tag{4.38}$$

where

$$\check{\mathbf{X}}_t(k) = \begin{bmatrix} X_{t,1}(k) \\ \vdots \\ X_{t,M}(k) \end{bmatrix} \tag{4.39}$$

with $X_{t,m}(k)$ as the total input noise+ICI distortion induced on subcarrier k and antenna m.

In the case of OC (or SDCC), the estimate of total input noise+ICI induced on one subcarrier is available through the interference plus noise matrix $\mathbf{Z}(k)$ defined in (4.21). Therefore, the estimated output noise can be written as:

$$\begin{aligned} \hat{\sigma_t^2}(k) &= \tilde{\mathbf{W}}_{OC}^H(k)\,\mathbf{Z}(k)\,\tilde{\mathbf{W}}_{OC}(k) \\ &= \check{\mathbf{H}}^H(k,k)\,\mathbf{Z}^{-1}(k)\,\mathbf{Z}(k)\,\mathbf{Z}^{-1}(k)\,\check{\mathbf{H}}(k,k) \\ &= \check{\mathbf{H}}^H(k,k)\,\mathbf{Z}^{-1}(k)\,\check{\mathbf{H}}(k,k) = \tilde{\mathbf{W}}_{OC}^H(k)\,\check{\mathbf{H}}(k,k). \end{aligned} \tag{4.40}$$

In the case of MRC, the estimate of total noise+ICI induced on one subcarrier is available through the total noise+ICI covariance matrix $\check{\mathbf{C}}(k)$, defined in (4.33)

$$\begin{aligned}\hat{\sigma_t^2}(k) &= \tilde{\mathbf{W}}_{mrc}^H(k)\,\check{\mathbf{C}}^{-1}(k)\,\tilde{\mathbf{W}}_{mrc}^H(k)\\ &= \check{\mathbf{H}}^H(k,\,k)\,\check{\mathbf{C}}^{-1}(k)\,\check{\mathbf{C}}(k)\,\check{\mathbf{C}}^{-1}(k)\,\check{\mathbf{H}}(k,\,k)\\ &= \check{\mathbf{H}}^H(k,\,k)\,\check{\mathbf{C}}^{-1}(k)\,\check{\mathbf{H}}(k,\,k)\\ &= \tilde{\mathbf{W}}_{mrc}^H(k)\,\check{\mathbf{H}}(k,\,k).\end{aligned} \tag{4.41}$$

From (4.41) and (4.40), we can see that the general equation for computing the output noise variance after combining can be written as

$$\hat{\sigma_t^2}(k) = \tilde{\mathbf{W}}^H(k)\,\check{\mathbf{H}}(k,\,k). \tag{4.42}$$

4.5.2. Input Noise Estimation

As shown in (4.21), knowledge of the noise covariance matrix $\check{\mathbf{C}}_{\text{Noise}}$ is needed to build the interference plus noise matrix $\mathbf{Z}(k)$. In addition, the noise information is also needed to build the MMSE filtering vector in (3.26). This information can be obtained through PANE. However, in a mobile environment, practical PANE will capture the combined effect of noise plus ICI power. In our implementation, we use (4.43) to (4.45) to separate the ICI power from the total noise power captured through PANE:

1.
$$\hat{\sigma}_{ici}^2(k) = \sum_{d=-D,d\neq 0}^{D} |H(k,\,k+d)|^2 \overset{(4.24)}{\approx} \kappa^2 \left(\sum_{d=-D,\,d\neq 0}^{D} \left(\frac{1}{d}\right)^2\right) |H(k,\,k+1)|^2 \tag{4.43}$$

2.
$$\hat{\sigma}_m^2(k) = \hat{\sigma}_{t,m}^2(k) - \hat{\sigma}_{ici}^2, \tag{4.44}$$

3.
$$\check{\mathbf{C}}_{\text{Noise}}(k) = \begin{bmatrix} \hat{\sigma}_1^2(k) & & \\ & \ddots & \\ & & \hat{\sigma}_M^2(k) \end{bmatrix}, \tag{4.45}$$

where $\hat{\sigma}_{t,m}^2(k)$ is obtained from the PANE. In Figure 4.8, we can see the effect of the way the noise covariance matrix $\check{\mathbf{C}}_{\text{Noise}}(k)$ is built on the BER performance of the SDCC combiner. As shown, the best performance is achieved when genie-aided information of the actual noise variance is used to build the noise covariance matrix as $\check{\mathbf{C}}_{\text{Noise}} = \sigma^2\mathbf{I}_M$, $\forall k$, observed through the green curve.

If no separation is applied, i.e., the noise covariance matrix is set as $\check{\mathbf{C}}_{\text{Noise}}(k) = \begin{bmatrix} \hat{\sigma}_{t,1}^2(k) & & \\ & \ddots & \\ & & \hat{\sigma}_{t,M}^2(k) \end{bmatrix}$, significant degradation is encountered, through the black

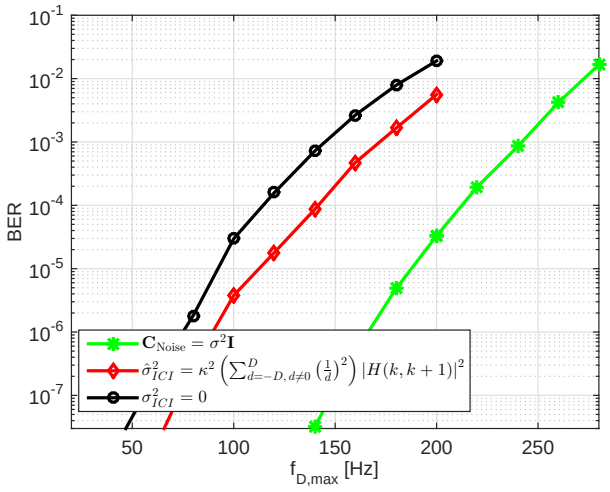

Figure 4.8.: BER performance of SDCC vs Doppler shift at $\Gamma = 30\,\mathrm{dB}$. Simulation settings summarized in Table 4.4

curve. By estimating the average ICI power through (4.43), a much better performance is obtained (red curve), which, however, still lags behind the performance of the optimum setting for $\check{\mathbf{C}}_{\mathrm{Noise}}(k)$ by around 70 Hz, indicating a room for significant improvement by a better estimation of $\check{\mathbf{C}}_{\mathrm{Noise}}(k)$.

In Figure 4.9, we can see the same comparison vs SNR. As shown, a smaller error floor is encountered, in the displayed SNR range, by estimating the average ICI power through (4.43) (black curve vs red curve). However, significant degradation from the ideal case is also clear.

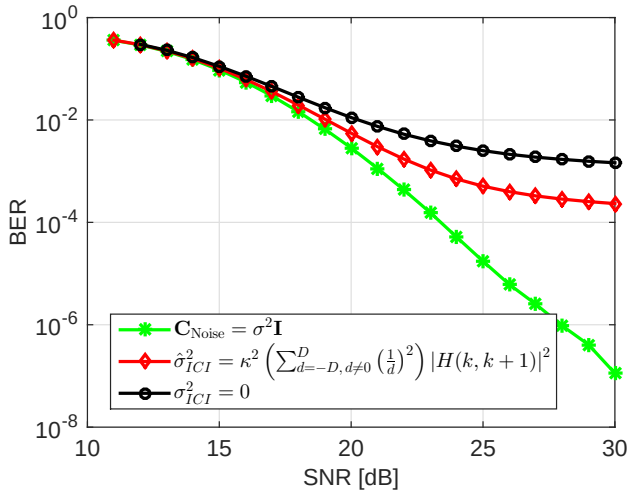

Figure 4.9.: BER performance of SDCC vs SNR at $f_{D,max} = 150\,\text{Hz}$. Simulation settings summarized in Table 4.4

Parameter	Setting
System	DVB-T
BER	after Viterbi decoding in dependency of Doppler frequency shift/SNR
CSI	PACE using linear interpolation
SNR	30 dB
Doppler frequency shift	150 Hz
Modulation	64QAM
Coding	Viterbi decoding (2/3) traceback depth=252
OFDM	8k FFT , $N_{GI} = 2048$ samples, $N_a = 6817$ subcarriers, $N_{data} = 6048$ subcarriers
Channel	2×1 spatially uncorrelated TU6 channels
OFDM Receiver	SDCC, $D_{simo} = 10$

Table 4.4.: Simulation Parameters used to produce results in Figures 4.8 and 4.9

4.6. Concatenation of SIMO Receivers with ICI Cancelers

In this section, we examine how ICI cancelers can be combined with SIMO diversity receivers. Depending on the order of processing, two architectures are investigated:

1. ICI cancellation first : ICIC→Combining.
2. Combining first: Combining→ICIC.

We rewrite (3.8) considering only a limited number of $2D$ interferers. The received signal at subcarrier position k on antenna m can be written as

$$\begin{aligned} R_m(k) &= H_m(k)\,S(k) + \sum_{d=-D, d\neq 0}^{D} H_m(k,\, k+d) S(k+d) + X_m(k) \\ &= \left[\; H_m(k,\, k-D) \;\; .. \;\; H_m(k,\, k) \;\; .. \;\; H_m(k,\, k+D) \;\right] \begin{bmatrix} S(k-D) \\ \vdots \\ S(k) \\ \vdots \\ S(k+D) \end{bmatrix}_{(2D+1\times 1)} \\ &+ X_m(k) \\ &= \mathbf{H}_{f,m}(k)\,\bar{\mathbf{S}}_{(2D+1\times 1)}(k) + X_m(k), \end{aligned} \tag{4.46}$$

where $\mathbf{H}_{f,m}(k)$ is the ICI frequency vector on antenna m. Throughout this section, we shall use this model for the derivation of the equivalent channel after filtering the received OFDM signal in the frequency domain (MMSE ICIC) or in the spatial domain (MRC, SDCC or OC).

4.6.1. Combining after ICIC

In the first architecture, depicted in Figure 4.10, an ICI cancellation block is placed on each antenna prior to the combining stage. In this case, the equivalent channel is recomputed after a bank of ICI cancelers, using knowledge of the set of filter coefficients $\tilde{\mathbf{W}}_{f,m}$ and knowledge of the input ICI channel coefficients $H_m(k,\, k+d)$.

The derivation of an equivalent channel $\tilde{H}(k,\, k+d)$ for $d > 0$ after ICIC assumes that the ICIC operation can be represented as a filtering operation, as in an MMSE ICIC. When dealing with non-linear equalizers like PIC introduced in section 3.2.2 or successive interference cancellation (SIC) as in [MTV07b], the equivalent channel can not be computed for $d > 0$. Thus in this work, for a second combining stage which requires knowledge of the off-diagonal coefficients (OC or SDCC), we only consider a first stage of MMSE equalization. However, a first stage of PIC or SIC can still be used as a prior stage to MRC with $D_{simo} = 0$, i.e., MRC→PIC can be considered, since MRC requires only knowledge of the main diagonal coefficients.

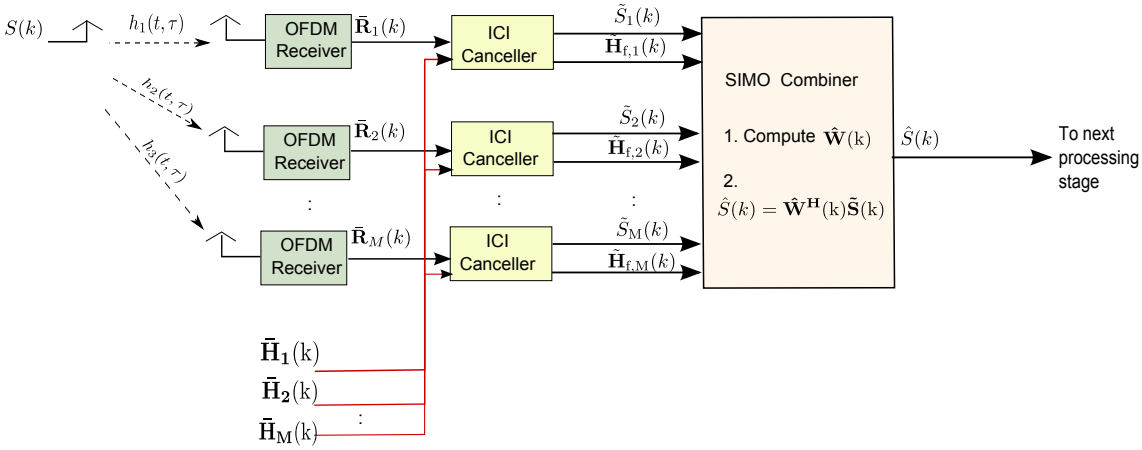

Figure 4.10.: ICI Cancellation Before SIMO Combining

Equivalent Channel after MMSE filtering with SISO ICI Equalization Vector Recalling (3.27), the windowed linear model of the received signal can be written as

$$\bar{\mathbf{R}}_m(k) = \bar{\mathbf{H}}_m(k)\bar{\mathbf{S}}_{(4D+1\times 1)}(k) + \bar{\mathbf{X}}_m(k), \tag{4.47}$$

where $\bar{\mathbf{R}}_m(k)$, $\bar{\mathbf{S}}_{(4D+1\times 1)}(k)$ and $\bar{\mathbf{X}}_m(k)$ are as defined as in (3.28), (3.29) and (3.30), respectively.

After filtering with an ICI equalization vector, the output filtered non-normalized estimated symbol is

$$\begin{aligned}
\tilde{S}_m(k) &= \tilde{\mathbf{W}}_{f,m}^H(k)\bar{\mathbf{R}}_m(k), \\
&= \underbrace{\tilde{\mathbf{W}}_{f,m}^H(k)\bar{\mathbf{H}}_m(k)}_{\tilde{\mathbf{H}}_{f,m}(k)}\bar{\mathbf{S}}_{4D+1\times 1}(k) + \underbrace{\mathbf{W}_{f,m}^H\bar{\mathbf{X}}_m(k)}_{\tilde{X}_m(k)}, \\
&= \tilde{\mathbf{H}}_{f,m}(k)\begin{bmatrix} S(k-2D) \\ \vdots \\ S(k) \\ \vdots \\ S(k+2D) \end{bmatrix} + \tilde{X}_m(k),
\end{aligned} \tag{4.48}$$

where $\tilde{\mathbf{W}}_{f,m}(k) = \tilde{\mathbf{W}}_{f,(2D+1\times 1)}$ defined in (3.33) on antenna m. Comparing (4.48) with the original model in (4.46), we can conclude that the equivalent channel of length $4D+1$ can be written as

$$\tilde{\mathbf{H}}_{f,m}(k) = \begin{bmatrix} \tilde{H}_m(k,\, k-2D) & .. & \tilde{H}_m(k,\, k) & .... & \tilde{H}_m(k,\, k+2D) \end{bmatrix} = \tilde{\mathbf{W}}_{f,m}^H(k)\bar{\mathbf{H}}_m(k) \tag{4.49}$$

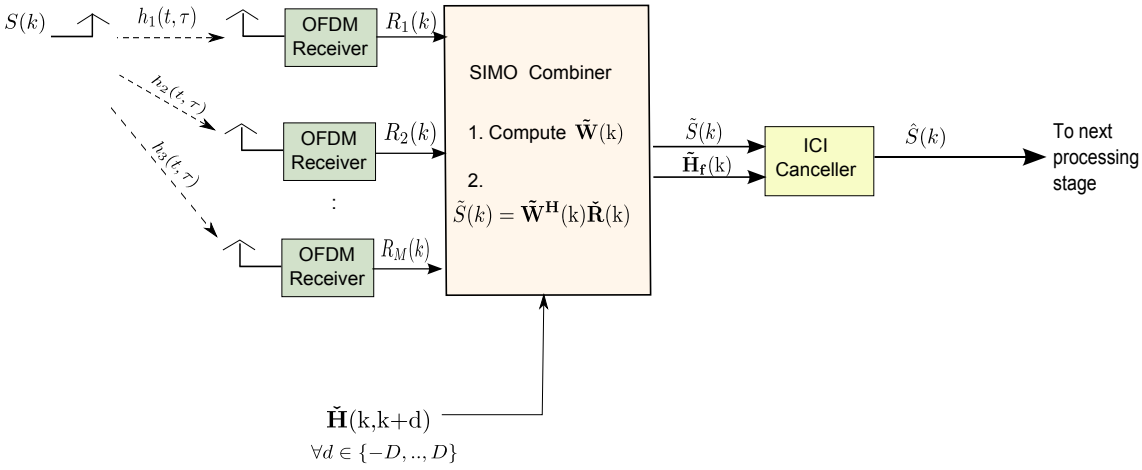

Figure 4.11.: ICI Cancellation After SIMO Combining

As we can see, the equivalent channel after frequency filtering is of length $4D+1$, which means the number of interferers considered is doubled from $2D$ to $4D$. In other words, by filtering the received sequence, the length of the effective channel has increased by the length of the filter, which is intuitively satisfying.

4.6.2. ICIC after Combining

In the second architecture, depicted in Figure 4.11, the combining stage is followed by an ICIC. In this case, the equivalent channel after the SIMO diversity receiver needs to be recomputed before the ICI cancellation stage. We should also note that the first stage (in both architectures ICIC→combining and combining→ICIC) should not normalize the intermediate output signal, which we shall refer to here as $\tilde{S}(k)$. Instead the normalization is carried out in the second stage.

Equivalent Channel after SIMO Combining Using (4.5), the non-normalized output of the SIMO combiner can be written as

$$\tilde{S}(k) = \tilde{\mathbf{W}}^{H}_{(M\times 1)}(k)\,\check{\mathbf{R}}(k)\,. \tag{4.50}$$

Using (4.46) and (4.2), $\tilde{S}(k)$ can be written as

$$\begin{aligned}\tilde{S}(k) &= \tilde{\mathbf{W}}^{H}_{(M\times 1)}\begin{bmatrix}\mathbf{H}_{f,1}(k)\\ \vdots \\ \mathbf{H}_{f,M}(k)\end{bmatrix}_{M\times 2D+1}\bar{\mathbf{S}}_{(2D+1\times 1)}(k) + \tilde{\mathbf{W}}^{H}_{(M\times 1)}\begin{bmatrix}X_1(k)\\ \vdots \\ X_M(k)\end{bmatrix}\\ &= \tilde{\mathbf{H}}_{f,(1\times 2D+1)}(k)\,\bar{\mathbf{S}}_{(2D+1\times 1)}(k) + \tilde{X}(k)\,,\end{aligned} \tag{4.51}$$

where $\mathbf{H}_{f,m}(k)$ is the ICI frequency vector at the m^{th} antenna built as

$$\mathbf{H}_{f,m}(k) = \left[\; H_m(k,\, k-D) \quad .. \quad H_m(k,\, k) \quad .. \quad H_m(k,\, k+D) \; \right]. \tag{4.52}$$

Comparing (4.51) with the original model in (4.46), we see that the equivalent channel can be computed as

$$\tilde{\mathbf{H}}_{f,(1\times 2D+1)}(k) = \tilde{\mathbf{W}}^{H}_{(M\times 1)}(k) \begin{bmatrix} \mathbf{H}_{f,1}(k) \\ \vdots \\ \mathbf{H}_{f,M}(k) \end{bmatrix}_{(M\times 2D+1)} . \tag{4.53}$$

Alternatively, the $(D+d)^{th}$ element in $\tilde{\mathbf{H}}_{f,1\times 2D+1}(k)$, which is the interference of subcarrier $k+d$ on subcarrier k can be computed as

$$\tilde{H}(k,\, k+d) = \tilde{\mathbf{W}}^{H}_{(M\times 1)}(k)\, \check{\mathbf{H}}_{(M\times 1)}(k,\, k+d), \tag{4.54}$$

where $\check{\mathbf{H}}_{(M\times 1)}(k,\, k+d)$ is built as in (4.25).

4.7. Summary of Results for SIMO receivers

4.7.1. Results on Concatenation of MRC Receiver with PIC

In this section, we compare simulation results of the two architectures PIC→MRC vs MRC→PIC. In Table 4.5, we list the settings used in these simulations.

In Figure 4.12, the BER of PIC→MRC vs MRC→PIC is compared in two different settings:

1. the ZF QAM symbol estimates are fed into the ICI subtraction block in Figure 3.9 (green curves).

2. the genie aided QAM symbols (actual transmitted QAM symbols) are fed into the ICI subtraction block in Figure 3.9 instead of the estimated QAM symbols at the output of the ZF block (red curves).

As we can see, in the case when the ICI subtraction block is fed with the genie aided symbols, the order of MRC and ICIC does not affect the BER curves, where both red starred and red squared curves overlap. However, in the realistic case, when the estimates given to the ICI subtraction block are obtained from the ZF block, a performance gap of around 15 Hz is observed, where the architecture MRC→PIC can deliver a better performance.

In Figure 4.13, the frequency domain channel is shown on antenna 1 vs the equivalent channel after MRC. We can see that as expected after combining, the equivalent channel does not suffer from spectral nulls and therefore applying ZF after such a channel transfer function produces more reliable QAM symbol estimates. Indeed the reliability of the initial QAM symbol estimates fed into the ICI subtraction block is the main reason behind the performance gap shown in Figure 4.12 between the two architectures.

Parameter	Setting
System	DVB-T
BER	after Viterbi decoding in dependency of Doppler shift
CSI	PACE using linear interpolation
noise estimation	PANE after PIC , (4.41) after MRC
SNR	30 dB
Modulation	64QAM
Coding	Viterbi decoding (2/3) traceback depth=252
OFDM	8k FFT , $N_{GI} = 2048$ samples, $N_a = 6817$ subcarriers $N_{data} = 6048$ subcarriers
Channel	2×1 spatially uncorrelated TU6 channels
ICIC	PIC:$D = 3$. MMSE:$D = 1$
OFDM Receiver	PIC→MRC, MRC→PIC MMSE→MRC and MRC→MMSE

Table 4.5.: Simulation Parameters used to produce results in Figures 4.12 to 4.20

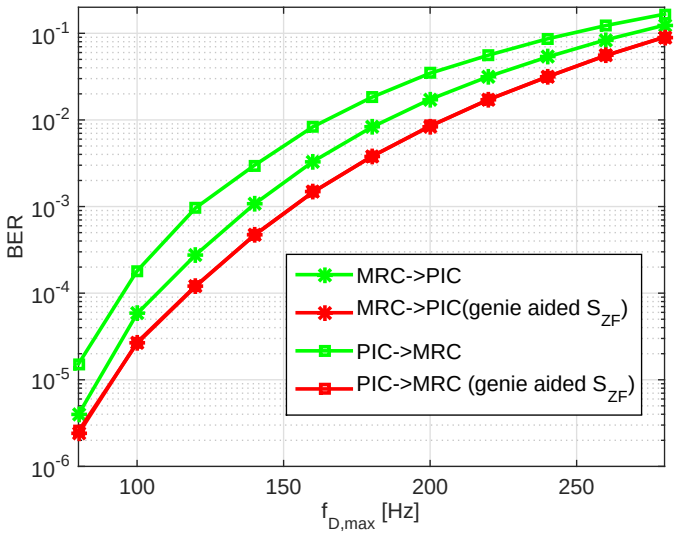

Figure 4.12.: MRC→PIC vs PIC→MRC. Simulation settings summarized in Table 4.5.

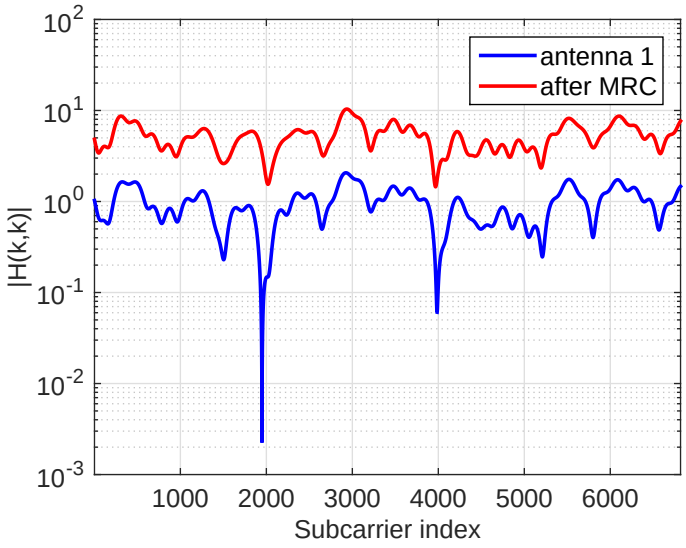

Figure 4.13.: Magnitude of frequency domain channel on first antenna vs equivalent frequency domain channel after MRC at $f_{D,max} = 150Hz$ and $\Gamma = 30\,\mathrm{dB}$

4.7.1.1. Results on Enhanced PIC →MRC

In this work we propose several measures to monitor or increase the reliability of the initial QAM symbol estimates applied to the second stage of the PIC block in Figure 3.9 (ICI subtraction block). These measures include:

1. Dropping unreliable QAM symbols: Unreliable QAM symbols can be detected (and later dropped) using

   a) QAM symbol based threshold: QAM symbols which exceed a certain threshold in amplitude are considered unreliable.
   At subcarrier positions where the frequency domain channel magnitude $|H(k,\,k)|$ is small (below noise+ICI level), the ZF QAM symbol estimates have a large amplitude and in turn this lead to error propagation when those unreliable QAM symbols are fed to the ICI subtraction block in Figure 3.9. Therefore, QAM symbols whose real or imaginary components exceed a threshold a_{drop} are dropped, i.e., set to zero and therefore not considered in the ICI subtraction step.

   b) channel based threshold: another approach to detect unreliable QAM symbols is to identify the positions where the frequency domain channel magnitude $|H(k,\,k)|$ is low. An SIR threshold Υ_{th} is set, where all QAM symbols with low SIR, $\Upsilon_1(k) = \frac{|H(k,k)|^2}{|H(k,k+1)|^2} < \Upsilon_{th}$, are dropped. The SIR function was initially defined in MMSE-ASW ICIC in (3.36), where it was used to set $D(k)$.
   In Figure 4.14, we can see the BER of enhanced PIC→MRC via channel

and QAM symbol based dropping after initial ZF stage. We can see, in the zoomed plot at the relevant BER ($1e-4$ as explained in Chapter 2) in Figure 4.14b, that the channel and symbol based dropping reduced the gap between PIC→MRC and MRC→PIC from around 15 Hz to around 4 Hz and 6 Hz, respectively. Using the settings in Table 4.5, a threshold of $\Upsilon_{th} = 6$ dB gives a slightly better performance than $\Upsilon_{th} = 3$ dB or $\Upsilon_{th} = 9$ dB. With symbol based dropping, the best threshold is found to be $a_{drop} = 1.25$.

2. noise reduction by applying hard decision on the initial symbol estimates at the input to the ICI subtraction block.

3. noise reduction by saturating the initial QAM symbol estimates' real and imaginary components at a value of a_{sat}, before input to the ICI subtraction block.
In Figure 4.15, we can see that the performance gap between PIC→MRC and MRC→PIC is bridged via applying hard decision or saturation on the initial QAM symbol estimates' real and imaginary components at a value of a_{sat}. Applying hard decision requires knowledge of the QAM constellation used and in addition, extra computations because of the used slicer. Using normalized 64QAM symbols, the maximum magnitude of the real or the imaginary component of a QAM symbol is $a_{max} = 1.0801$. As shown in 4.15b, applying a saturation at $a_{sat} = a_{max}$, gives even a better performance than applying hard decision, because of the error propagation implicit in the latter scheme. Therefore, we do not further consider hard decision as a means to enhance the PIC stage. As we can see, by saturating at $a_{sat} = 2 > a_{max}$, a slightly worse performance is encountered compared to saturating at $a_{sat} = a_{max}$, which is intuitively satisfying, since more estimation noise is suppressed in the latter case.

4. replacing ZF stage by an MMSE-ICIC stage: in Figure 4.16a, we can see the BER of enhanced PIC→MRC via replacing the initial ZF stage with an MMSE-FWS ICIC of $D = 1$ stage. The result in Figure 4.16b shows that applying MMSE-ICIC as an initial stage (MMSE-ICIC →PIC→MRC) gives a better performance than MRC→PIC, at the expense of higher complexity. Applying an enhanced PIC stage (with MMSE-ICIC initial estimation) after MRC (MRC→MMSE-ICIC →PIC) results in better performance than (MMSE-ICIC→PIC→MRC), as shown in Figure 4.16b. The gap, however, between MRC→MMSE-ICIC →PIC and MMSE-ICIC →PIC→MRC is reduced to around 4 Hz compared to the 15 Hz gap between MRC→PIC and PIC→MRC. Seeking a trade-off between performance and complexity, we also investigated applying an MMSE-ASW ICIC as an initial ICIC stage with $D_{max} = 1$, i.e., the initial ICIC stage has an option of applying either ZF or MMSE-ICIC with $D = 1$ depending on the SIR at every subcarrier position and the given Υ_{th}. Applying MMSE-ASW ICIC with $\Upsilon_{th} = 8$ dB gives a comparable performance to MRC→MMSE-FWS ICIC→PIC on only 18% of the subcarriers, as shown in the BER Figure 4.16b and the histogram in Figure 4.17. In Figure 4.18, we can see that using PIC→MRC with initial stage of MMSE (MMSE-ICIC→PIC→MRC), a better BER performance can be achieved compared to that

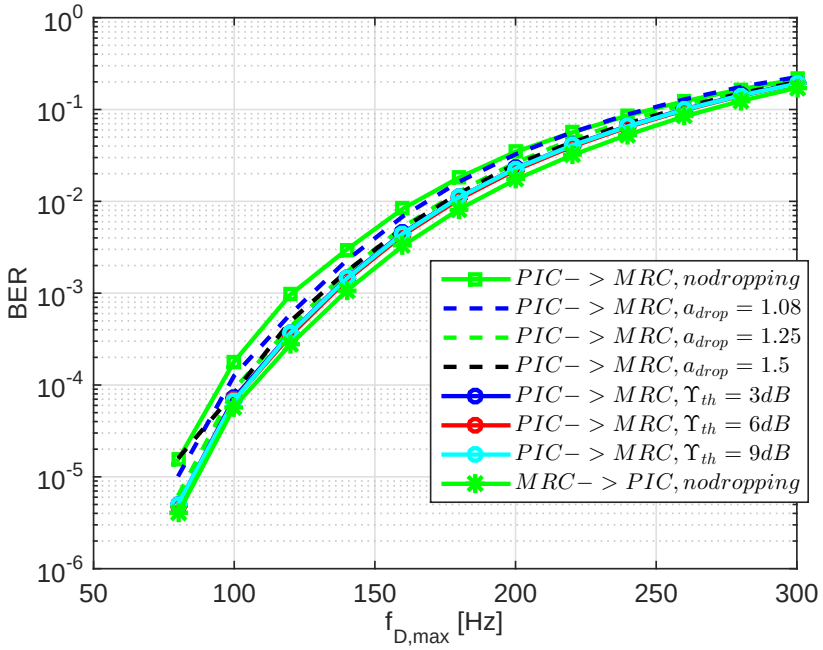

(a) BER vs Doppler frequency range

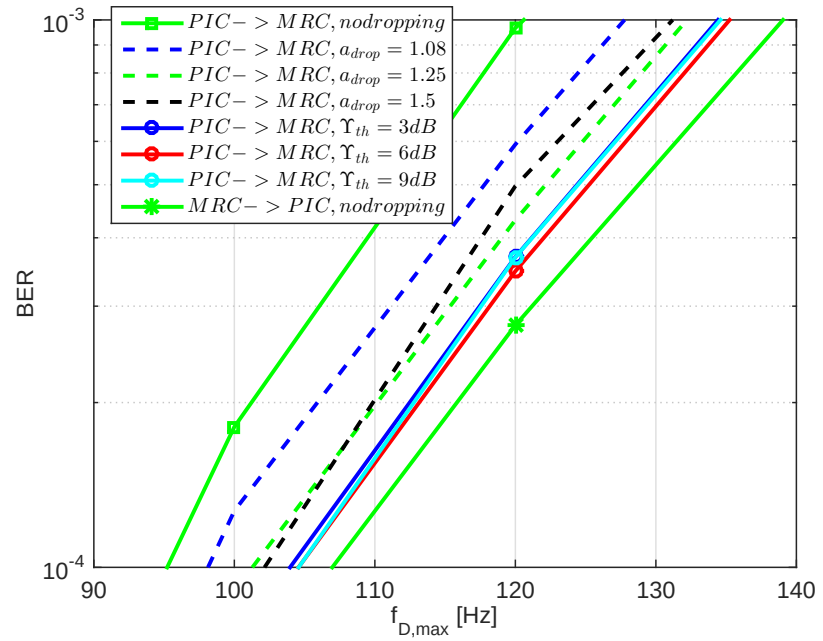

(b) Zoomed BER plot

Figure 4.14.: Enhanced PIC →MRC via channel and symbol based threshold symbol dropping after first ZF stage. Simulation settings summarized in Table 4.5

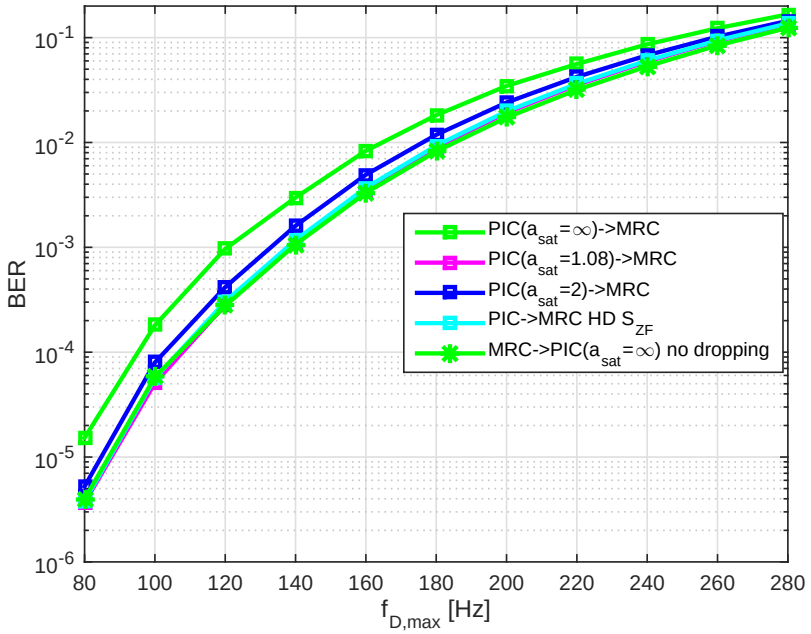

(a) BER vs Doppler frequency range

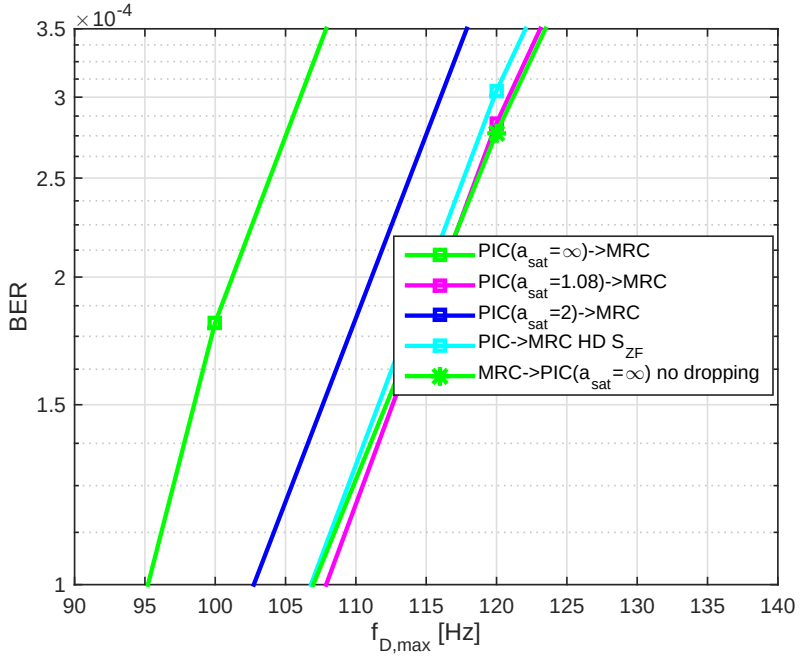

(b) Zoomed BER plot

Figure 4.15.: Enhanced PIC→MRC via saturation and hard decision after ZF at quasi-error free BER. Simulation settings summarized in Table 4.5

of MMSE-ICIC→MRC, which is intuitively satisfying.

Approaches based on 1a, 2 and 3 require that the QAM constellation used is known at the receiver side. This requirement might not be feasible, for example in the case when different QAM constellations are used on the different subcarriers. Channel based dropping eliminates the need to know the used QAM constellation, however, the optimum SIR threshold Υ_{th} will depend on the channel domain channel. Using an initial MMSE-ICIC stage does not require knowledge of the QAM constellation nor parameter optimization, but it comes at the cost of higher complexity.

In Figure 4.19, we can see a comparison of all proposed enhancements of PIC→MRC against the architecture MRC →PIC. We can see that the gap between the two architectures depend on the quality of the initial QAM symbols fed to the ICI subtraction stage as follows:

1. with genie-aided QAM symbols, both architectures give the exact same performance.
2. with ZF receiver, the Doppler frequency gap is $\sim 15\,\text{Hz}$ as mentioned earlier.
3. with enhanced initial QAM symbol estimation, via an initial MMSE-ICIC stage or via QAM symbol saturation, the gap reduces to around 4 Hz.

4.7.2. Results on Concatenation of MRC Receiver with MMSE ICI Canceler

In Figure 4.20, we can see the performance of MMSE-ICIC→MRC vs the performance of MRC→MMSE-ICIC. Unlike the comparison in Figure 4.12, we can see that the order of combining and ICI cancellation does not affect the BER performance when the ICI cancellation is done using MMSE-ICIC.

Though a concatenation of MMSE-ICIC equalizer followed by an SDCC or an OC combining stage is possible, as discussed in section 4.6.1, a limited Doppler frequency gain can be achieved with this architecture, as shown in Figure 4.21, where the architecture MMSE-ICIC →SDCC gives almost the same performance as MMSE-ICIC→MRC and even a worse performance than SDCC standalone. An analysis of this architecture can be found in Appendix B for the interested reader.

4.7.3. Results on Enhanced MRC with Colored Noise Information

In Figures 4.22 to 4.27, the BER of the enhanced MRC using (4.41) vs the noise window size q is shown. The simulation parameters used are summarized in Table 4.7.

Compared to the conventional solution, where all CoPs are averaged to get one noise variance value per OFDM symbol (performance highlighted in circles), we can see how the noise windowing can lead to a lower error floor at $f_{D,max} = 150\,\text{Hz}$ for 4 and 16QAM and at $f_{D,max} = 90\,\text{Hz}$ for 64QAM, as shown in Figures 4.25 to 4.27. Same behavior is observed at a constant SNR= 30 dB, in Figures 4.22 to 4.24.

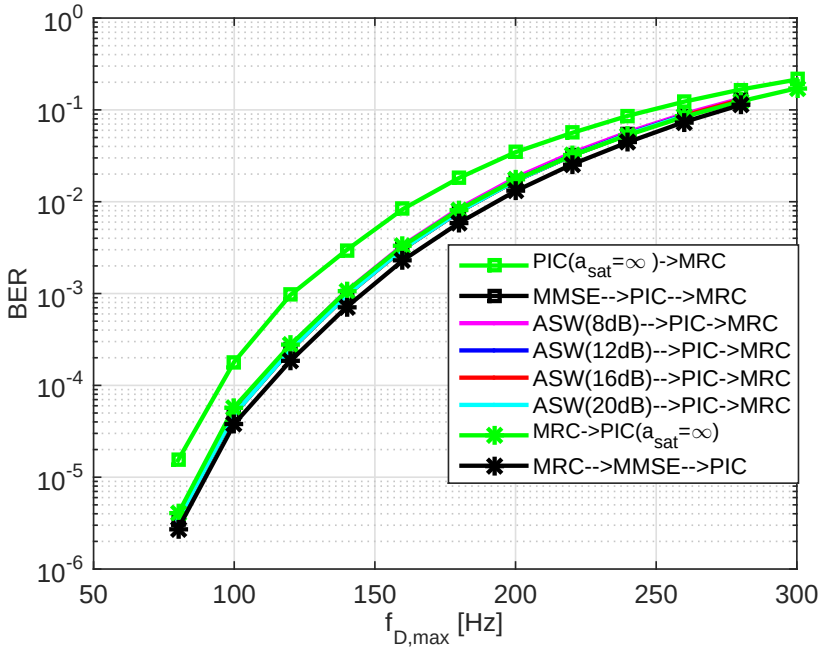

(a) BER vs Doppler frequency range

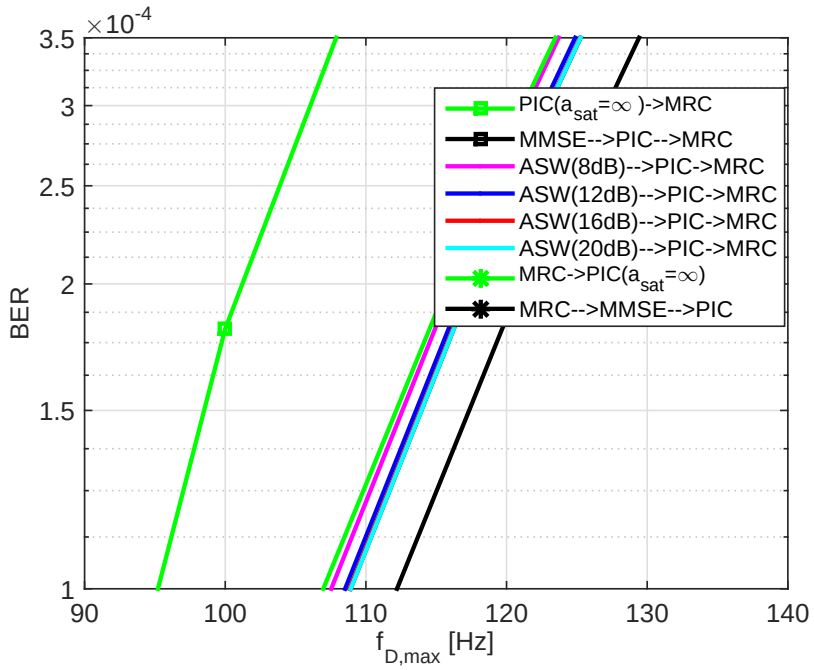

(b) Zoomed BER plot

Figure 4.16.: Enhanced PIC→MRC via an initial MMSE-ICIC stage. Simulation settings summarized in Table 4.5.

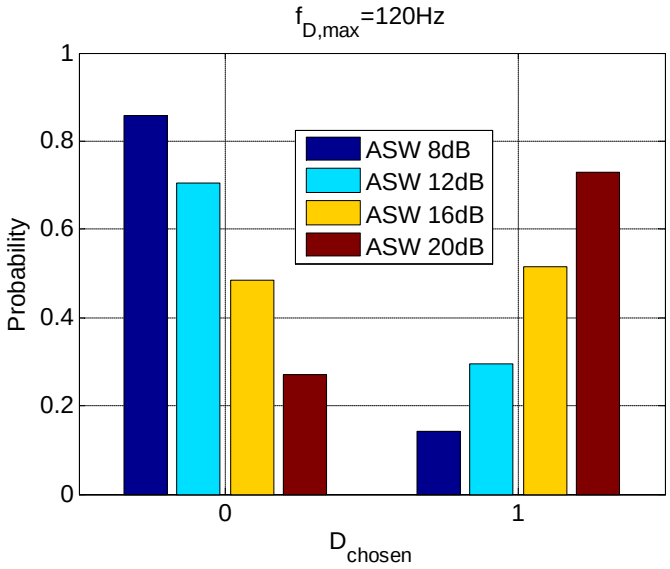

Figure 4.17.: Histogram of selected D by ASW-ICIC in ASW-ICIC→ICI-C. Simulation settings summarized in Table 4.5.

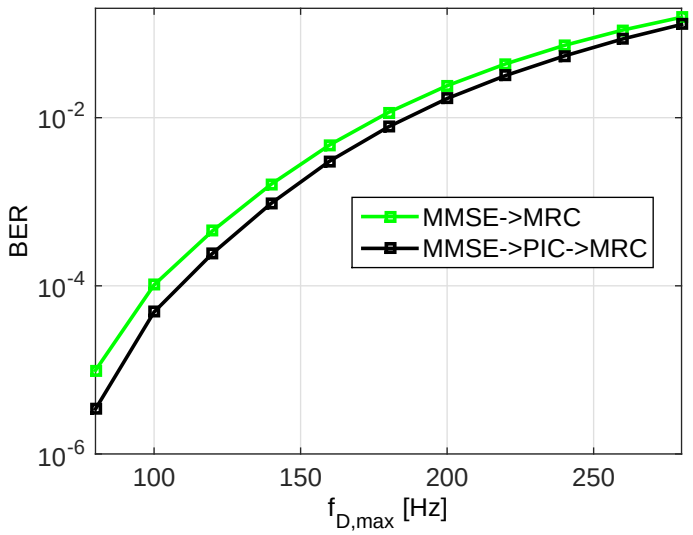

Figure 4.18.: MMSE-ICIC→MRC vs PIC→MRC with initial stage of MMSE-ICIC. Simulation settings summarized in Table 4.5.

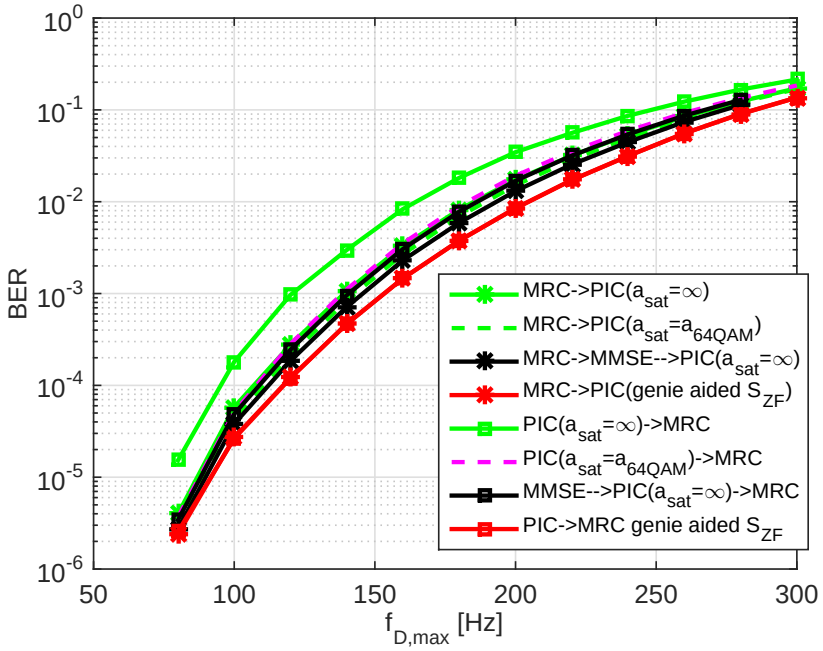

(a) MRC→PIC vs PIC→MRC (different variants).

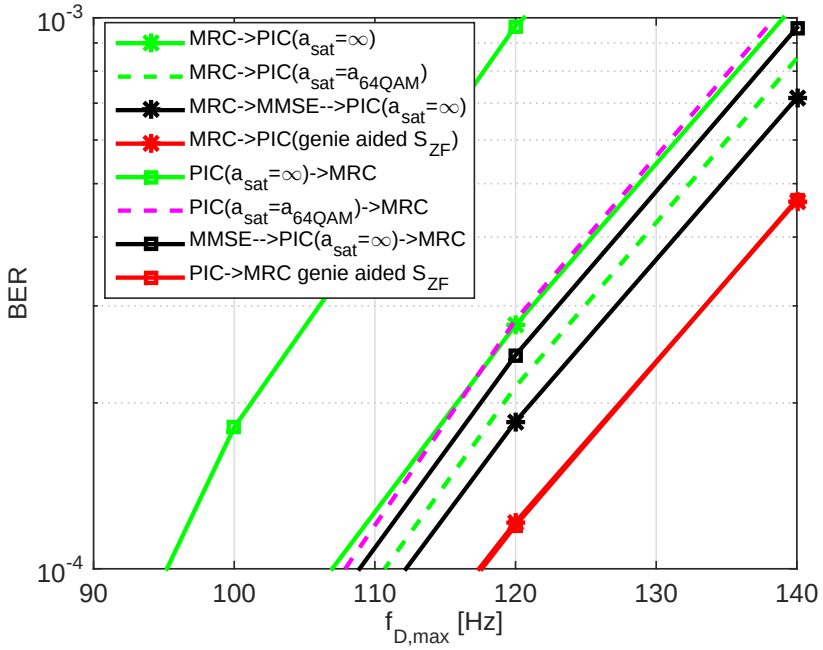

(b) Zoomed BER plot

Figure 4.19.: MRC→PIC vs PIC→MRC at the relevant BER. Simulation settings summarized in Table 4.5

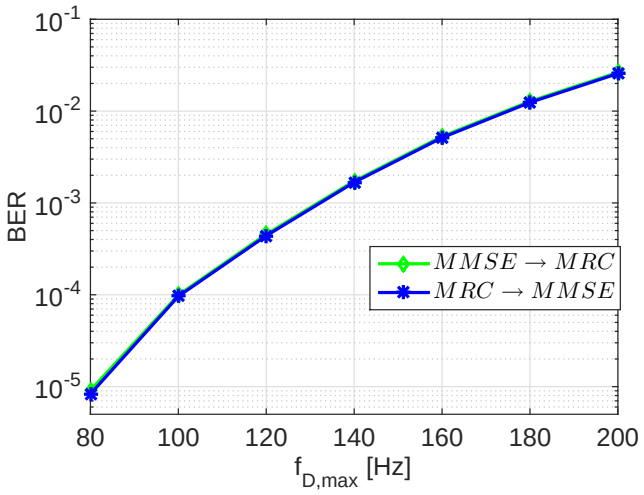

Figure 4.20.: MRC→MMSE-ICIC vs MMSE-ICIC→MRC at the relevant BER. Simulation settings summarized in Table 4.6.

Parameter	Setting
System	DVB-T
BER	after Viterbi decoding in dependency of Doppler shift
CSI	PACE using linear interpolation
noise estimation fed to demapper	after MRC using (4.41)
SNR	30 dB
Modulation	64QAM
Coding	Viterbi decoding (2/3) traceback depth=252
OFDM	8k FFT , 2048 samples GI
	$\Delta f = 1.116\,\text{kHz}$, $N_a = 6817$ subcarriers, $N_{data} = 6048$ subcarriers
Channel	2×1 spatially uncorrelated TU6 channels
OFDM Receiver	MMSE→MRC,MMSE-ICIC→SDCC and SDCC. MMSE:$D = 1$, SDCC:$D_{simo} = 10$

Table 4.6.: Simulation Parameters used to produce results in Figure 4.21

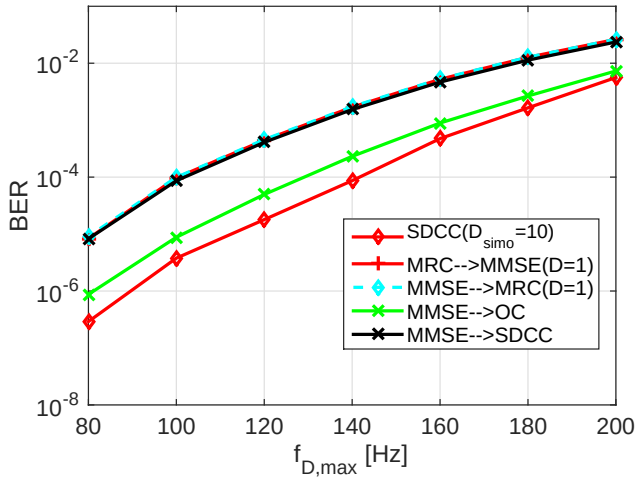

Figure 4.21.: Performance of MMSE-ICIC→OC. Simulation settings summarized in Table 4.6.

At low SNR, very small window sizes (such as $q = 5$ samples) can lead to a worse performance, as shown in Figures 4.25 to 4.27.

We can also see that the weighting proposed in (4.36) has significantly decreased the dependency of the BER performance of the enhanced MRC on the selected noise window size. The curves with the proposed weighting criterion in (4.36) have a much flatter shape than the curves with the rectangular weighting according to (4.35). In addition, they exhibit lower BER in comparison to their non-weighted counterparts.

In Figure 4.28, we see the BER performance of conventional MRC and enhanced MRC with weighted CoP PANE at $q = 100$ CoPs for TU6 and 2TU6 channels, using 4QAM, 16QAM and 64QAM modulation. The used 2TU6 channel (explained in section 2.3.3) had a delay of $\tau_2 = 0.15 N_{GI} T \approx 0.134\,\text{msec}$ and $k_2 = -3\,\text{dB}$. As we can see, using a weighted noise window of $q = 100$ CoPs is effective over a wide Doppler frequency range and with even a higher frequency selective channel. We can see in Figure 4.28 a flattening of the BER curve at low Doppler shifts for 4QAM. The error floor is caused by the very high frequency selectivity of the channel which the linear channel interpolation is not able to track accurately.

Figure 4.29 shows the BER vs Doppler frequency shift of MRC with weighted CoP PANE at the input to MRC for TU6 and 2TU6 channels using GACN and 64QAM modulation. Because GACN is used, we do not see the error floor obvious as in Figure 4.28. We can clearly see that the Doppler gain obtained from colored noise estimation decreases as the frequency selectivity increases, from around 9 Hz gain in a TU6 channel to around 4 Hz gain in a 2TU6 channel. This is intuitively satisfying because with the increase in the frequency selectivity, the sparse arrangement of the continual pilots is no longer capable of capturing the frequency variation of the total noise+ICI power.

Parameter	Setting
System	DVB-T
BER	after Viterbi decoding in dependency of window size q
CSI	PACE using linear interpolation
Noise estimation fed to demapper	after MRC using (4.41)
SNR	30 dB
Doppler shift ($f_{D,max}$)	$150Hz$ and $90Hz$
Modulation	4QAM ,16QAM and 64QAM
Coding	Viterbi decoding (2/3) traceback depth=252
OFDM	8k FFT , $N_{GI} = 2048$ samples ,$N_a = 6817$ subcarriers $N_{data} = 6048$ subcarriers , $\Delta f = 1.116$ kHz
Channel	2×1 spatially uncorrelated: TU6 channel 2TU6 channel: $\tau_2 = 0.15 N_{GI} T \approx 0.134$ msec and $k_2 = -3$ dB.

Table 4.7.: Simulation Parameters used to produce the results in Figures 4.23 to 4.27

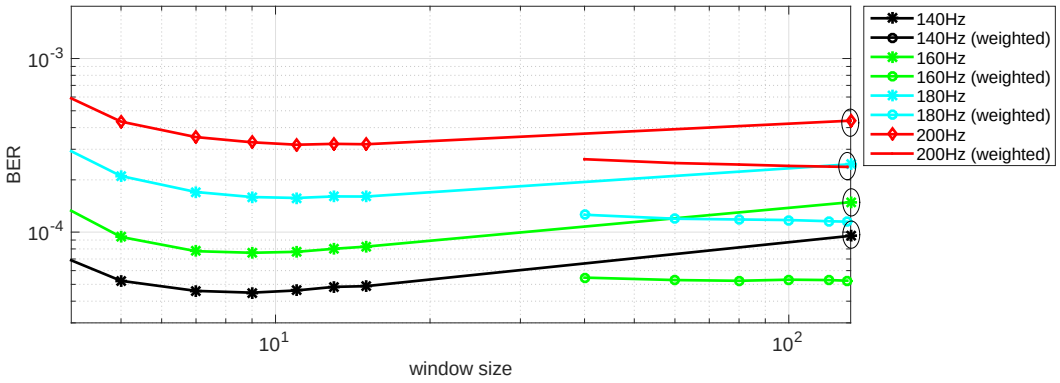

Figure 4.22.: BER vs noise window size for different Doppler shift values at SNR= 30 dB using 4QAM

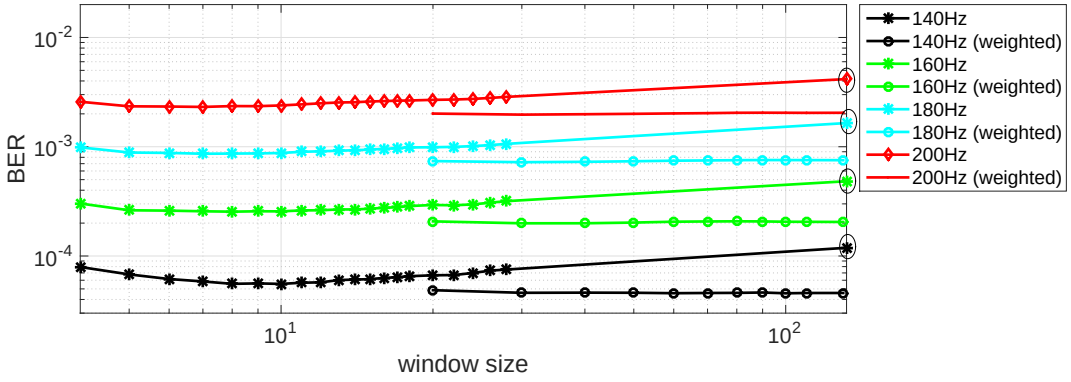

Figure 4.23.: BER vs noise window size for different Doppler shift values at SNR= 30 dB using 16QAM

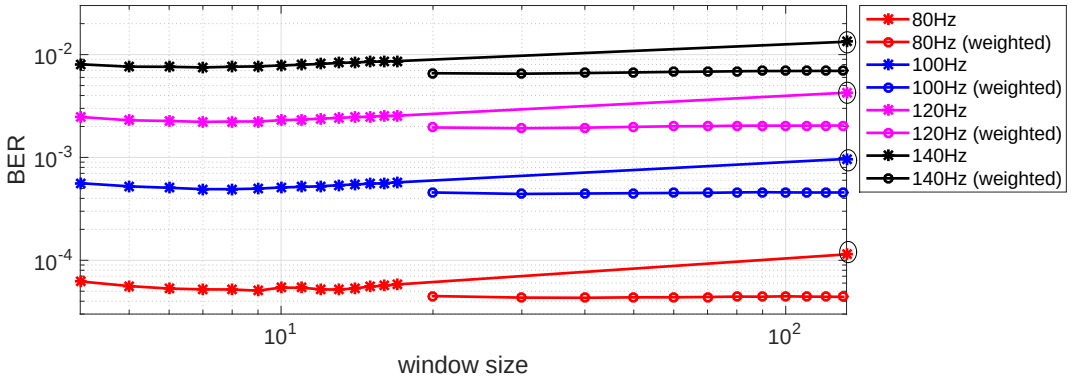

Figure 4.24.: BER vs noise window size for different Doppler shift values at SNR= 30 dB using 64QAM

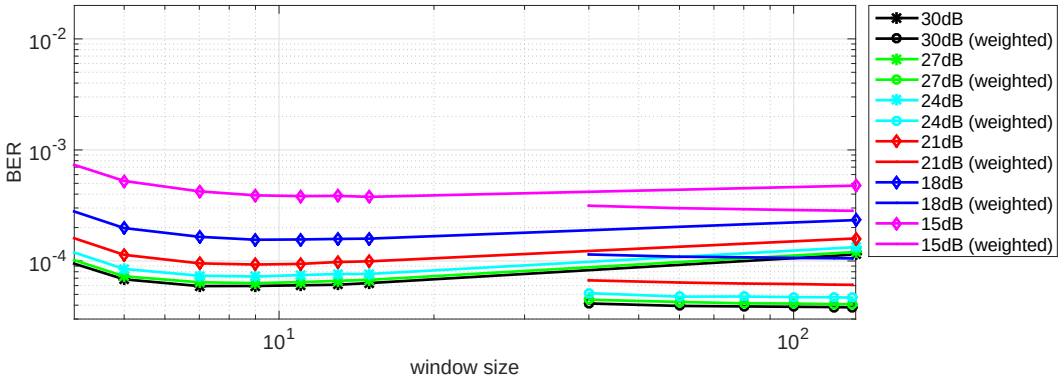

Figure 4.25.: BER vs noise window size for different Doppler shift values at $f_{D,max}$ = 150 Hz using 4QAM

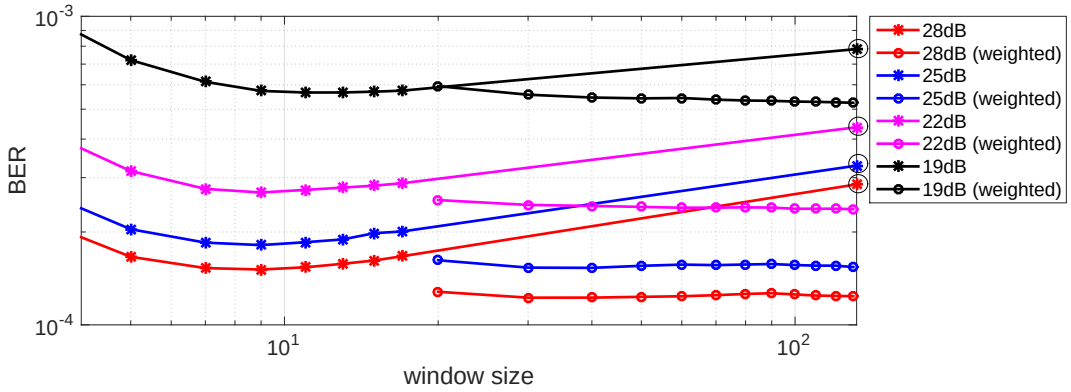

Figure 4.26.: BER vs noise window size for different SNR values at $f_{D,max} = 150\,\text{Hz}$ using 16QAM

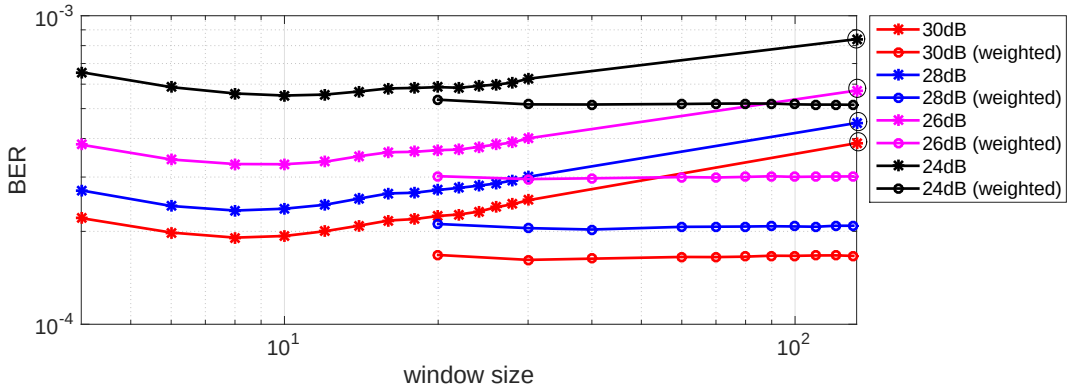

Figure 4.27.: BER vs noise window size for different SNR values at $f_{D,max} = 90\,\text{Hz}$ using 64QAM

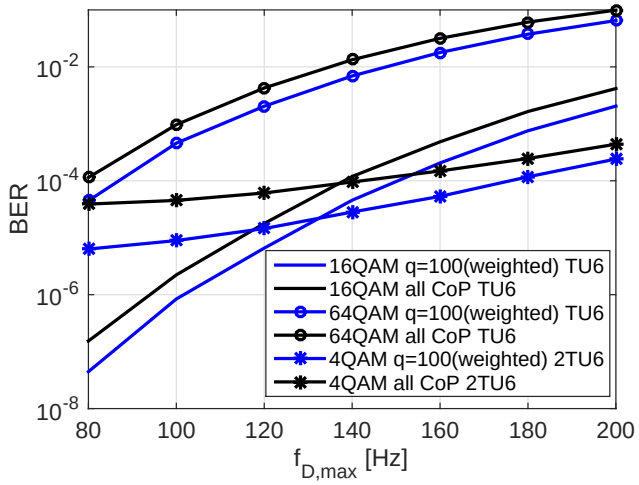

Figure 4.28.: BER of MRC vs Doppler shift with colored noise estimation at the input to MRC for TU6 and 2TU6 channels

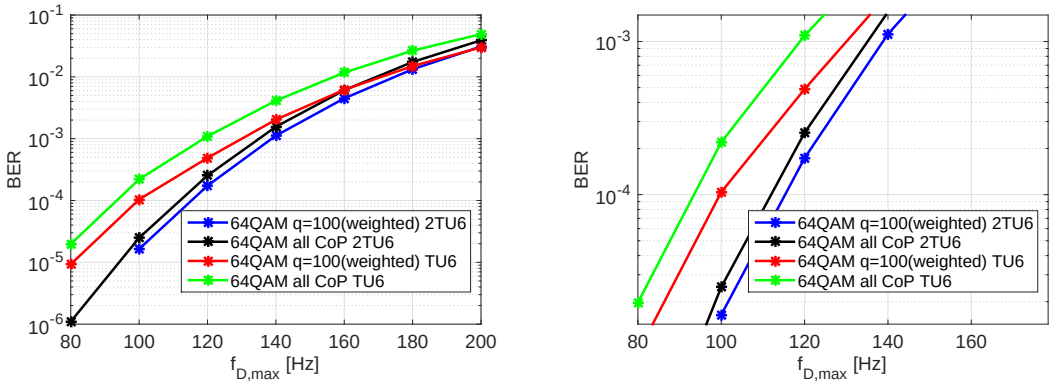

(a) (b) Zoomed plot at quasi-error-free BER.

Figure 4.29.: BER of MRC vs Doppler shift with colored noise estimation at the input to MRC for 2TU6 channel with GACN

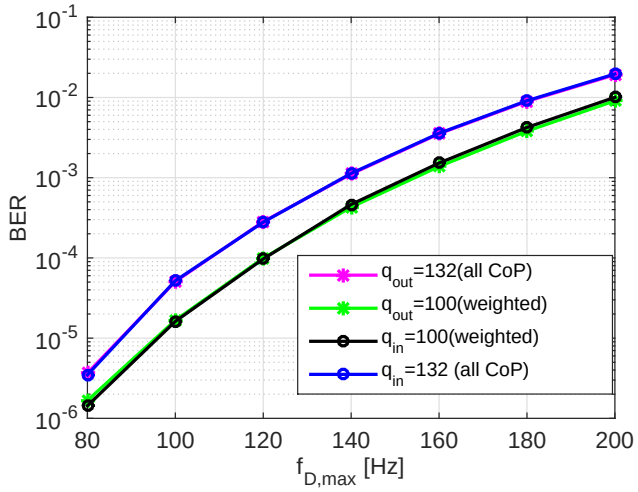

Figure 4.30.: BER of PIC→MRC with colored noise estimation after PIC

4.7.3.1. Enhanced PIC→MRC Using Windowed CoP PANE

In Figure 4.30, we demonstrate the advantage of using windowed CoP PANE on the architecture PIC→MRC. We apply windowed CoP PANE (using noise window size $q = 100$ CoPs plus weighting according to (4.36) and (4.37)) before and after the PIC block (green and black curves, respectively) as shown in Figure 4.30 and as marked in the block diagram in Figure 4.31.

Interestingly, as we see in Figure 4.30, both approaches (computing the colored noise before and after the PIC block) yield the same BER and both are better than considering all CoPs in PANE (shown in magenta and red curves).

Since γ_{in} and γ_{out} are very close in value as shown in Figure 4.32, the overall performance of estimating the noise variance before and after the PIC block are very close. In order to explain why estimating the noise variance before and after the PIC block yields the same performance, we define the noise+ICI inter-channel ratios (across the two antennas) at the input and output of the PIC as

$$\gamma_{in}(k) = \frac{\|X_{t,1}(k)\|^2}{\|X_{t,2}(k)\|^2} \tag{4.55}$$

$$\gamma_{out}(k) = \frac{\left\|\tilde{X}_{t,1}(k)\right\|^2}{\left\|\tilde{X}_{t,2}(k)\right\|^2} \tag{4.56}$$

As shown in Figure 4.32, the signals $\gamma_{in}(k)$ and $\gamma_{out}(k)$ are very close in value and are both colored because of the effect of the ICI . Indeed, this signal is a crucial parameter in determining the weights of the MRC according to (4.33). To make this point clearer, we rewrite (4.32) for 2 antennas as

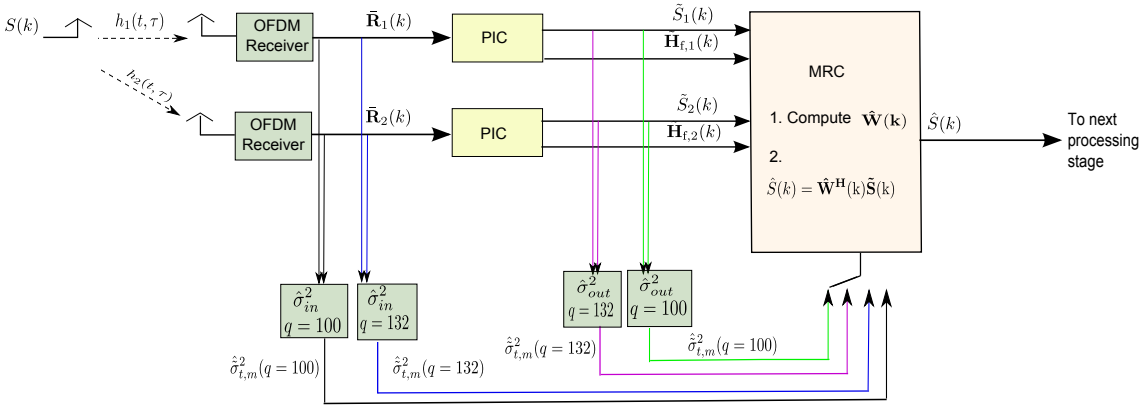

Figure 4.31.: Simplified architecture of the PIC→MRC with the BER result, shown in Figure 4.30, the locations of PANE are marked

$$\begin{aligned}\tilde{\mathbf{W}}_{MRC}(k) &= \breve{\tilde{\mathbf{C}}}^{-1}(k)\,\breve{\tilde{\mathbf{H}}}(k,\,k) = \begin{bmatrix} \tilde{\sigma}^2_{t,1}(k) & \\ & \tilde{\sigma}^2_{t,2}(k) \end{bmatrix}^{-1} \begin{bmatrix} \tilde{H}_1(k,\,k) \\ \tilde{H}_2(k,\,k) \end{bmatrix} \\ &= \frac{1}{\tilde{\sigma}^2_{t,2}(k)} \begin{bmatrix} E\{\gamma_{out}(k)\} & \\ & 1 \end{bmatrix}^{-1} \begin{bmatrix} \tilde{H}_1(k,\,k) \\ \tilde{H}_2(k,\,k) \end{bmatrix}. \end{aligned} \tag{4.57}$$

Since eventually the weighting filter coefficients are going to be normalized, the scalar factor in (4.57) $\tilde{\sigma}^2_{t,2}(k)$ can be ignored, then, the remaining influencing factor is the ratio between the single weights given to each antenna relative to each other, $E\{\gamma_{out}(k)\}$.

In Figure 4.33, we can see the MSE between the genie aided noise+ICI inter-channel ratio and the estimated noise+ICI inter-channel ratio averaged over all frequency sub-carriers for successive OFDM symbols. Noise+ICI inter-channel ratio estimation using weighted windowed PANE with $q = 100$ CoPs is compared against conventional PANE after PIC. Clearly, using a weighted windowed PANE gives a better estimate of the noise+ICI inter-channel ratio and hence a better estimate of the MRC weights, which shows that the total noise is still colored even after applying PIC.

On the other hand, if we look at Figure 4.34, where the MSE of noise estimation after PIC is shown, we can see that bypassing the estimated noise does not yield a better MSE, i.e., σ^2_{in} is not in principal a good estimate of σ^2_{out}. However, since, as explained earlier, γ_{in} is a good estimate of γ_{out} and since the weighting filter vector of the MRC block depends mainly on the noise+ICI inter-channel ratio and not necessarily on the quality of the estimated noise+ICI value, we find a similar BER performance in the case when the noise variance is estimated at the input to the PIC and bypassed to the MRC block, or estimated after the PIC block.

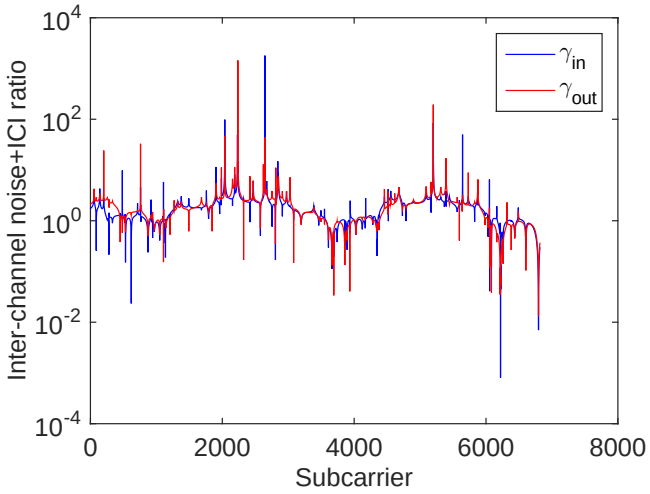

Figure 4.32.: Inter-channel noise+ICI ratio before and after PIC, γ_{in} and γ_{out}, for one OFDM symbol

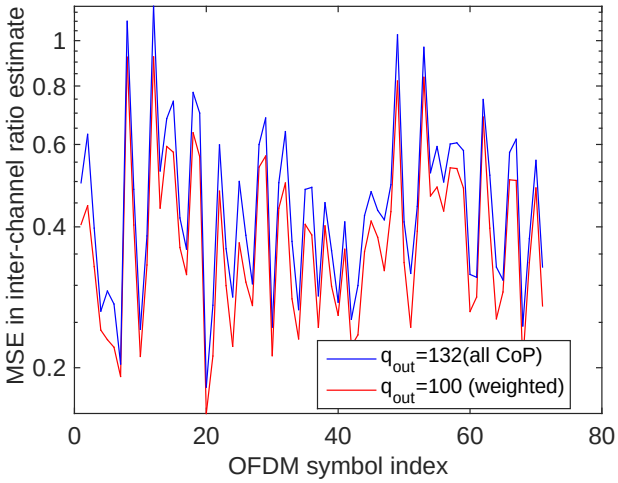

Figure 4.33.: $|\gamma_{out} - \gamma_{GANE}|^2$ for successive OFDM symbols

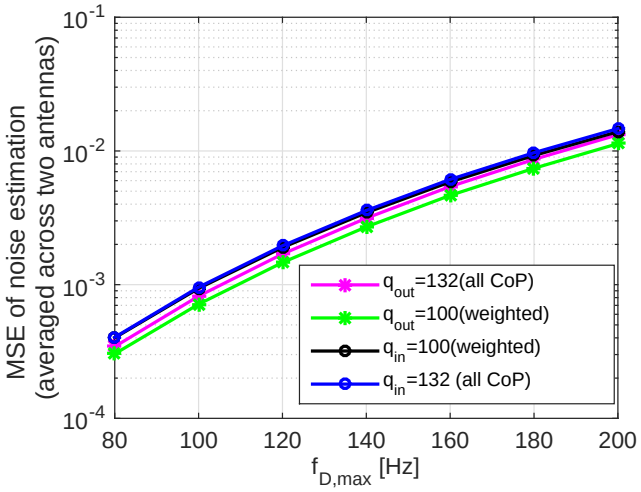

Figure 4.34.: MSE of noise variance estimation PIC→MRC with colored noise estimation after PIC

4.7.3.2. Enhanced MRC→PIC Using Windowed CoP PANE

In Figure 4.35, we can see the Doppler gain provided by applying windowed CoP PANE on the architecture MRC→PIC. We apply windowed CoP PANE (using a noise window size $q = 100$ CoPs plus weighting according to (4.36) and (4.37)) before MRC and after PIC.[2] As we can see, around 13 Hz gain can be achieved by applying windowed CoP PANE before MRC in MRC→PIC (squared magenta curve vs black curve), which is a little bit higher than the gain achieved by applying windowed CoP PANE on the architecture MRC standalone. However, applying windowed CoP PANE after PIC in MRC→PIC can only achieve a marginal gain (squared green curve vs squared magenta curve).

4.7.4. Comparisons

In Figures 4.36 and 4.37, we can see BER comparisons of all the different receiver diversity architectures discussed so far. We do not add the results for MMSE-ICIC→MRC since it overlaps with the results for MRC→MMSE-ICIC, as shown in Figure 4.20. The simulation parameters are listed in Table 4.8. As we can see, using PACE in Figure 4.36, the best performance can be achieved using the architecture SDCC→PIC, which gives a significant Doppler gain of around 95 Hz compared to the classical MRC which does not consider ICI at all. Thus, assuming a carrier frequency of $f_c = 600$ MHz, MRC can handle a receiver moving at a speed of 153 km/h while the architecture SDCC→PIC allows for reception till a speed of 324 km/h.

[2]Note that ICI cancellation using PIC does not require knowledge of noise variance, therefore the way the noise variance computed after MRC does not affect the performance.

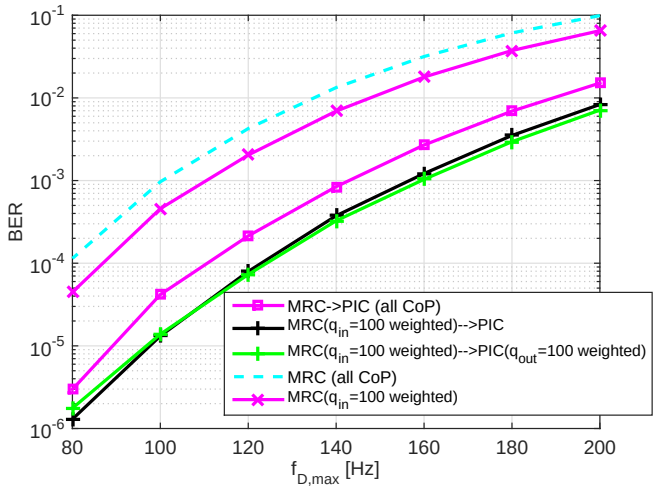

Figure 4.35.: BER of MRC→PIC with colored noise estimation at the input to MRC and after PIC

Applying windowed CoP PANE before MRC gives a gain around $10 - 15$ Hz in the architectures MRC→PIC, PIC→MRC and MRC standalone.

With GACN in Figure 4.37, we can see almost the same relative performance as in Figure 4.36, only in a slightly higher frequency range, which is intuitively satisfying. We can thus conclude that this relative performance observed in Figure 4.36 will still apply using a better channel estimation method than that of linear interpolation used throughout this thesis.

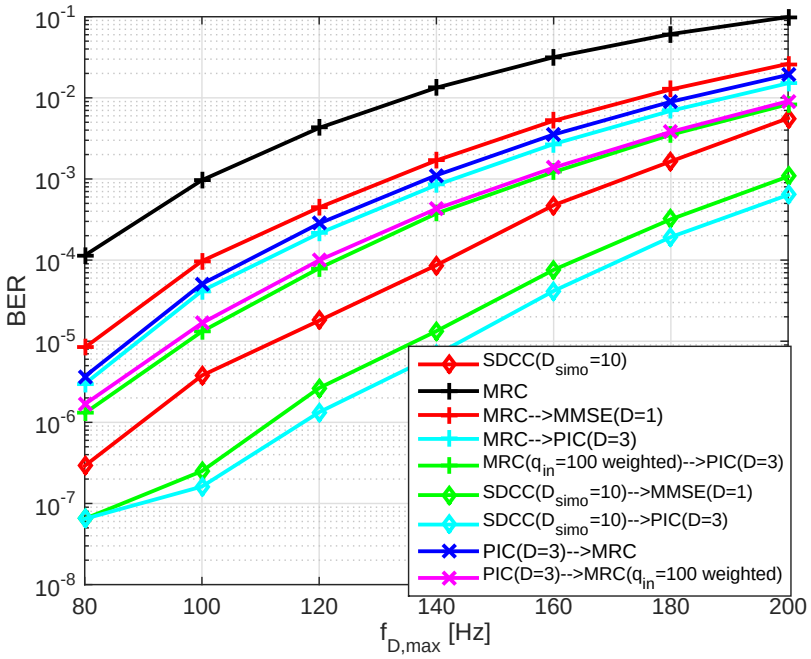

(a) BER vs Doppler frequency range

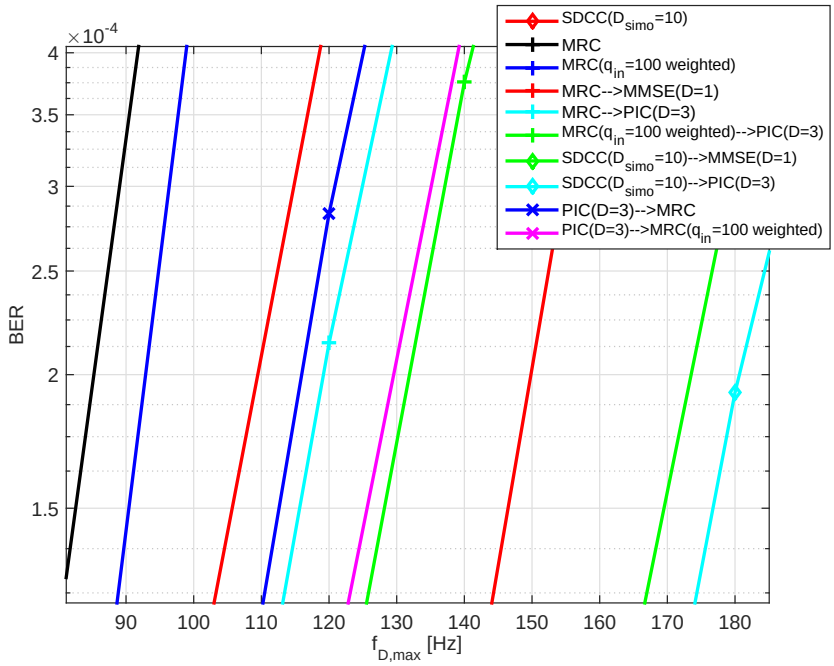

(b) Zoomed BER plot

Figure 4.36.: Comparison of all different architectures using PACE

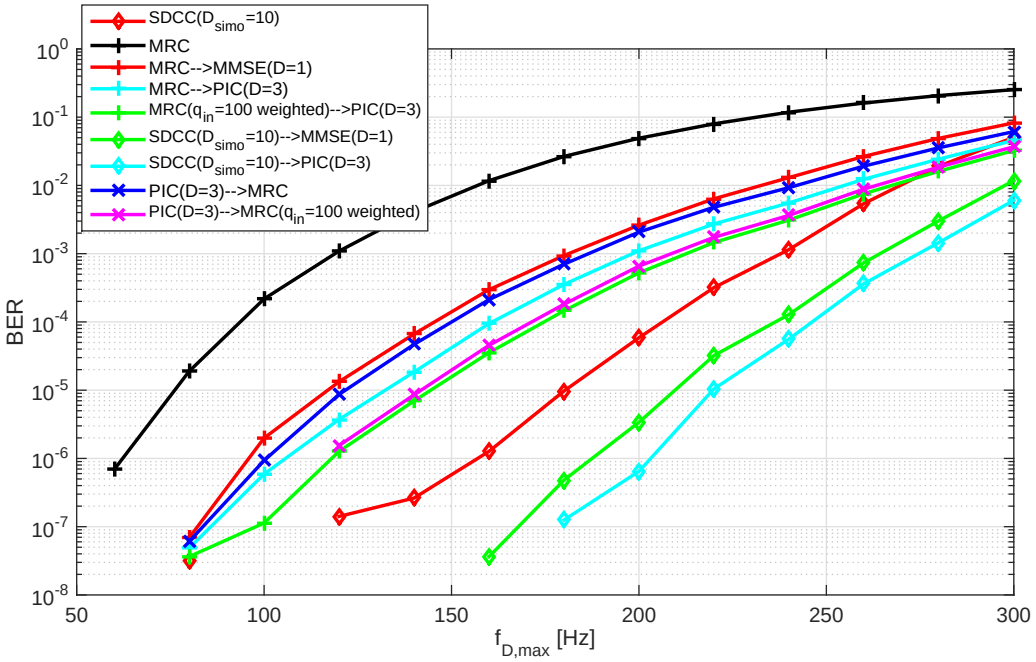

(a) BER vs Doppler frequency range

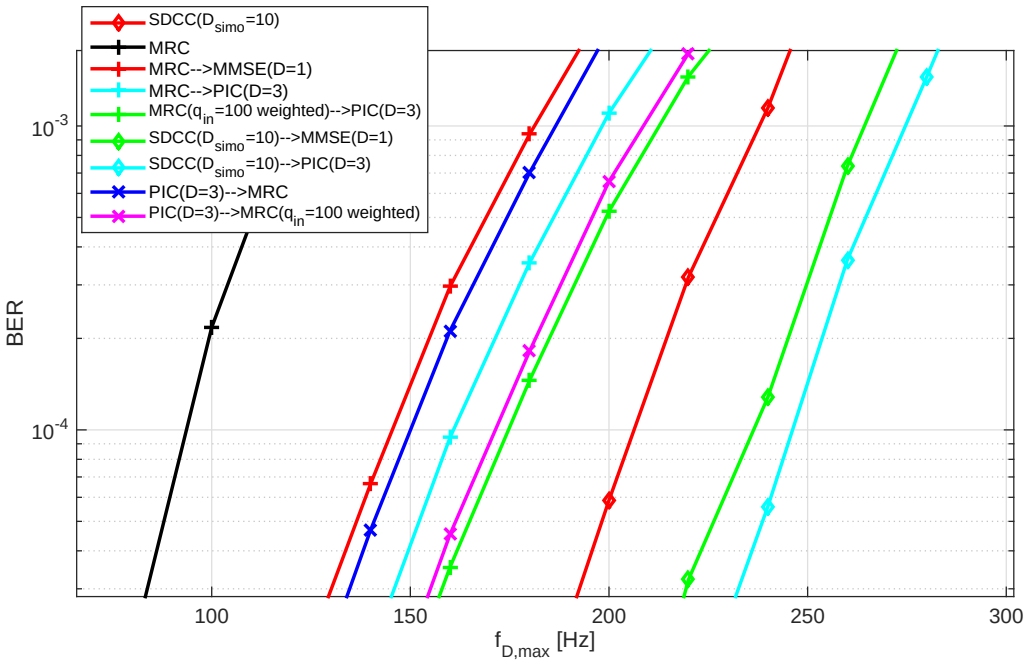

(b) Zoomed BER plot

Figure 4.37.: Comparison of all different architectures using GACN

Parameter	Setting
System	DVB-T
BER	after Viterbi decoding in dependency of Doppler
CSI	PACE using linear interpolation, GACN
noise estimation	PANE after PIC and MMSE, (4.41) after MRC
SNR	30 dB
Modulation	64 QAM
Coding	Viterbi decoding (2/3) traceback depth=252
OFDM	8k FFT , $N_{GI} = 2048$ samples,$N_a = 6817$ subcarriers $N_{data} = 6048$ subcarriers
Channel	2×1 spatially uncorrelated TU6 channels
OFDM Receiver	PIC:$D = 3$. MMSE-ICIC:$D = 1$. OC:$D_{simo} = 10$

Table 4.8.: Simulation Parameters used to produce results in Figures 4.36 and 4.37

5. Blind Maximum Ratio Combining

5.1. Motivation

In Chapter 4, we investigated exploiting the receiver diversity to mitigate the effect of ICI. There exists a huge literature on the issue of receiver diversity combining [SA05, Stu96]. Some approaches require only partial CSI knowledge, e.g, EGC, while others expect full CSI knowledge, e.g, MRC. In the case of spatially uncorrelated channels with AWGN, the highest gain is obtained using MRC. In the absence of interference and assuming equally likely transmitted symbols, the total conditioned SNR per symbol is given as the summation of SNR on all individual antennas [SA05, Stu96]. In Figure 5.1, a block diagram of a conventional receive diversity scheme is shown. The signal $s\,(t)$ is transmitted over M uncorrelated channels $h_m(t,\,\tau)$, $m \in [1, M]$. The received signals $r_m\,(t)$ are combined using knowledge of the CSI acquired at the receiver side using PACE. Therefore as we can see, at each antenna part of the demodulator circuit has to be duplicated to perform standard-dependent operations such as synchronization, pilot extraction and channel estimation. The design of these blocks strongly depends on the communication signal structure, e.g, the synchronization depends on the framing structure, the demodulation is applied differently for single-carrier or multi-carrier signals, the pilot information is embedded depending on the used standard and thus extracted differently, and so on.

In [AES13], we proposed a receiver architecture which has the advantage of being transmit signal independent. Only limited information about the underlying system is required for receive signal combining, therefore such a unit can be employed in almost any standard.

The architecture of the proposed scheme is shown in Figure 5.2. In order to work independently of the underlying standard, blind maximum ratio combining (BMRC) re-

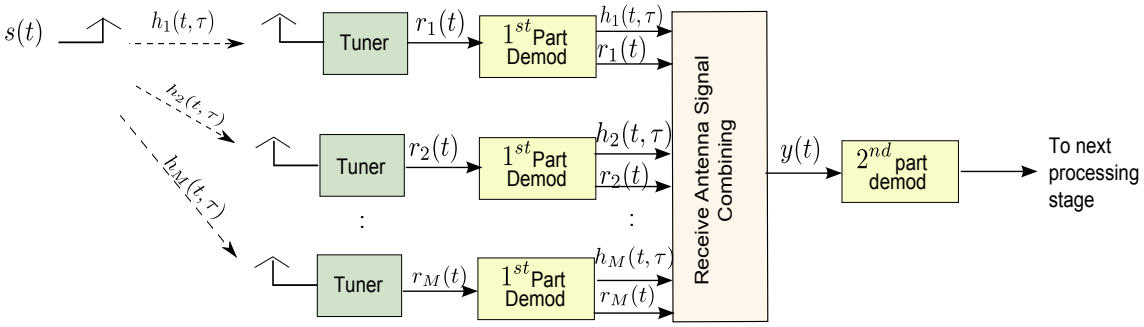

Figure 5.1.: Pilot-assisted signal combining

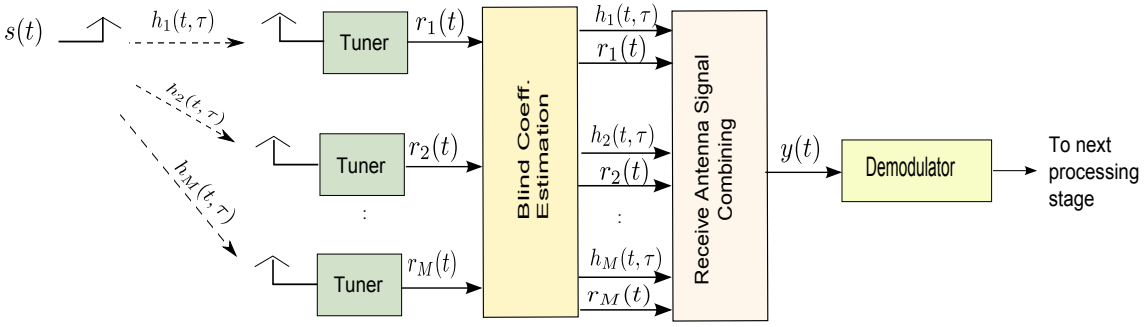

Figure 5.2.: Blind receive antenna signal combining

lies only on the received signals to acquire CSI instead of PACE. To get an estimate of the channel only through the received signals, we propose to use blind channel identification (BCI) [AES13, EAS13]. In section 5.2, the proposed architecture is described. Afterwards, we elaborate on the BCI methods in sections 5.3 and 5.5.

5.2. Blind Maximum Ratio Combining

As we shall see in sections 5.3 and 5.5, BCI is carried out in the time domain. Similarly, blind receiver diversity combining is also done in the time domain. To proceed, we first put down the system model for the time domain received signal vector for an observation window of B samples as

$$\mathbf{r}_m(n) = \mathbf{g}_m(n)\,\mathbf{s}(n) + \mathbf{x}_m(n), \tag{5.1}$$

where $\mathbf{r}_m(n)$ is an $B \times 1$ vector of the received samples at antenna m and time index n. $\mathbf{g}_m(n)$ is the time domain Toeplitz channel matrix of size $B \times B + L - 1$. $\mathbf{s}(n)$ is an $B + L - 1 \times 1$ vector of sent samples and $\mathbf{x}_m(n)$ is the vector of noise samples at antenna m and time index n. Assuming an observation window of size $B = 5$ samples and an FIR channel transfer function of order 2 ($L = 3$), the received vector $\mathbf{r}_m(n)$ can be written as

$$\begin{bmatrix} r_m(n) \\ r_m(n-1) \\ r_m(n-2) \\ r_m(n-3) \\ r_m(n-4) \end{bmatrix} = \begin{bmatrix} h_m(n,0) & h_m(n,1) & h_m(n,2) & 0 & 0 & 0 & 0 \\ 0 & h_m(n,0) & h_m(n,1) & h_m(n,2) & 0 & 0 & 0 \\ 0 & 0 & h_m(n,0) & h_m(n,1) & h_m(n,2) & 0 & 0 \\ 0 & 0 & 0 & h_m(n,0) & h_m(n,1) & h_m(n,2) & 0 \\ 0 & 0 & 0 & 0 & h_m(n,0) & h_m(n,1) & h_m(n,2) \end{bmatrix} \begin{bmatrix} s(n) \\ s(n-1) \\ s(n-2) \\ s(n-3) \\ s(n-4) \\ s(n-5) \\ s(n-6) \end{bmatrix} + \begin{bmatrix} x_m(n) \\ x_m(n-1) \\ x_m(n-2) \\ x_m(n-3) \\ x_m(n-4) \end{bmatrix}. \tag{5.2}$$

where the channel is assumed constant over the whole block in (5.2), i.e., $h_m(n,\, l) \approx h_m(n-1,\, l) \approx ... \approx h_m(n-B,\, l)$. At a receiver equipped with M antennas, the concatenated received vector from all antennas can be written as

$$\begin{aligned} \check{\mathbf{r}}(n) &= \begin{bmatrix} \mathbf{r}_1(n) \\ \vdots \\ \mathbf{r}_M(n) \end{bmatrix}_{(MB\times 1)} \\ &= \check{\mathbf{g}}(n)\,\mathbf{s}(n) + \bar{\mathbf{x}}(n), \end{aligned} \tag{5.3}$$

where the concatenated channel matrix $\check{\mathbf{g}}(n)$ can be written as

$$\check{\mathbf{g}}(n) = \begin{bmatrix} \mathbf{g}_1(n) \\ \vdots \\ \mathbf{g}_M(n) \end{bmatrix}_{(MB\times B+L-1)} \tag{5.4}$$

There is a fundamental difference between the models in (5.1) and (5.3), as the channel matrix is no longer a "fat" or a landscape matrix. If $M > 1$ and $B > L-1$, $\check{\mathbf{g}}(n)$ is a "tall" or a seascape matrix, i.e., the linear model in (5.3) is an overdetermined system and therefore the signal vector s can be exactly recovered. It is also clear that the longer the observation window B or the higher the number of antennas M, the more equations are available in the system and thus a better estimate can be obtained for the signal vector $\mathbf{s}$ in an AWGN environment. This confirms our observation that linear equalization is indeed enough in a SIMO system. For more information, the interested reader can refer to [PS08].

Performing an least squares (LS) criteria on (5.3) yields

$$\begin{aligned} \hat{\mathbf{s}}(n) &= \check{\mathbf{g}}^{\dagger}(n)\,\check{\mathbf{r}}(n) \\ &= \left(\check{\mathbf{g}}^{H}(n)\,\check{\mathbf{g}}(n)\right)^{-1} \underbrace{\check{\mathbf{g}}^{H}(n)\,\check{\mathbf{r}}(n)}. \end{aligned} \tag{5.5}$$

If we examine the underlined part of (5.5), we can write it down as

$$\check{\mathbf{g}}^H(n)\,\check{\mathbf{r}}(n) = \sum_{m=1}^{M} \underbrace{\mathbf{g}_m^H(n)\,\mathbf{r}_m(n)}_{h_m^*(n,-l)\star_l r_m(n)}, \tag{5.6}$$

which can also be seen as a convolution between each received signal at time index n, i.e, $r_m(n)$ and the corresponding matched filter of this particular antenna, i.e., $h_m^*(n,-l)$ over the dimension l. This is also the original definition of a receiver that applies MRC in the time domain [SA05]. Therefore, as seen in Figure 5.3, we perform MRC in time domain using matched filters.

The distortion introduced by the channel and later by the diversity combiner (bank of matched filters) can then be removed in the second part of the demodulator. A disadvantage of time domain combining is that the distortion introduced by the matched filters will result in an effective channel impulse response with double the actual channel length. In case the receiver is using a time domain equalizer, this will complicate the receiver architecture. However, in case of OFDM frequency domain equalization, as long as the effective channel length does not exceed the guard interval, the equalization process remains uncomplicated.

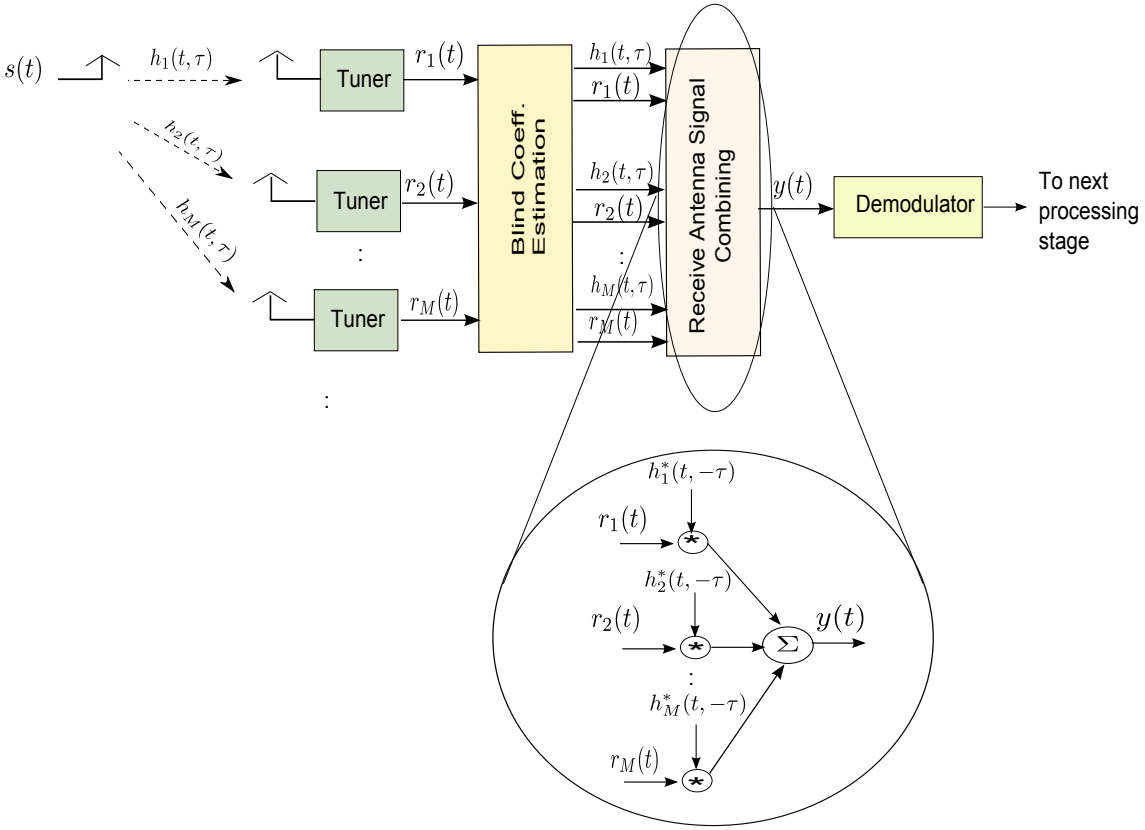

Figure 5.3.: Blind receive antenna signal combining using matched filters

5.3. Blind Channel Identification

Blind deconvolution algorithms can be classified into [Hay00]

1. Algorithms based on higher order statistics (HOS)
2. Algorithms based on second order statistics (SOS)

Algorithms based on HOS, include for example the famous constant modulus algorithm (CMA) [God80] or algorithms based on higher order cumulants [Hay00]. The main disadvantage of relying on higher order statistics is their slow rate of convergence, which makes them unsuitable to identify a time-varying channel. Hence, we shall not consider this family of algorithms in our investigations.

Algorithms based on SOS were first proposed in [TXK91], where oversampling at the receiver side is used to create the temporal diversity needed for the algorithm to converge. Similarly, in [HLT94] an SOS algorithm based on LS solution is used to blindly identify a SIMO channel. The approach makes use of the cross relations between the outputs of the antennas. Hence, it acquired the name cross relations (CR). To explain the idea behind the CR, we refer to Figure 5.4, where two antennas are placed at the receiver side to obtain two received signals r_m and $r_{m'}$. In the absence of noise, the received signals can be written as

$$\begin{aligned} r_m &= h_m \star s \\ r_{m'} &= h_{m'} \star s, \end{aligned} \tag{5.7}$$

where h_m and $h_{m'}$ are the communication channels between the transmit antenna and the receive antennas m and $m^{'}$ and s is the sent signal.

The idea of cross relations is based on the observation that

$$r_{m'} \star h_m = r_m \star h_{m'}. \tag{5.8}$$

Therefore, based only on the received signals r_m and $r_{m'}$, the CR approach tries to find the signals h_m and $h_{m'}$ which would make (5.8) satisfied. In this search, only the received signals r_m and $r_{m'}$ are used, thus it is a blind approach. This estimate can only be obtained up to a scalar ambiguity which can be explained by the fact that (5.8) is

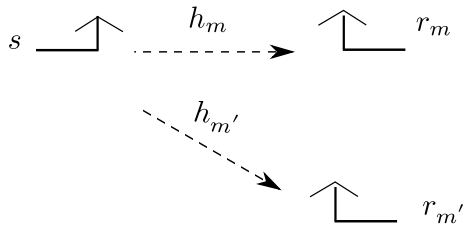

Figure 5.4.: SIMO model with 2 antennas

still satisfied even if both sides are multiplied by an arbitrary complex scalar factor. In [GXK95, TXK91], a least squares solution was first proposed to solve the problem of CR.

In [MDM95], the authors introduced a subspace approach inspired from a direction of arrival (DOA) estimation algorithm, namely the multiple signal classification (MUSIC) algorithm. In [Hua96], a two step maximum likelihood (ML) solution is designed for the problem of CR. The interested reader can refer to [Sal11], for more information on SOS based identification methods. Although all the aforementioned batch solutions can achieve very good performance, they all require very high complexity since they include eigenvalue decomposition (EVD) or singular value decomposition (SVD) steps which require high complexity. In this work, seeking a low complex solution, we are interested in a frequency domain iterative implementation of the CR approach, namely the MCFLMS solution proposed in [HB03, HBC03].

5.3.1. Multi-Channel Frequency Least Mean Squares

To explain the MCFLMS algorithm we first introduce the iterative vector form of (5.8) at time index n

$$\mathbf{r}_{m'}^{T}(n)\,\mathbf{h}_m = \mathbf{r}_{m}^{T}(n)\,\mathbf{h}_{m'}, \tag{5.9}$$

where $\mathbf{r}_{m'}(n)$ and $\mathbf{h}_m$ can be defined as

$$\mathbf{r}_{m'}(n) = \begin{bmatrix} r_{m'}(n) \\ \vdots \\ r_{m'}(n-L+1) \end{bmatrix} \tag{5.10}$$

and

$$\mathbf{h}_m = \begin{bmatrix} h_m(0) \\ \vdots \\ h_m(L-1) \end{bmatrix}. \tag{5.11}$$

A CR error signal can be defined as

$$e_{mm'}(n) = \mathbf{r}_{m'}^{T}(n)\,\mathbf{h}_m - \mathbf{r}_{m}^{T}(n)\,\mathbf{h}_{m'}, \tag{5.12}$$

where $m, m^{'} \in \{1, 2, ...M\}\ \forall m \neq m^{'}$. Accordingly, a cost function can be defined as the summation of the squared CR error among all M antennas

$$j_{CR}(n) = \sum_{m=1}^{M-1} \sum_{m'=m+1}^{M} \left| e_{mm'}(n) \right|^2. \tag{5.13}$$

The problem can then be formulated as

$$\check{\hat{\mathbf{h}}} = arg \min_{\hat{\mathbf{h}}} E\left\{ j_{CR}(n) \right\}, \tag{5.14}$$

under the constraint $\left\|\check{\hat{\mathbf{h}}}\right\| = 1$.

The stacked channel impulse response, $\check{\hat{\mathbf{h}}}$, can be written as $\check{\hat{\mathbf{h}}} = \left[\begin{array}{ccc} \hat{\mathbf{h}}_1^T & \dots & \hat{\mathbf{h}}_M^T \end{array}\right]^T$. As mentioned earlier, because of the scalar ambiguity, the output of such an optimization is usually a scalar multiple of the actual channel impulse response. Therefore, the output of the optimization should be normalized such that $\left\|\check{\hat{\mathbf{h}}}\right\| = 1$, to avoid excessively large scalar ambiguity factors.

In [HB02], the authors proposed to use the least mean square (LMS) algorithm to solve the optimization problem in (5.14), namely multi-channel least mean squares (MCLMS). In [HB03, HBC03], the authors proposed using frequency domain block adaptive filtering to solve the same problem. This approach has the advantage of requiring significantly less computational complexity than the time domain solution, [Hay01].

In this work, we focus only on the frequency domain solution, namely the MCFLMS algorithm. MCFLMS operates in block-wise mode, i.e., one iteration includes processing a block of B samples. The CR error in the frequency domain can be written as

$$\mathbf{E}_{mm'}^u = \mathbf{W}_{(B\times 2B)}^{01}\left(\mathbf{D}_m^u \mathbf{W}_{(2B\times B)}^{10}\hat{\mathbf{H}}_{m'} - \mathbf{D}_{m'}^u \mathbf{W}_{(2B\times B)}^{10}\hat{\mathbf{H}}_m\right), \tag{5.15}$$

where $\mathbf{D}_m^u$ is a diagonal matrix of size $2B \times 2B$ composed of the FFT of the buffered $2B$ received samples on antenna m

$$\mathbf{D}_m^u = \text{diag}\left\{\mathbf{F}_{2B}\left[\begin{array}{c} r_m\left(uB - B\right) \\ \vdots \\ r_m\left(uB + B - 1\right) \end{array}\right]\right\}, \tag{5.16}$$

where the FFT matrix $\mathbf{F}_{2B}$ is as defined in (3.11). The frequency domain masks $\mathbf{W}_{(B\times 2B)}^{01}$ and $\mathbf{W}_{(2B\times B)}^{10}$ are used to emulate the overlap-save technique and are defined as

$$\mathbf{W}_{(B\times 2B)}^{01} = \mathbf{F}_B \left[\begin{array}{cc} \mathbf{0}_B & \mathbf{I}_B \end{array}\right] \mathbf{F}_{2B}^{-1}, \tag{5.17}$$

$$\mathbf{W}_{(2B\times B)}^{10} = \mathbf{F}_{2B}\left[\begin{array}{c} \mathbf{I}_B \\ \mathbf{0_B} \end{array}\right] \mathbf{F}_B^{-1}. \tag{5.18}$$

Similar to (5.13), a cost function can be computed in the frequency domain as

$$J_{CR}^u = \sum_{m=1}^{M-1}\sum_{m'=m+1}^{M} ||\mathbf{E}_{mm'}^u||^2. \tag{5.19}$$

The frequency domain gradient of the cost function with respect to the m^{th} subchannel and the u^{th} iteration of the algorithm is computed as

$$\nabla_m J_{CR}^u = \frac{\partial J_{CR}^u}{\partial \hat{\mathbf{H}}_m^*} = \sum_{m'=1, m'\neq m}^{M-1}\left(\mathbf{W}_{(B\times 2B)}^{01}\mathbf{D}_{m'}^u \mathbf{W}_{(2B\times B)}^{10}\right)^H \mathbf{E}_{m'm}^u \tag{5.20}$$

The update equation of the estimate of the m^{th} subchannel is then written as

$$\begin{aligned}\hat{\mathbf{H}}_m^u &= \hat{\mathbf{H}}_m^{u-1} - \mu \nabla_m J_{CR}^u \\ &= \hat{\mathbf{H}}_m^{u-1} - \mu \mathbf{W}_{(B\times 2B)}^{10} \sum_{m'=1, m'\neq m}^{M} \mathbf{D}_{m'}^{u*} \mathbf{W}_{(2B\times B)}^{01} \mathbf{E}_{m'm}^{u},\end{aligned} \tag{5.21}$$

where μ is the step size parameter and the frequency domain masks $\mathbf{W}_{B\times 2B}^{10}$ and $\mathbf{W}_{2B\times B}^{01}$ are defined as

$$\mathbf{W}_{(B\times 2B)}^{10} = \mathbf{F}_B \left[\begin{array}{cc} \mathbf{I}_B & \mathbf{0}_B \end{array} \right] \mathbf{F}_{2B}^{-1} = \left(\mathbf{W}_{(2B\times B)}^{10} \right)^H, \tag{5.22}$$

$$\mathbf{W}_{(2B\times B)}^{01} = \mathbf{F}_{2B} \left[\begin{array}{c} \mathbf{0_B} \\ \mathbf{I}_B \end{array} \right] \mathbf{F}_B^{-1} = \left(\mathbf{W}_{(B\times 2B)}^{01} \right)^H. \tag{5.23}$$

The estimate of the m^{th} subchannel is then computed as

$$\hat{\mathbf{H}}_m^u = \hat{\mathbf{H}}_m^{u-1} - \mu \mathbf{W}_{(B\times 2B)}^{10} \sum_{m'=1}^{M} \mathbf{D}_{m'}^{u*} \mathbf{W}_{(2B\times B)}^{01} \mathbf{E}_{m'm}^{u}. \tag{5.24}$$

After every estimation step u, the estimated channel has to be further normalized such that $\left\| \overset{\circ}{\hat{\mathbf{H}}}^u \right\| = \left\| \left[\begin{array}{c} \hat{\mathbf{H}}_1^u \\ \vdots \\ \hat{\mathbf{H}}_M^u \end{array} \right] \right\| = 1$.

In general, there are two identifiability conditions associated with this problem [GXK95], i.e., conditions on the signal sent and the channel in order for the channel impulse response to be identifiable

1. The channels have to be co-prime, i.e., no common zeros. This requirement is clear if we rewrite (5.8) in the Z domain

$$R_{m'}(z) H_m(z) = R_m(z) H_{m'}(z). \tag{5.25}$$

As we can see, in case the two channels $H_m(z)$ and $H_{m'}(z)$ share a common zero such that $H_m(z) = H_m^{'}(z)(z - z_s)$ and $H_{m'}(z) = H_{m'}^{'}(z)(z - z_s)$. If we substitute the formulas back in (5.25), we find that the shared zeros cancel each other and hence any arbitrary zero can also satisfy the equation in (5.25). Therefore, this particular zero can not be identified. A similar case arises in case the channel order is overestimated, i.e., the number of zeros is overestimated. For example, if the actual channel length L is overestimated by $L^{'} > L$, an arbitrary polynomial of degree $L^{'} - L$ multiplied by both sides of (5.25) will still make the equation satisfied. That is why channel order overestimation is regarded as a common challenge in this problem [dCS04].

2. The second requirement is concerned with the source signal, where the source signal has to have enough excitation modes to cover the whole transmission bandwidth. This is a typical requirement in system identification problems. Mathematically, it is equivalent to the auto-correlation matrix of the transmit signal $\mathbf{R}_{ss}$ being of full rank.

In reality, these conditions are not always satisfied, which threats the convergence of the algorithm. In section 5.5, we shall explain some enhancements added to the algorithm to guarantee a stable and accurate performance.

5.4. Assessment Criteria

As mentioned earlier, the problem of BCI based on the principal of CR has an inherent ambiguity. In [MBS98], the authors discuss the philosophy of evaluating estimated impulse responses for applications in which the overall scaling or gain is irrelevant such as blind identification algorithms. In this work we use normalized root projection mean squared error (NRPMSE) criteria to evaluate the performance of the BCI algorithm. This error measure reflects that we are only able to estimate $\mathbf{h}$ up to an arbitrary scalar factor, assuming correct knowledge of channel length. In general, the BCI estimate can be put in this form

$$\alpha(n)\,\check{\hat{\mathbf{h}}}(n) = \check{\mathbf{h}}(n) + \mathbf{x}_{est} \tag{5.26}$$

We are interested in assessing the noise power of $\mathbf{x}_{est}$ relative to the channel power. Therefore, the scalar ambiguity is derived as

$$\hat{\alpha}(n) = \frac{\check{\hat{\mathbf{h}}}^H(n)\,\check{\mathbf{h}}(n)}{\check{\hat{\mathbf{h}}}^H(n)\,\check{\hat{\mathbf{h}}}(n)} \tag{5.27}$$

The NRPMSE can be derived as

$$||\check{\mathbf{h}} - \frac{\check{\hat{\mathbf{h}}}^H(n)\,\check{\mathbf{h}}(n)}{\check{\hat{\mathbf{h}}}^H(n)\,\check{\hat{\mathbf{h}}}(n)}\check{\hat{\mathbf{h}}}(n)\,||^2 \tag{5.28}$$

The NRPMSE can also be equivalently derived using the frequency domain variables, i.e., $\check{\hat{\mathbf{H}}}^u$ and $\check{\hat{\mathbf{H}}}$.

In [EAS13], a new criteria is proposed to assess how good the estimate for the combining process is. In our system, we use the blind estimate only in the combining stage. The rest of the equalization should be handled by the standard dependent equalizer. In other words, our idea of a "good" channel estimate is much wider than the classical case. For example, in case of channel order overestimation, the NRPMSE can diverge due to the additional ambiguity of a possible delay time, that is common for all channel estimates $\hat{\mathbf{h}}(n,l)$. Furthermore, a common delay of all channel estimates has no influence on the combining performance. For this purpose, a new assessment criterion is proposed, that measures the average SNR loss of BMRC compared to perfect MRC. First, we define the

output SNR after combining the received signals with $\hat{\mathbf{h}}(n)$ according to MRC assuming AWGN with zero mean and same variance for all receive antennas. For convenience, we compute the output SNR in the frequency domain. After MRC, the combined signal is

$$\hat{S}(k) = \check{\hat{\mathbf{H}}}^H(k)\,\check{\hat{\mathbf{H}}}(k)\,S(k) + \check{\hat{\mathbf{H}}}^H(k)\,\check{\mathbf{X}}(k) \tag{5.29}$$

$$\begin{aligned}\Gamma_{out}\left(\check{\hat{\mathbf{H}}}^u\right) &= \sum_{k=0}^{B-1} \frac{\check{\hat{\mathbf{H}}}^{\hat{u}H}(k)\,\check{\mathbf{H}}(k)\,E\left\{|S(k)|^2\right\}\check{\mathbf{H}}^H(k)\,\check{\hat{\mathbf{H}}}^{\hat{u}}(k)}{\check{\hat{\mathbf{H}}}^{\hat{u}H}(k)\,E\left\{\check{\mathbf{X}}(k)\,\check{\mathbf{X}}^H(k)\right\}\check{\hat{\mathbf{H}}}^{\hat{u}}(k)} \\ &= \sum_{k=0}^{B-1} \frac{\check{\hat{\mathbf{H}}}^{\hat{u}H}(k)\,\check{\mathbf{H}}(k)\,\check{\mathbf{H}}^H(k)\,\check{\hat{\mathbf{H}}}^{\hat{u}}(k)}{\sigma^2\left\|\check{\hat{\mathbf{H}}}^{\hat{u}}(k)\right\|^2},\end{aligned} \tag{5.30}$$

where $\check{\hat{\mathbf{H}}}^{\hat{u}}(k)$ contains the estimated channels from all M antennas at the k^{th} frequency bin and u^{th} block index. The last step assumes unit energy symbols, $E\left\{|S(k)|^2\right\} = E_S = 1$ as discussed in the beginning of Chapter 3.

The output SNR loss can then be computed as

$$\Gamma_{loss}\left(\check{\hat{\mathbf{H}}}^{\hat{u}}\right) = \frac{\Gamma_{out}\left(\check{\hat{\mathbf{H}}}^{\hat{u}}\right)}{\Gamma_{out}\left(\check{\mathbf{H}}\right)} \tag{5.31}$$

Note that in the division step the noise variance σ^2 present in (5.30) will disappear in (5.31), and thus $\Gamma_{loss}\left(\check{\hat{\mathbf{H}}}^{\hat{u}}\right)$ measures only how far the estimate $\check{\hat{\mathbf{H}}}^{\hat{u}}$ from the actual channel estimate $\check{\mathbf{H}}$ is.

5.5. Enhanced Multi-Channel Frequency Least Mean Squares

In this section, we describe several enhancements applied to the MCFLMS proposed in [HB03, HBC03] to make it more suitable for tracking time-varying communication channels.

5.5.1. Adaptive Step Size

In the update equation of MCFLMS in (5.24), a static step size parameter μ is used. The choice of μ greatly affects the convergence behavior of the algorithm. An excessively large value of μ can lead to divergence, whereas if μ is chosen to be too small very slow convergence is encountered, which might be too slow to track a time-varying channel. In [GHN06, HBC05], a variable step size MCLMS approach is presented. The idea is further generalized to be applied in the MCFLMS in [HH07]. In these publications, the idea is to adapt the step size so that the distance between $\alpha\hat{\mathbf{H}}_m^{u+1}$, where α is the scalar ambiguity factor defined in (5.26), and the actual channel $\mathbf{H}_m$ is minimum at each iteration. A cost function is defined as

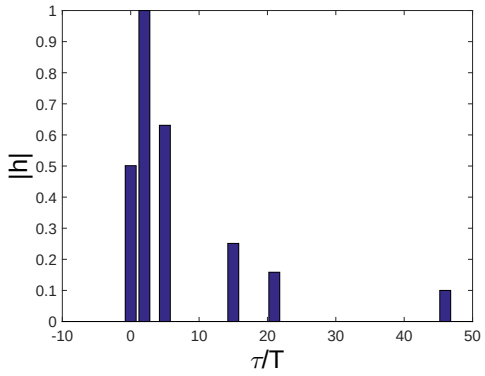

Figure 5.5.: Power delay profile in dB of the TU6 channel

$$J_{\mu}^{u} = \left(\mathbf{H}_m - \alpha\hat{\mathbf{H}}_m^{u+1}\right)^H \left(\mathbf{H}_m - \alpha\hat{\mathbf{H}}_m^{u+1}\right). \tag{5.32}$$

In a second step, the step size is optimized by setting

$$\frac{\partial J_{\mu}^{u}}{\partial \mu^{u}} = 0. \tag{5.33}$$

This optimization results in the variable step size formula [HH07]

$$\mu^{u} = \frac{\check{\hat{\mathbf{H}}}^{\hat{u}H}}{||\nabla J_{CR}^{u}||^2} \nabla J_{CR}^{u} \tag{5.34}$$

where $\nabla J_{CR}^{u} = \begin{bmatrix} \nabla J_{CR,1} \\ \vdots \\ \nabla J_{CR,M} \end{bmatrix}$.

5.5.2. Sparse Cross Relations

Especially at high data rates, many of the encountered communication channels are typically sparse. This means that these channels span a large delay in which only few taps are significant in amplitude. As an example, the TU6 channel shown in Figure 5.5 spans a delay of 46 samples, using the sampling time of a DVB-T signal in an 8 MHz channel bandwidth, but only 6 of those taps are active.

In [AEBAML11, AEBAM08], the sparseness of the communication channel is exploited inside the MCFLMS estimation for better performance. The sparseness of the communication channel can be measured using the l_1 norm

$$||\check{\mathbf{h}}||_1 = \sum_{l=0}^{L-1} |h\,(l)\,|, \tag{5.35}$$

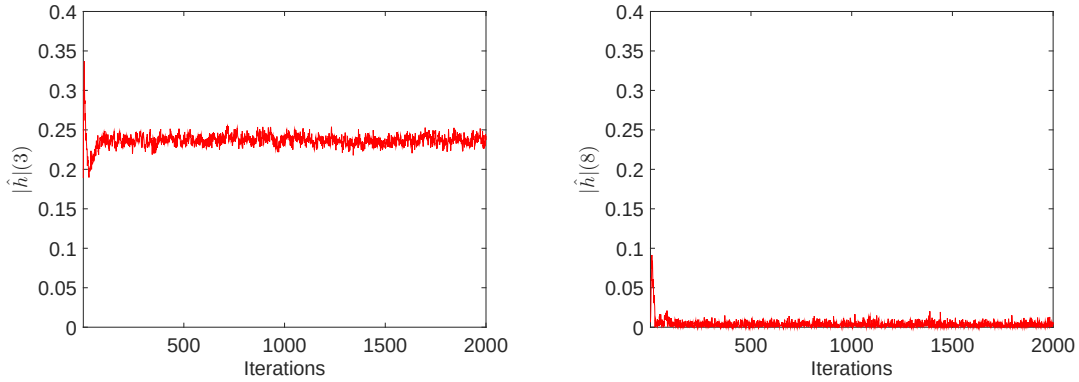

(a) Significant Tap (b) Non-significant tap

Figure 5.6.: Amplitude values of the estimated MCFLMS channel taps at SNR = 10 dB, $f_{D,max} = 0\,\text{Hz}$ and $N = 512$ samples

where as the sparseness of a channel increases, the l_1 norm value decreases assuming a constant channel power value. The idea adopted in [AEBAML11, AEBAM08] is to add a penalty cost function to the cross relation cost function in (5.13) as follows

$$j_{SCR}(n) = j_{CR}(n) + \lambda_s ||\check{\mathbf{h}}||_1, \tag{5.36}$$

such that the algorithm is forced to look for the most sparse solution. The modified update equation is then [AEBAML11, AEBAM08]

$$\hat{\mathbf{h}}_i(n) = \hat{\mathbf{h}}_i(n-1) - \mu \nabla j_{CR} - \lambda_s \dot{\mathbf{h}}(n) \tag{5.37}$$

where $\dot{\mathbf{h}}(n)$ is the derivative of the l_1 norm and can be computed as

$$\dot{h}(l) = sign(h(l))\, l = 0, ..., M(L-1). \tag{5.38}$$

5.5.3. Channel Tap Masking

As mentioned in section 5.5.2, exploiting the sparseness of the communication channel can significantly enhance the tracking capability of the MCFLMS algorithm. For example, in Figure 5.5, we can see that prior knowledge of the location of the 6 significant taps can significantly help reduce the estimation noise, since most of the taps are inactive. The problem is that such an information is not readily available at the receiver side. In [EAS13], a heuristic approach is proposed to identify those significant taps in a first step and create a mask to suppress the estimation noise at the locations of the non-significant taps in a second step.

In Figure 5.6, we can see how the amplitude of the estimated channel varies over time for a significant (left) and a non-significant tap (right). As we can see, the non-significant tap has a much smaller estimated magnitude. To distinguish a significant tap, one idea

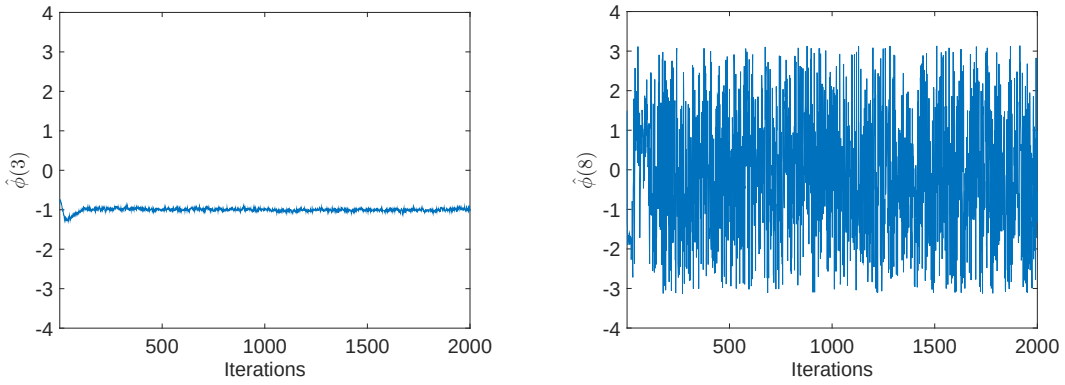

(a) Significant Tap (b) Non-significant tap

Figure 5.7.: Estimated phase information of the estimated MCFLMS channel impulse response taps at SNR $= 10\,\text{dB}$, $f_{D,max} = 0\,\text{Hz}$ and $N = 512$ samples

would be to set a threshold based on the magnitude value of the estimated tap. The problem with such an approach is that the choice of the threshold will be very sensitive to the SNR and the choice of the step size.

However, by looking at Figure 5.7, we can see another feature by which we can distinguish significant and non-significant taps. Namely, the phase information, more precisely, the temporal variation in the phase information. As we can see in Figure 5.8b, where the variations in phase and amplitude values of the estimated MCFLMS channel impulse response taps are displayed, the phase information of the non-significant taps exhibits large non-monotonous changes compared to the variations recorded for a significant channel tap. On the locations of the non-significant taps, the algorithm is tracking the phase of the AWGN noise component, i.e., an uncorrelated random variable which is uniformly distributed over the range $[-\pi, \pi]$, hence the very fast change in the estimated phase at these locations.

In [EAS13], we propose to monitor the average magnitude of these phase variations as a way to distinguish the significant taps from the non-significant ones. A channel tap mask is built based on comparing these values to a predetermined threshold. The masking operation, carried out in each MCFLMS iteration, is summarized in the following steps:

1. at the u^{th} iteration of the algorithm, compute the phase difference $\Delta\phi^u(l)$ for the l^{th} tap as
$$\Delta\phi_m^u(l) = \angle\hat{h}_m^u(l) - \angle\hat{h}_m^{u-1}(l) \tag{5.39}$$

2. compute a time moving exponential average change value $\Delta\bar{\phi}_m^u(l)$ as
$$\Delta\bar{\phi}_m^u(l) = \lambda_{mask}\Delta\bar{\phi}_m^{u-1}(l) + (1-\lambda_{mask})\,|\Delta\phi_m^u(l)\,| \tag{5.40}$$
where λ_{mask} is the forgetting factor parameter of the averaging process, $\lambda_{mask} \in]0, 1]$.

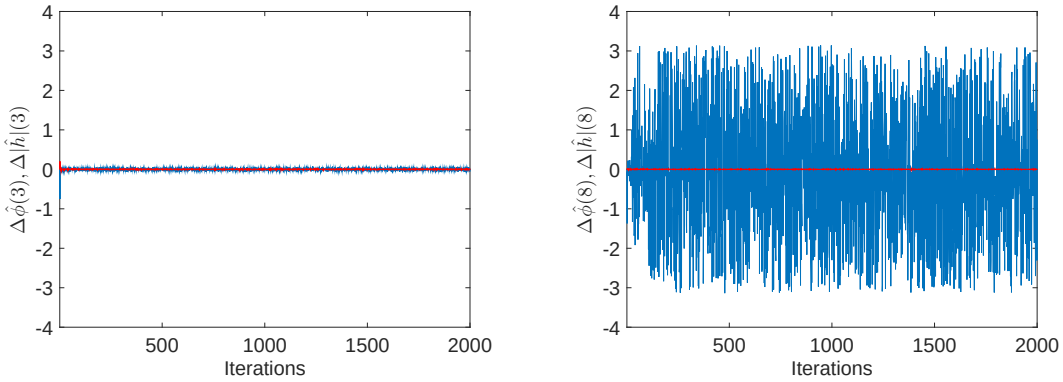

(a) Significant tap

(b) Non-significant tap

Figure 5.8.: Variations in phase (blue line) and amplitude (red line) values of the estimated MCFLMS channel impulse response taps at SNR = 10 dB, $f_{D,max}$ = 0 Hz and $N = 512$ samples

3. compare $\Delta\bar{\phi}_m^u(l)$ to a predetermined threshold k_ϕ. If $\Delta\bar{\phi}_m^u(l) > k_\phi$, the l^{th} tap is judged as a non-significant tap and is then set to zero. The resulting impulse response is used for the next iteration step.

After every iteration step, the mask is re-calculated such that if a new echo appears in the channel impulse response which was previously regarded as a non-significant tap, the algorithm is able to detect the new significant channel tap relying on the average phase difference.

In Figures 5.9 and 5.10, zoomed-in plots on the SNR after MRC are shown for the cases of no blind coefficient masking, with blind coefficient masking, genie-aided coefficient masking and perfect CSI respectively. Comparing Figure 5.9a and 5.9b, we can observe the enhancement brought by the blind coefficient masking, where it significantly smoothed out the response and resulted in higher SNR. No significant degradation can be found in Figure 5.9b compared to Figure 5.10, which proves that the proposed methodology explained above to distinguish the significant taps from the non-significant taps is successful.

5.5.4. Out-of-band Noise Reduction

It is common for communication signals to have null bands in the frequency domain to follow some restrictions on a spectral mask. For example, in DVB-T and DVB-T2, out of the N subcarriers, only N_a subcarriers carry information and the rest are set to zero as explained in section 2.3.1. Such a signal structure violates the second identifiability condition mentioned in section 5.3.1, namely the fact that the sent signal does not excite the whole bandwidth. As an example, we refer to Figure 5.11 where the sent signal in green excites only half of the transmission bandwidth. In the null bands, although CSI

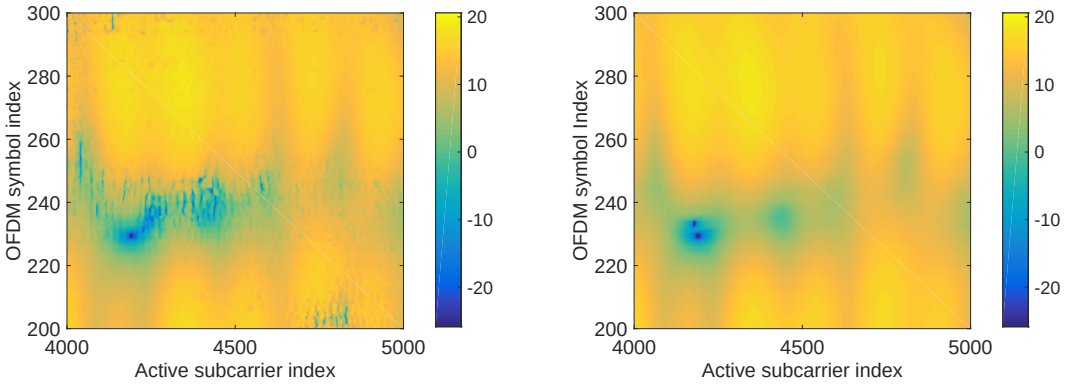

(a) No coefficient masking (b) With coefficient masking

Figure 5.9.: Output SNR after combining

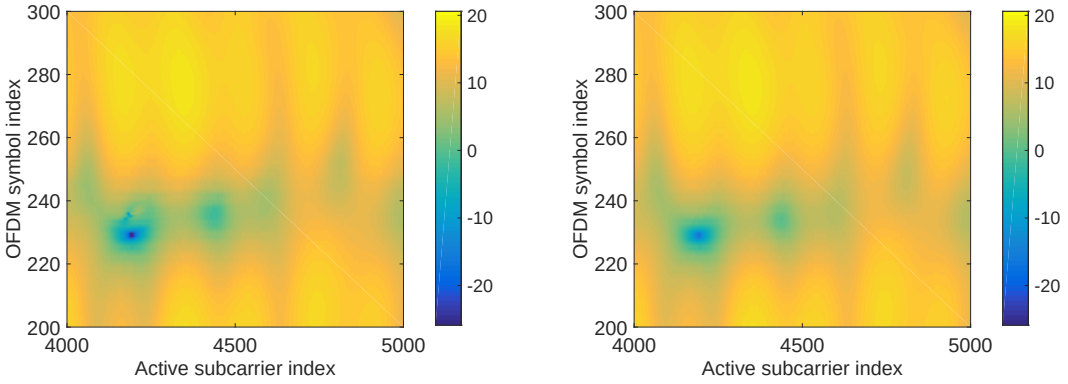

(a) With genie-aided coefficient masking (b) Perfect CSI

Figure 5.10.: Output SNR after combining – continued

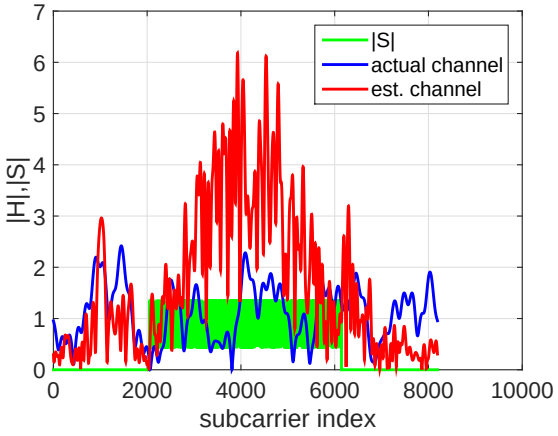

Figure 5.11.: Spectrum of sent signal, actual and estimated channel at SNR = 5 dB and $f_{D,max} = 0.1$ Hz

is not needed, the algorithm is misled by the noise components in those regions and is trying to track them. As shown, the channel estimate (in red) diverges from the actual CFR (in blue).

We notice that, especially at low SNR the estimated channel tends to have high values in the non excited regions, resulting in the divergence behavior of the MCFLMS. In [AES13], we proposed to monitor the energy of the estimate in those null bands and to apply a weighting factor on the estimated channel in the out-of-band regions. Once the ratio of the power in the out-of-band regions to that in the active regions exceeds a certain threshold, k_{onr}, the weighting factor is applied, such that the ratio between the out-of-band energy to the in-band energy remains at k_{onr}. In Figures 5.12 and 5.13, we can see the effectiveness of the proposed weighting approach with $N_a = 4096$ subcarriers, $B = 64$ samples and with coefficient masking. In this simulation, we suppress the estimated channel power in the out-of-band region at a threshold value of $k_{onr} = 1.85$. As we can see, as the number of iterations increases, the simulation curve which does not apply out-of-band noise reduction experiences a worse performance, which can lead at some point to algorithm instability.

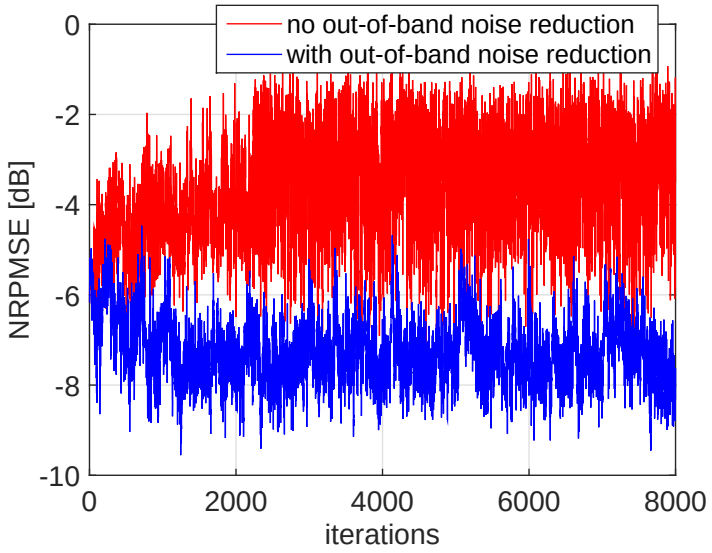

Figure 5.12.: NRPMSE in the case weighting is used vs the case when it is not used at SNR $= 5\,\mathrm{dB}$ and $f_{D,max} = 0.1\,\mathrm{Hz}$ and $\lambda_s = \frac{1}{256}$.

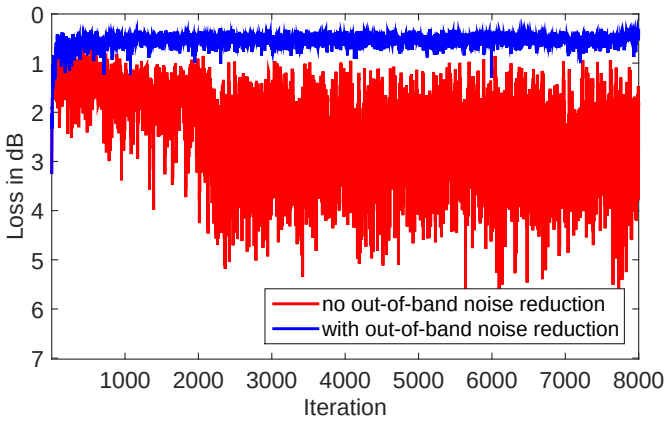

Figure 5.13.: Output SNR loss in the case weighting is used vs the case when it is not used at SNR $= 5\,\mathrm{dB}$ and $f_{D,max} = 0.1\,\mathrm{Hz}$ and $\lambda_s = \frac{1}{256}$.

5.6. Coded BER Results

In Figure 5.14, we compare the coded BER after LDPC decoder in a DVB-T2 system with different receiver settings. The common simulation settings are listed in Table 5.1.

The lower bound is obtained when GACN is used in combining (circled black curve). We can observe the degradation in performance when synchronization information is not available at the BMRC (dashed green curve). When synchronization information is available at the BMRC block, the matched filters in Figure 5.3 use the same (averaged) channel to combine every block within one OFDM symbol. However, when this information is not available, the BMRC block combines every block within the OFDM symbol with a different estimate of the channel corresponding to the current block, u, $\hat{\mathbf{h}}_m^u$. This in turn results in severe ICI since the estimate differs with every iteration (block operation). We can therefore observe around 1 dB performance loss because of the lack of synchronization information between the dashed green and dashed blue curves.

Interestingly, when the masking operation is applied, the gap due to lack of synchronization information almost disappears, as we can observe following the starred blue and starred green curves. This is because when the masking is applied successfully, the small noisy taps which change quite fast are suppressed, and hence a smoother CIR across iterations can be obtained, which can significantly reduce ICI. As we can observe, using the masking technique, we could come to around 0.25 dB from the lower bound even with no synchronization information.

Parameter	Setting
System	DVB-T2
BER	after LDPC decoding in dependency of Doppler frequency shift
Architecture	MRC→ZF
CSI used in ZF equalizer	GACN
Doppler shift	100 Hz
Modulation	16QAM
Coding	LDPC $n_{LDPC} = 16K$ code rate=(1/2)
OFDM	8k FFT , 0.25GI , $N_a = 6817$ subcarriers, $N_{data} = 6208$ subcarriers
Channel	TU6 channel
MCFLMS	$B = 512$ samples, μ^u as in (5.34), $\lambda_s = 0.003$, $k_\phi = \frac{\pi}{4}$, $k_{onr} = 1.85$

Table 5.1.: Simulation Parameters used to produce results in Figure 5.14

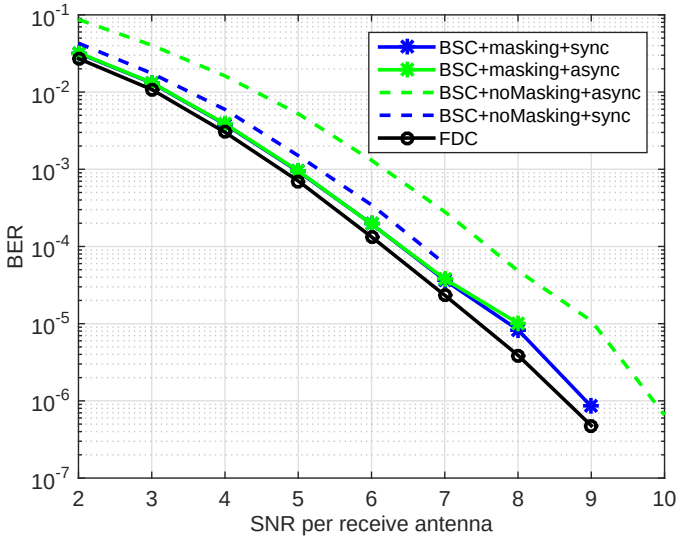

Figure 5.14.: BER performance for a TU6 channel and $f_{D,max} = 100\,\text{Hz}$

6. Conclusions

Nowadays, user mobility and receiver power consumption are two major challenges in wireless communications, in which OFDM became recently a dominant key technology. OFDM is used in the current and upcoming wireless standards, such as DVB, LTE and the upcoming 5G standard. In this thesis, we have studied the ICI problem encountered at the OFDM receiver due to a time-varying channel.

Our aim was to focus on solutions with low complexity which can enable proper reception at high user speeds and which works for a wide range of channel frequency selectivity. To this end, we presented several methods to mitigate the effect of ICI, with a special focus on techniques with reduced complexity.

We observed that, in a doubly selective channel (time and frequency selective), ICI resulting from the time selectivity affects the different subcarriers depending on the frequency selectivity of the channel. In other words, in a doubly selective channel, different subcarriers have to be handled differently. From this observation, we developed an enhanced MMSE equalizer which considers different number of off-diagonal coefficients around each subcarrier, depending on the distortion to which the subcarrier is exposed. The proposed equalizer shows a very good trade-off between performance and complexity, as discussed in Chapter 3.

Antenna receiver diversity has proven to be an effective technique for ICI mitigation. Therefore, in Chapter 4, we have studied classical diversity combining techniques such as MRC, which is the optimum receiver in the absence of interference. We have also studied a combining technique, OC (along with its simplified version SDCC), proposed in [Ser12, STJ08], which takes ICI into consideration. We have also considered the concatenation of different combining techniques with SISO ICI cancelers. We found the best performance is achieved by a concatenation of the ICI-aware diversity combiner OC (or SDCC) followed by an ICIC. Using this architecture, around 95 Hz Doppler performance gain can be achieved, compared to classical MRC which does not consider ICI at all. Throughout these investigations, we used a simple linear interpolation scheme for channel estimation. However, after testing the discussed algorithms using GACN, the same conclusions are still viable, which suggests that using a better CSI method than linear interpolation shall provide the same relative performance.

During these investigations, we found the performance of the ICI-aware diversity combiner OC (or SDCC) to be very sensitive to the way the noise covariance matrix is built. Throughout this thesis, we followed an approach where we relied on CoPs to provide the total noise+ICI value, and in a next step we subtracted a rough estimate of the ICI obtained through the off-diagonal coefficients, as explained in section 4.5.2. This method provided around 30 Hz Doppler gain, as shown in Figure 4.8, compared to the case when no separation is done, i.e, the total noise+ICI value is assigned to the noise covariance

matrix. However, a significant degradation of around 70 Hz Doppler gain is observed relative to the case when the correct AWGN noise level is known and is assigned to the noise covariance matrix. Therefore a huge room for improvement against Doppler variations exists and can be achieved with better estimation of the noise covariance matrix in the ICI-aware diversity combiner OC (or SDCC) .

Taking into account the effect of ICI, in the combining or SISO ICI cancellation step, requires the computation of the off-diagonal coefficients, which in turn requires buffering at least three OFDM symbols. For receiver designs where this requirement is hard to be met, we have proposed an enhanced MRC scheme, in section 4.4 which assumes ICI to be a source of colored noise, which is taken into consideration in building the MRC filtering vector. The idea is again based on the aforementioned observation of the frequency selective distortion to which the different subcarriers are exposed in a doubly selective channel. We have proposed to compute the colored noise using CoPs, which are part of the transmit stream of the DVB-T and DVB-T2 systems.

In the second part of this thesis, we have discussed a special architecture for receiver diversity combining. The proposed architecture does not assume a special transmit signal structure and thus allows for the reception of various broadcasting signals from different standards. To perform diversity combining using MRC, blind channel identification using MCFLMS was employed. We found that in its native form, MCFLMS, is incapable of tracking some channels, depending on the transmit signal structure. Therefore, we applied several modifications, in Chapter 5, to yield an enhanced MCFLMS. We found it advantageous to exploit the sparseness of the channel structure. Applying the proposed scheme on a DVB-T2 system, we found that a blind combining scheme can come very close to the performance of conventional combining using GACN, with around 0.2 dB SNR performance gap. This, however, comes at the expense of very high computational cost, which suggests the possibility of using a sub-optimum version of the MCFLMS algorithm, which provides a trade-off between complexity and performance.

A. Implementation Details

A.1. Input Noise Estimation for MMSE Equalizer

In section 4.5.2, we explained how we estimate the input noise estimation matrix $\check{\mathbf{C}}_{\text{Noise}}$ needed to build the OC filtering vector. In this section, we follow the same steps in (4.43) to (4.45) to estimate the input noise estimation matrix $\mathbf{C}_{\text{Noise}}$, needed to build the MMSE filtering vector.

Figures A.1b and A.2 show the BER performance of a SISO MMSE equalizer using different settings for $\bar{\mathbf{C}}_{\text{Noise},(2\text{D}+1\times 2\text{D}+1)}$ vs different Doppler shifts and SNRs, respectively. Ignoring the ICI power in the total estimated noise power (black curve) delivers the worst performance, as was the case in the SDCC equalizer. As mentioned earlier in section 3.2.1, because the used MMSE equalizer considers only $2D$ diagonals around the main diagonals and ignores the rest of the off-diagonals, the noise covariance matrix should ideally be set as $\bar{\mathbf{C}}_{\text{Noise},(2\text{D}+1\times 2\text{D}+1)} = \left(\sigma^2 + \sigma^2_{resICI}\left(2D\right)\right)\mathbf{I}_{2D}$, where $\sigma^2_{resICI}\left(2D\right)$ is the residual ICI power outside the $2D$ sub- and super-diagonals. We used the formula to estimate the residual ICI power from [MH01]

$$\hat{\sigma}^2_{resICI}\left(2D\right) = 1 - \frac{1}{N_a^2}\left[\left(1+2D\right)N_a + 2\sum_{n=1}^{N_a-1}\left(N_a - n\right)\frac{\sin\left(\left(D+\frac{1}{2}\right)\frac{2\pi}{N_a}n\right)}{\sin\left(\frac{\pi}{N_a}n\right)}J_0\left(2\pi f_{D,max}Tn\right)\right]. \tag{A.1}$$

As shown in Figures A.1b and A.2, using $\bar{\mathbf{C}}_{\text{Noise},(2\text{D}+1\times 2\text{D}+1)} = \left(\sigma^2 + \sigma^2_{resICI}\left(2D\right)\right)\mathbf{I}_{2D+1}$ (green curve) delivers a better performance than $\bar{\mathbf{C}}_{\text{Noise},(2\text{D}+1\times 2\text{D}+1)} = \sigma^2\mathbf{I}_{2D+1}$ (magenta curve). Interestingly, using (4.45) delivers the best performance (black curve), which suggests a better approximation for the residual ICI power than the one in (A.1) should be found.

In general, we find the MMSE equalizer much less sensitive than the SDCC combiner to the mis-estimation of the noise covariance matrix in (3.26).

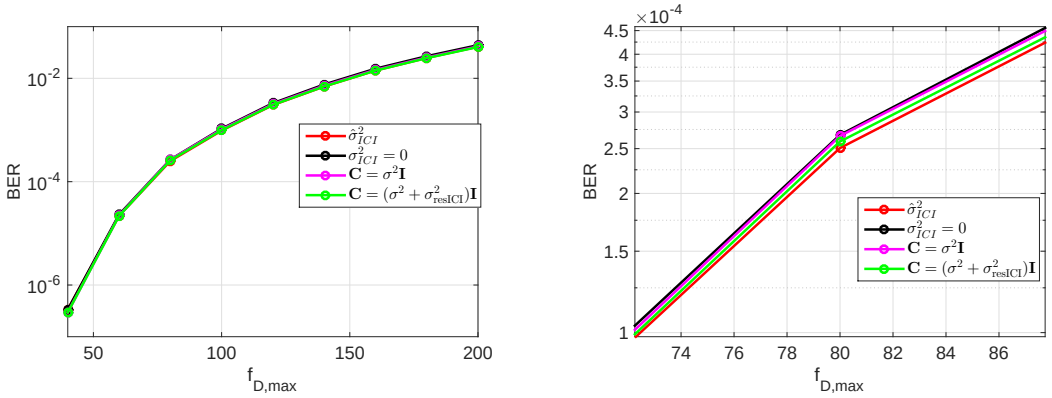

(a) BER performance of MMSE equalizer vs Doppler shift

(b) Zoomed plot

Figure A.1.: AWGN estimation in MMSE equalizer at SNR= 30 dB, 16QAM and TU6 channel. Simulation settings can be found in Table 3.2.

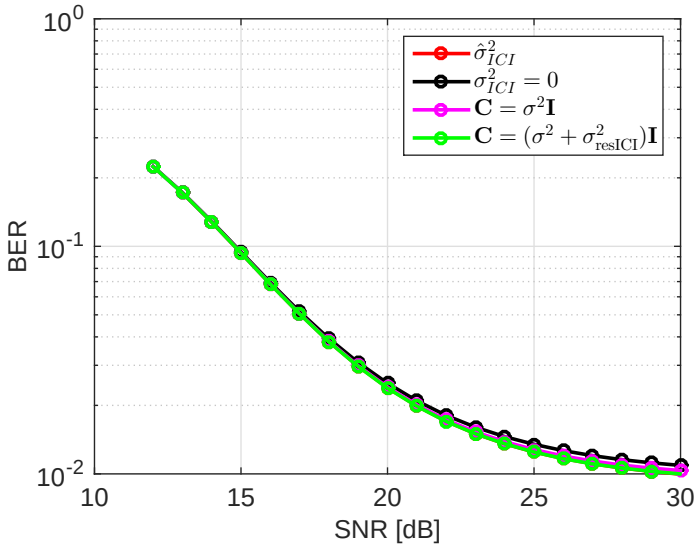

Figure A.2.: AWGN estimation in MMSE equalizer at $f_{D,max} = 150$ Hz, 16QAM and TU6 channel

A.2. PANE after ICI Cancellation

Equations (2.25) and (2.26), reproduced here for convenience,

$$\sigma^2(\iota) = \|R(\iota) - H(\iota, \iota) S(\iota)\|^2 . \tag{A.2}$$

$$\hat{\sigma^2} = \frac{1}{N_{CoP}} \sum_{\iota \in \Omega_{CoP}} \sigma^2(\iota) \tag{A.3}$$

assume that the input to the noise estimation block are the raw output symbols received from the communication channel. Therefore, the noise to be estimated is AWGN and a simple averaging is sufficient to get a good estimate of it.

In the case when the noise estimation is done after processing and normalizing the received signal, the output noise is no longer white. Therefore, before applying (A.3), the output symbols have to be de-normalized or equivalently the estimated noise at pilot positions have to be de-normalized. The steps done to perform noise estimation on the estimated symbols, to be forwarded to the demapper block, then goes as follows:

1.
$$\sigma^2(\iota) = \left\| \hat{S}(\iota) - S(\iota) \right\|^2 , \tag{A.4}$$

2.
$$\hat{\sigma^2}_a = \frac{1}{N_{CoP}} \sum_{\iota \in \Omega_{CoP}} \chi^2 \left(\Omega_{CoP}(\iota) \right) \sigma^2(\iota) , \tag{A.5}$$

3.
$$\hat{\sigma^2}(k) = \frac{\hat{\sigma^2}_a}{\chi^2(k)}, \tag{A.6}$$

where $\chi(k)$ is a de-normalization factor which depends on the kind of processing done. For example, in the case of a ZF equalizer, $\chi(k) = H(k, k)$. When using MMSE equalizer, we estimated $\chi(k) \approx \tilde{\mathbf{W}}^H_{f,(2D+1\times1)}(k)\, \mathbf{C}_{\text{Noise},(2\text{D}+1\times2\text{D}+1)}(k)\, \tilde{\mathbf{W}}_{f,(2D+1\times1)}(k)$, where the frequency noise covariance matrix is built from the estimated total input noise to the MMSE equalizer as $\mathbf{C}_{\text{Noise},(2\text{D}+1\times2\text{D}+1)}(k) = \begin{bmatrix} \hat{\sigma}_t^2(k-D) & & \\ & \ddots & \\ & & \hat{\sigma}_t^2(k+D) \end{bmatrix}$. Using a PIC equalizer, we used the de-normalization factor used in a ZF equalizer, i.e., $\chi(k) \approx H(k, k)$, since no linear filtering step is involved in this equalizer.

B. MMSE→OC

In Figure B.1, we can see the equivalent channel after applying MMSE on the whole received vector of FFT size $N = 256$ according to (3.26). As we can see, the pattern is different from that observed before in the $2D$ FFT plots of channel matrix in Figures 3.1b, 3.2b and 3.3b, where the energy among the off-diagonals does not steadily decrease as the distance from the main diagonal increases.

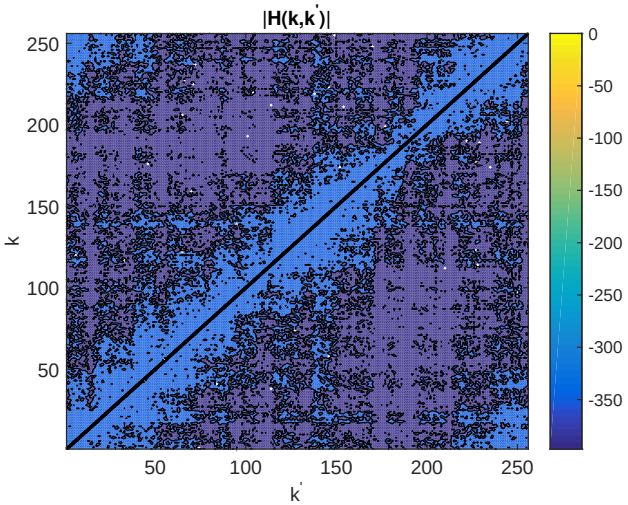

Figure B.1.: Equivalent channel after full MMSE equalization in a TU6 channel at $f_{D,norm} = 0.2$

The same behavior is also encountered when using a windowed MMSE equalizer, with $D = 2$, as shown in Figures B.2a and B.2b on a TU6 channel and a flat channel respectively. We can clearly see, especially in Figure B.2b, that the energy is no longer concentrated in the few off-diagonal coefficients around the main diagonal.

In Figures B.3a and B.3b, the magnitude of the interference off-diagonal coefficients are shown after MMSE equalization at $f_{D,norm} = 0.2$, using $D = 1$ and $D = 2$ in a flat fading channel, respectively. As shown, after filtering with an MMSE equalizer, the position of the most significant interferer on subcarrier k changes from the neighboring subcarriers $k+1$ and $k-1$ (via the off-diagonal coefficients $H(k, k+1)$ and $H(k, k-1)$ respectively) to the interference from subcarriers $k-D-1$ and $k+D+1$ (through the off-diagonal coefficients $H(k, k-D-1)$ and $H(k, k+D+1)$). This can be explained easily if we consider the structure of the MMSE equalization as a filtering operation with a filter whose main tap exists in the middle according to (3.31), i.e., a delay of D samples is caused because of the filtering operation.

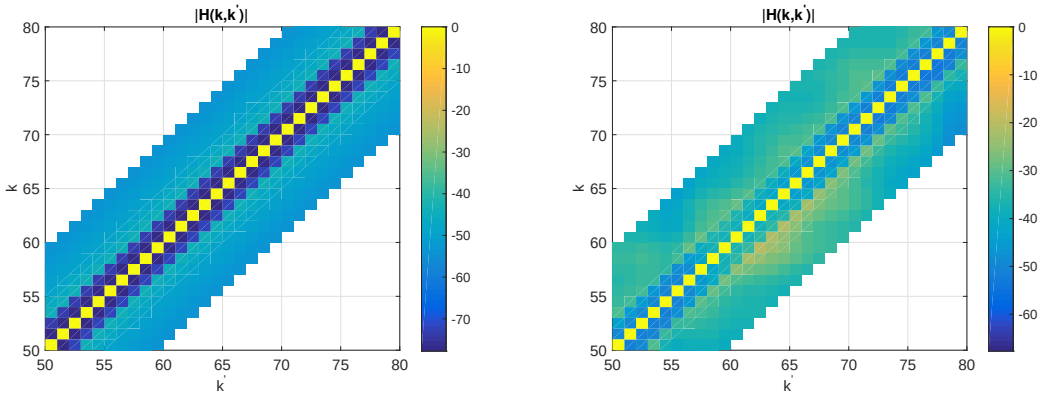

(a) TU6 channel (b) Flat Fading Channel

Figure B.2.: Equivalent channel after MMSE $f_{D,norm} = 0.2$

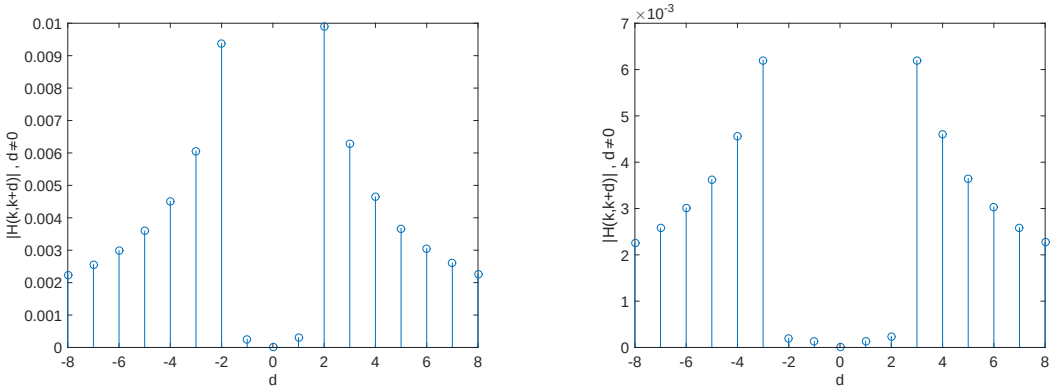

(a) $D = 1$ (b) $D = 2$.

Figure B.3.: Off-diagonal coefficients of the equivalent channel after MMSE $f_{D,norm} = 0.2$

This behavior has a significant impact on the BER behavior in the case when the MMSE block is followed by an SDCC diversity combiner(MMSE→SDCC), since in this case the approximation used in (4.24) is no longer valid in this case. The SDCC combiner uses the output equivalent channel of MMSE to build the interference matrix $\check{\mathbf{C}}_{\mathrm{ICI}}$. Equation (4.24) assumes that the strongest interference comes from the neighboring subcarrier $k \pm 1$ and that the power of the interference decays with $\frac{1}{d^2}$, therefore in such a case, the ICI part of the interference+noise matrix $\mathbf{Z} = \check{\mathbf{C}}_{\mathrm{ICI}} + \check{\mathbf{C}}_{\mathrm{Noise}}$ is significantly underestimated. As shown in Figure B.4, the performance of MMSE→SDCC is close to that of MMSE→MRC because of the underestimation of the interference matrix. MMSE→OC gives a better performance than MMSE→SDCC because it considers all off-diagonal coefficients instead of just the one originating from the neighboring subcarrier.

However, as shown in Figure B.4, MMSE→OC still gives a worse performance than OC standalone, which might be attributed to the fact that after MMSE equalization, the input noise to the OC block is colored (because of the filtering operation). As we see in Figure 4.8, OC is quite sensitive to the way the noise covariance matrix $\check{\mathbf{C}}_{\mathrm{Noise}}(k)$ is built. Therefore, inaccurate computation of the noise variance information leads to a significant degradation in performance.

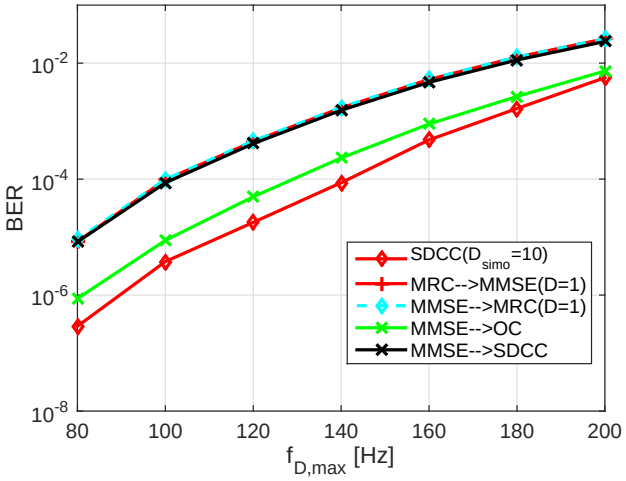

Figure B.4.: Performance loss between MMSE→SDCC and MMSE→OC

Our solution to this problem is to identify the strongest interferer at $\tilde{H}(k,\, k+D+1)$ and to pass it as an input to the SDCC combining block, which computes the ICI covariance matrix as

$$\check{\mathbf{C}}_{\mathrm{ICI}}(k) = \left(\sum_{d=-D,\, d\neq 0}^{D} \left(\frac{1}{d}\right)^2 \right) \tilde{\check{\mathbf{H}}}(k,\, k+D+1)\, \tilde{\check{\mathbf{H}}}^{H}(k,\, k+D+1)\,, \tag{B.1}$$

where $\tilde{\tilde{\mathbf{H}}}(k,\, k+D+1) = \begin{bmatrix} \tilde{H}_1(k,\, k+D+1) \\ \vdots \\ \tilde{H}_M(k,\, k+D+1) \end{bmatrix}$, instead of as in (4.26). As shown in Figure (B.5), following the approach in (B.1), a better performance is reached (blue curve), however, it still lags in performance behind MMSE→OC. Though the strongest interferer is correctly chosen at $\tilde{H}(k,\, k+D+1)$, the implicit assumption of the linear decay rate in the SDCC block according to (4.24) is no longer accurate in (B.1), $\tilde{H}(k,\, k+D+d+1) \overset{?}{\approx} \frac{1}{d}\tilde{H}(k,\, k+D+1)$, which results in the observed degradation.

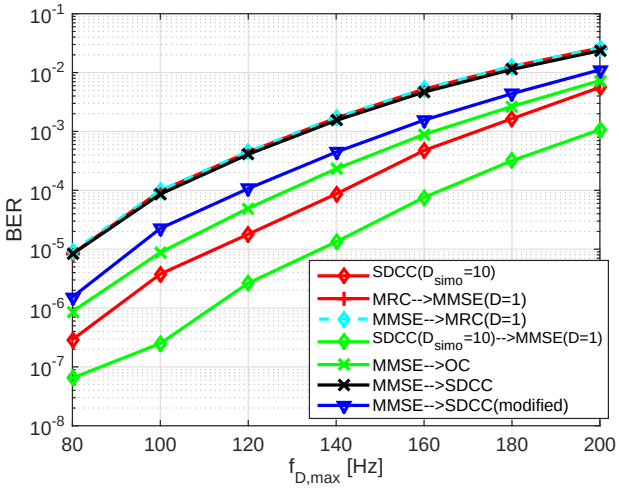

Figure B.5.: Performance of enhanced MMSE→SDCC

Bibliography

[AEBAM08] A. Aissa-El-Bey and K. Abed-Meraim. Blind SIMO channel identification using a sparsity criterion. In *IEEE 9th Workshop on Signal Processing Advances in Wireless Communications, 2008. SPAWC 2008.* , pages 271 –275, Jul. 2008.

[AEBAML11] A. Aissa-El-Bey, K. Abed-Meraim, and C. Laot. Adaptive blind estimation of sparse SIMO channels. In *7th International Workshop on Systems, Signal Processing and their Applications (WOSSPA), 2011* , pages 348 –351, May 2011.

[AES13] Rana Ahmed, Ben Eitel, and Joachim Speidel. Enhanced blind maximum ratio combining in broadcasting systems. In *15. ITG-Fachtagung fuer Elektronische Medien (Fernsehsehminar)*, 2013.

[AES15] Rana Ahmed, Ben Eitel, and Joachim Speidel. Enhanced maximum ratio combining for mobile DVB-T reception in doubly selective channels. In *2015 IEEE 81st Vehicular Technology Conference:VTC2015-Spring*, 2015.

[AK05] G. Auer and E. Karipidis. Pilot aided channel estimation for ofdm: a separated approach for smoothing and interpolation. In *2005 IEEE International Conference on Communications, 2005. ICC 2005.*, volume 4, pages 2173–2178 Vol. 4, May 2005.

[ALS14] Rana Ahmed, Nabil Sven Loghin, and Joachim Speidel. Adaptive sliding window minimum mean square error inter-carrier interference cancellation. In *Vehicular Technology Conference (VTC Spring), 2014 IEEE 79th*, pages 1–5, May 2014.

[ATSa] ATSC. ATSC digital television standard.

[ATSb] ATSC. Call for proposals for ATSC 3.0. physical layer: A terrestrial broadcast standard ATSC technology group 3 (ATSC 3.0).

[ATS09] ATSC. ATSC mobile DTV standard, 2009.

[ATS13] ATSC. Detailed ATSC 3.0 Physical Layer Technical Proposals Being Evaluated., Oct 2013.

[Bul00] Scott R. Bullock. *Transceiver and System Design for Digital Communications.* Noble Publishing Corporation, 2nd edition, 2000.

[CEPB02] S. Coleri, M. Ergen, A. Puri, and A. Bahai. Channel estimation techniques based on pilot arrangement in OFDM systems. *IEEE Transactions on Broadcasting*, 48(3):223–229, Sep 2002.

[Cha66] R. W. Chang. High-speed multichannel data transmission with bandlimited orthogonal signals. *Bell Sys. Tech.*, 45:1775–96, 1966.

[CLB+07] Sammo Cho, Gwangsoon Lee, Byungjun Bae, Kyutae Yang, Chung-Hyun Ahn, Soo-In Lee, and Chiteuk Ahn. System and services of terrestrial digital multimedia broadcasting (T-DMB). *IEEE Transactions on Broadcasting*, 53(1):171–178, March 2007.

[COS89] COST-207. Digital land mobile radio communications(final report). Technical report, Commission of the European Communities, Directorate General Communications, Information Industries and Innovation, 1989. pp. 135-147.

[dCS04] E. de Carvalho and D. T M Slock. Blind and semi-blind FIR multichannel estimation: (global) identifiability conditions. *IEEE Transactions on Signal Processing*, 52(4):1053–1064, April 2004.

[dtm06] Framing structure, channel coding and modulation for digital television terrestrial broadcasting system, 2006.

[DVB09] DVB. *DVB Document A133, Implementation Guidelines for a second generation digital terrestrial transmission system*, Dec 2009.

[DVB12] DVB. Digital Video Broadcasting (DVB); Next Generation broadcasting system to Handheld, physical layer specification (DVB-NGH), Nov. 2012.

[EAS13] B. Eitel, R. Ahmed, and J. Speidel. Enhanced blind maximum ratio combining using channel tap masking for broadcasting applications. In *IEEE Third International Conference on Consumer Electronics Berlin (ICCE-Berlin), 2013. ICCEBerlin 2013.*, pages 79–83, Sept 2013.

[ETS09a] ETSI. ETSI EN 300 744 Digital Video Broadcasting (DVB); Framing structure, channel coding and modulation for digital terrestrial television, Jan. 2009.

[ETS09b] ETSI. ETSI EN 302 755 v1.1.1, Frame Structure channel coding and modulation for a second generation digital terrestrial television broadcasting system (DVB-T2), Sept. 2009.

[ETS11] ETSI. ETSI TR 101 190 Implementation guidelines for DVB terrestrial services; Transmission aspects, Mai. 2011.

[FA08] Borko Furht and Syed A. Ahson. *Handbook of mobile broadcasting: DVB-H, DMB, ISDB-T, and MEDIAFLO.* Auerbach Publications, Boston, MA, USA, 1st edition, 2008.

[FAPBRB+11] L. Ferrer-Arnau, V. Parisi-Baradad, R. Reig-Bolano, P. Marti-Puig, and A. Manjabacas. Efficient representation of contours using splines implemented with FIR filters. In *2011 7th International Conference on Next Generation Web Services Practices (NWeSP)*, pages 125–128, Oct 2011.

[Flo14] Sofia Flores. Verizon and embms: the operator incentive. http://www2.alcatel-lucent.com/techzine/verizon-and-embms-the-operator-incentive/, February 2014.

[GB13] David Gómez-Barquero, editor. *Next generation mobile broadcasting.* CRC Press, 2013.

[GEV12] A.Y. Gafer, S. Elsadig, and J. Varun. Front-end signal to noise ratio estimation for DVBT fixed reception in flat-fading channel. In *2012 4th International Conference on Intelligent and Advanced Systems (ICIAS)*, volume 1, pages 296–300, June 2012.

[GHN06] Nikolay D. Gaubitch, Md. Karmul Hasan, and Patrick A. Naylor. Generalized optimal step-size for blind multichannel LMS system identification. *IEEE signal processing letters*, (10), Oct. 2006.

[God80] D. Godard. Self-recovering equalization and carrier tracking in two-dimensional data communication systems. *IEEE Transactions on communications*, pages 1867–1875, November 1980.

[GVGBC10] D. Gozalvez, D. Vargas, D. Gomez-Barquero, and N. Cardona. Performance evaluation of DVB-T2 time interleaving in mobile environments. In *2010 IEEE 72nd Vehicular Technology Conference Fall (VTC 2010-Fall)*, pages 1–5, Sept 2010.

[GXK95] Lang Tong Ghaunghan Xu, Hiu Liu and Thomas Kaliath. A least squares approach to blind channel identification. *IEEE Transactions on Signal Processing*, 43(12), December 1995.

[Hay00] S. Haykin. *Unsupervised adaptive filtering: volume 2 Blind Deconvolution.* Prentice Hall, 2000.

[Hay01] Simon Haykin. *Adaptive Filter Theory.* Pearson, 2001.

[HB02] Yiteng Arden Huang and Jacob Benesty. Adaptive multi-channel least mean square and Newton algorithms for blind channel estimation. *SIGNAL PROCESSING*, 82:1127–1138, Aug. 2002.

[HB03] Yiteng Arden Huang and Jacob Benesty. A class of frequeny-domain adaptive approaches to blind multichannel identification. *IEEE Transactions on signal processing*, 51(1), Jan. 2003.

[HBC03] Yiteng Arden Huang, Jacob Benesty, and Jingdong Chen. Adaptive blind identification of SIMO systems using channel cross-relation in the frequency domain. *ICASSP2003*, 2003.

[HBC05] Yiteng Huang, J. Benesty, and Jingdong Chen. Optimal step size of the adaptive multichannel lms algorithm for blind simo identification. *Signal Processing Letters, IEEE*, 12(3):173–176, March 2005.

[HH07] Mohammad Ariful Haque and Kamrul Hasan. Variable step size frequency domain multichannel LMS algorithm for blind channel identification with noise. *Journal IET Signal Processing*, 1:182–189, 2007.

[HHDCC00] A A Hutter, J.S. Hammerschmidt, E. De Carvalho, and J.M. Cioffi. Receive diversity for mobile OFDM systems. In *IEEE Wireless Communications and Networking Confernce, 2000. WCNC*, volume 2, pages 707–712 vol.2, 2000.

[HHH+07] F. Hartung, U. Horn, J. Huschke, M. Kampmann, T. Lohmar, and M. Lundevall. Delivery of broadcast services in 3G networks. *IEEE Transactions on Broadcasting*, 53(1):188–199, March 2007.

[HKR97] P. Hoeher, S. Kaiser, and P. Robertson. Two-dimensional pilot-symbol-aided channel estimation by Wiener filtering. In *1997 IEEE International Conference on Acoustics, Speech, and Signal Processing, 1997. ICASSP-97.*, volume 3, pages 1845–1848 vol.3, Apr 1997.

[HLT94] Ghaunghan Xu Hiu Liu and Lang Tong. Determinstic approach to blind identification of multi-channel FIR systems. *ICASSP Proceedings of the Acoustics, Speech, and Signal Processing*, 4, 1994.

[HM11] Franz Hlawatsch and Gerald Matz, editors. *Wireless communications over rapidly time-varying channels.* Academic Press, 2011.

[HO02] B. Holter and G. E. Oien. The optimal weigths of a maximum ratio combiner using an eigenfilter approach. In *5th Nordic Signal Processing Symposium*, 2002.

[Hua96] Yingbo Hua. Fast maximum likelihood for blind identification of multiple FIR channels. *IEEE transactions on signal processing*, 44(3), Mar. 1996.

[ITU12] Frequency and network planning aspects of dvb-t2 bt.2254. Technical report, ITU-R, 2012.

[Jak74] William C. Jakes. *Microwave mobile communications.* Wiley, 1974.

[Kay93] Steven M. Kay. *Fundamentals of statistical signal processing.* Prentice Hall, first edition, 1993.

[Kaz11] Rana Kazamel. Inter-carrier interference mitigation for mobile OFDM. Master's thesis, Institute of Telecommunications, University of Stuttgart, August 2011.

[KHJ03] Seog Geun Kang, Yong Min Ha, and Eon Kyeong Joo. A comparative investigation on channel estimation algorithms for OFDM in mobile communications. *Broadcasting, IEEE Transactions on*, 49(2):142–149, June 2003.

[Kow14] Maryam Kowsari. Pilot-assisted channel and noise variance estimation and ICI cancellation in OFDM systems. Master's thesis, Institute of Telecommunications, University of Stuttgart, July 2014.

[LC06] I-Wei Lai and Tzi-Dar Chiueh. One-dimensional interpolation based channel estimation for mobile DVB-H reception. In *2006 IEEE International Symposium on Circuits and Systems, 2006. ISCAS 2006. Proceedings.*, pages 4 pp.–5210, May 2006.

[Li10] Yunxin Li. Blind snr estimation of OFDM signals. In *2010 International Conference on Microwave and Millimeter Wave Technology (ICMMT)*, pages 1792–1796, May 2010.

[LKAD06] Sili Lu, R. Kalbasi, and N. Al-Dhahir. OFDM interference mitigation algorithms for doubly-selective channels. In *IEEE 64th Vehicular Technology Conference VTC*, pages 1 –5, Sept. 2006.

[LSGBGC12] J. Lopez-Sanchez, D. Gomez-Barquero, D. Gozalvez, and N. Cardona. On the provisioning of mobile digital terrestrial TV services to vehicles with DVB-T. *IEEE Transactions on Broadcasting*, 58(4):642–647, Dec 2012.

[Mas06] Simon Mason. Mobile TV - results from the DVB-H trial in Oxford. Technical report, EBU technical review, 2006.

[MBS98] Dennis R. Morgan, Jacob Benesty, and M. Mohan Sondhi. On the evaluation of estimated impulse responses. *IEEE signal processing Letters*, 5(7), Jul. 1998.

[MC05] Y. Mostofi and D.C. Cox. ICI mitigation for pilot-aided OFDM mobile systems. *IEEE Transactions on Wireless Communications*, 4(2):765 – 774, March 2005.

[MDM95] Eric Moulines, Pierre Duhamel, and Sylvie Mayrague. Subspace methods for the blind identification of multichannel FIR filters. *IEEE Transactions on Signal Processing*, 43(2), Feb. 1995.

[MH01] M. Munster and L. Hanzo. Second-order channel parameter estimation assisted cancellation of channel variation-induced inter-subcarrier interference in OFDM systems. In *EUROCON'2001, International Conference on Trends in Communications.*, volume 1, pages 1–5 vol.1, July 2001.

[MOP07] C-C Jay Kuo Man-On Pun, Michele Morelli. *Multi-carrier techniques for broadband wireless communications: A signal processing perspective.* Imperial College London, 2007.

[MTV07a] A.F. Molisch, M.. Toeltsch, and S.. Vermani. Iterative methods for cancellation of intercarrier interference in OFDM systems. *IEEE Transactions on Vehicular Technology,*, 56(4):2158 –2167, July 2007.

[MTV07b] A.F. Molisch, M.. Toeltsch, and S.. Vermani. Iterative methods for cancellation of intercarrier interference in ofdm systems. *IEEE Transactions on Vehicular Technology*, 56(4):2158–2167, July 2007.

[NGH10] DVB-NGH Channel Models: TM-NGH063. Technical report, DVB, 2010.

[OSB99] A. V. Oppenheim, R. W. Schafer, and J. R. Buck. *Discrete-time signal processing.* Prentice Hall, 1999.

[pMGLHB07] Jean paul M. G. Linnartz, Sri Andari Husen, and Stan Baggen. Mobile reception of DVB-H: How to make it work. In *Proc. IEEE SPS-DARTS2007*, 2007.

[PNG08] Arogyaswami Paulraj, Rohit Nabar, and Dhananjay Gore. *Introduction to Space-Time Wireless Communications.* Cambridge University Press, New York, NY, USA, 1st edition, 2008.

[PS08] John G. Proakis and Masoud Salehi. *Digital communications.* 5 edition, 2008.

[Rap96] Theodore S Rappaport. *Wireless communications: principles and practice.* prentice hall PTR, 1996.

[Rei05] Ulrich Reimers. *DVB: The Family of International Standards for Digital Video Broadcasting.* Springer Science & Business Media, 2005.

[SA05] Marvin K. Simon and Mohamed-Slim Alouini. *Digital communication over fading channels.* Prentice Hall, second edition, 2005.

[Sal11] Rana Ahmed Salem. Blind receive antenna signal combining. Master's thesis, Institut für Systemtheorie und Bildschirmtechnik, University of Stuttgart, 2011.

[Sch] Rhode & Schwarz. Introduction to DVB-T2 "second generation digital terrestrial video broadcasting".

[Ser12] S. Serbetli. Doppler compensation for mobile OFDM systems with multiple receive antennas. In *2012 IEEE 19th Symposium on Communications and Vehicular Technology in the Benelux (SCVT)*, pages 1–6, 2012.

[Skl] Bernard Sklar. *Digital communications: fundamentals and applications*. prentice hall PTR.

[SS13] Xiaoying Shao and Cornelis H. Slump. Opportunistic error correction for OFDM-based DVB systems. *Communications and network*, 5(4):344–352, November 2013.

[STJ08] M. Schellmann, L. Thiele, and V. Jungnickel. Low-complexity Doppler compensation in mobile SIMO-OFDM systems. In *42nd Asilomar Conference on Signals, Systems and Computers, 2008*, pages 1015–1019, 2008.

[Stu96] Gordon L. Stuber. *Principles of Mobile Communication*. Kluwer Academic Publishers, Norwell, MA, USA, 1st edition, 1996.

[TXK91] Lang Tong, G. Xu, and T. Kaliath. A new approach to blind identification and equalization of multipath channels. *Conference Record of the Twenty-Fifth Asilomar Conference on Signals, Systems and Computers.*, Nov. 1991.

[VBT+09] L. Vangelista, N. Benvenuto, S. Tomasin, C. Nokes, J. Stott, A. Filippi, M. Vlot, V. Mignone, and A. Morello. Key technologies for next-generation terrestrial digital television standard dvb-t2. *Communications Magazine, IEEE*, 47(10):146–153, October 2009.

[Ver98] Sergio Verdu. *Multiuser Detection*. Cambridge University Press, New York, NY, USA, 1st edition, 1998.

[WBZS10] Chuan Wu, Dan Bao, Xiaoyang Zeng, and Bo Shen. An efficient iterative frequency domain equalization for ATSC DTV receiver. *IEEE Transactions on Consumer Electronics*, 56(4):–, November 2010.

[Wei09] S.B. Weinstein. The history of orthogonal frequency-division multiplexing [history of communications]. *Communications Magazine, IEEE*, 47(11):26–35, November 2009.

[Wik15] Wikipedia. Telecommunication — wikipedia, the free encyclopedia, 2015. [Online; accessed 11-March-2015].

[Win84] J. Winters. Optimum combining in digital mobile radio with cochannel interference. *IEEE Journal on Selected Areas in Communications*, 2(4):528–539, 1984.

[WJK+14] G. Wunder, P. Jung, M. Kasparick, T. Wild, F. Schaich, Yejian Chen, S. ten Brink, I. Gaspar, N. Michailow, A. Festag, L. Mendes, N. Cassiau, D. Ktenas, M. Dryjanski, S. Pietrzyk, B. Eged, P. Vago, and F. Wiedmann. 5GNOW: non-orthogonal, asynchronous waveforms for future mobile applications. *IEEE Communications Magazine*, 52(2):97–105, February 2014.

[YA05] T. Yucek and H. Arslan. Noise plus interference power estimation in adaptive OFDM systems. In *IEEE 61st Vehicular Technology Conference*, volume 2, pages 1278–1282 Vol. 2, May 2005.

[YA07] T. Yucek and H. Arslan. MMSE noise plus interference power estimation in adaptive OFDM systems. *IEEE Transactions on Vehicular Technology*, 56(6):3857 –3863, Nov. 2007.

[YS12] Mingchao Yu and P. Sadeghi. A study of pilot-assisted ofdm channel estimation methods with improvements for dvb-t2. *IEEE Transactions on Vehicular Technology*, 61(5):2400–2405, Jun 2012.

[ZM09] M. Zivkovic and R. Mathar. Preamble-based snr estimation in frequency selective channels for wireless OFDM systems. In *IEEE 69th Vehicular Technology Conference, 2009. VTC Spring 2009.*, pages 1–5, April 2009.

[ZM10] Milan Zivkovic and Rudolf Mathar. An improved preamble-based snr estimation algorithm for OFDM systems. In *21st International Symposium on Personal, Indoor and Mobile Radio Communications (IEEE PIMRC)*, pages 172–176, Istanbul, Turkey, September 2010.

[ZZB05] Zhigang Zhou, Xiaodong Zhang, and Zhiyong Bu. Interference cancellation based receive scheme to combat ICI for OFDM systems. In *Proceedings of International Conference on Wireless Communications, Networking and Mobile Computing* , volume 1, pages 257 – 260, Sept. 2005.